UNIVERSITÀ DEGLI STUDI DI NAPOLI FEDERICO II

Ph.D. School in EARTH SCIENCES XXV Cycle

Ph.D. Thesis

Depth resolution in potential field inversion: theory and applications

Simone Ialongo

Supervisor

Prof. Giovanni Florio

Ph.D. Coordinator

Prof.ssa Maria Boni

2013

CONTENTS

ABSTRACT

In this thesis we have implemented and studied on detail three different potential field inversion algorithms proposed by Li and Oldenburg (2003), Portniaguine and Zhdanov (2002) and Pilkington (2009). We focused our attention on the dependency of the solution with respect to external constraints and particularly with respect to the depth weighting function. This function is necessary to counteract the natural decay of the data kernels with depth, so providing depth resolution to the inverse solution.

We derived invariance rules for either the minimum-length solution and for the regularized inversion with depth weighting and positivity constraints. For a given source class, the invariance rule assures that the same solution is obtained inverting the magnetic (or gravity) field or any of its k^{th} order vertical derivatives. A further invariance rule regards the inversion of homogeneous fields: the homogeneity degree of the magnetization distribution obtained inverting any of the *k*-order vertical derivatives of the magnetic field is the same as that of the magnetic field, and does not depend on *k*. Similarly, the homogeneity degree of the density distribution obtained inverting any of the *k*-order vertical derivatives of the gravity field is the same as that of the 1^{st} order vertical derivative of the gravity field, and does not depend on *k*. This last invariance rule allowed us using the exponent β of the depth weighting function corresponding to the structural index of the magnetic case, no matter the order of differentiation of the magnetic field. We also illustrated how the combined effect of regularization and depth weighting could influence the estimated source model depth, in the regularized inversion with depth weighting and positivity constraints. We found that too high regularization parameter will deepen the inverted source-density distribution, so that a lower value for the exponent of the depth weighting function should be used, with respect to the

structural index *N* of the magnetic field (or of the 1st vertical derivative of the gravity field). In the attempt to keep the regularization parameter as low as possible, the GCV method yielded better results than the χ^2 criterion.

Furthermore we introduced a new approach to improve the resolution of the model, based on inversion of data with a differentiation order greater than that of the kernel. We analyzed also the case of a field generated by sources with different structural indices. This is a very important case, because it is the most common situation in real data. In this case, there isn't a unique value for β allowing to obtain accurate estimations of depth to all the sources. Thus the depth weighting exponent β must be varied according to the structural index estimated for each source and according to the invariance rules.

Furthermore we studied the dependency of the model obtained by inversion on the depth weighting function when a priori information is included in the inversion. We presented a self-constrained inversion procedure based only on the constraints retrieved by previous potential field anomaly interpretation steps. We showed that adding, as inversion constraints, information retrieved by a previous analysis of the data has a great potential to lead to well-constrained solutions with respect to the source depth and to the horizontal variations of the source-density distribution. Our analysis on both synthetic and real data demonstrated that the more self-constraints are included in the inversion, the less important is the role of the tuning of the depth-weighting function through the actual value of the source structural index.

Another type of a priori information regards the compactness of solution. This constraint can be imposed using the focusing inversion algorithm (Portniaguine and Zhadanov, 2002) or using sparseness constraints (Pilkington, 2009). In this case, imposing this type of constraint tends to decrease the importance of the depth weighting function.

INTRODUCTION

One of the principal difficulties with the inversion of the potential field data is the inherent non-uniqueness. In fact, by Gauss' theorem we know that there are infinitely many equivalent source distributions that can produce a measured field (Blakely, 1996).

In the paragraph 2.3 we will see that when the number of model parameters *M* is greater than the number of observations *N,* a unique solution for the inverse problem does not exist (underdetermined problem). This represents an *algebraic ambiguity* and represents the most common problem in geophysics inversion. Thus we have two causes of ambiguity, both implying that there are infinitely many models that will fit the data to the same degree. To solve an undetermined problem and obtain a unique solution we need to add a priori information.

Prior information takes numerous forms (geological, geophysical or mathematical) and a good inversion algorithm is able to incorporate this information into the inversion.

One of the most important and common prior information is a reference model. In reconnaissance surveys, where little about geology and structures at depth is known, the reference model might be a uniform half space and for some problems just the zero model. In other surveys, the knowledge of the physical property distribution, built up through previous analyses or direct measurements, might be quite detailed (Oldenburg and Li, 2005) and could be incorporated in the reference model.

In the last few years, with the development of ever more efficient computers, many potential fields inversion algorithms have been developed. The origin goes back to 1967, when Bott (1967) used this approach to interpret marine magnetic anomalies. Since then many different algorithms were proposed, each one characterized by a different type of a priori information and then to provide different solutions.

Green (1975) searched for a density model that minimizes its weighted norm to some reference model. Safon at al. (1977) used the method of linear programming to compute moments of the density distribution. Fisher and Howard (1980) solved a linear least-squares problem constrained for upper and lower density bounds. Last and Kubik (1983) introduced a 'compact' inversion minimizing the body volume. Guillen and Menichetti (1984) assumed as a constraint the minimum momentum of inertia. Barbosa and Silva (1994) suggested allowing compactness along given directions using a priori information. Li and Oldenburg (1996, 1998) introduced model weighting as a function of depth using a subspace algorithm. Pilkington (1997, 2002) used preconditioned Conjugate Gradients (CG) method to solve the system of linear equations. Portniaguine and Zhdanov (1999, 2002) introduced regularized CG method and focusing using a reweighted least squares algorithm with different focusing functional. Li and Oldenburg (2003) use wavelet compression of the kernel with logarithmic barrier and conjugate gradient iteration. Pilkington (2009) used data space inversion in Fourier domain.

Other relevant ways to introduce *a priori* information involve "soft constraints", such as positivity constraint for density and magnetization, or "hard constraints", such as empirical laws, constraints for upper and lower density bounds and for a density monotonically increasing with depth (Fisher and Howard, 1980) and external information from well-logs, geological studies and other geophysical investigations. An adaptive learning procedure was presented by Silva and Barbosa (2006) for incorporating prior knowledge. Such procedures lead to a reduction of the general

ambiguity, but is based on relatively strong assumptions about the source characteristics, which may often be too subjective.

So it is obvious that the solution is highly dependent on the prior information and for this reason, as previously said, just one algorithm suitable in every geological context does not cannot exist.

This means that it is very important to choose the correct algorithm according to the geological context of the studied area and according to the available a priori information. For this reasons in this thesis we have studied and implemented three different algorithms for potential field inversion, and in particular those proposed by Li and Oldenburg (2003), Portniaguine and Zhdanov (2002) and Pilkington (2009).

Each of these allows incorporating different prior information and then provide different solutions of the inverse problem.

For example, if we study an area for oil exploration and we want to know the morphology of the basement we need an algorithm producing smooth solutions and allowing to introduce a reference model. An algorithm that works very well in these problems is the Li and Oldenburg (1996, 1998, 2003) algorithm. If we work Instead on environmental problems and we want to study an area characterized by the presence of sinkholes and we want to know depth and shape of these cavities, we need an algorithm producing compact solutions, and we can use the focusing inversion algorithm of Zhdanov (2002) or the one by Pilkington (2009) with sparseness constraints.

CHAPTER I

Potential fields theory

1.1 Introduction

Gravitational and magnetic fields are both potential fields. In the mass free space, potential fields obey Laplace's equation, which states that the sum of the rates of change of the field gradient in three orthogonal directions is zero (Kearey et al., 2002).

In Cartesian coordinates, Laplace's equation is:

$$\frac{\partial^2 \phi}{\partial x^2} + \frac{\partial^2 \phi}{\partial y^2} + \frac{\partial^2 \phi}{\partial z^2} = 0 \qquad (1.1)$$

where ϕ refers to a gravitational or magnetic field and is a function of (x, y, z).

1.2 Gravity field

The gravitational field is defined in terms of the gravitational potential U:

$$U = \frac{\gamma M}{r}. \qquad (1.2)$$

Where γ is the Gravitational Constant, M is the mass of the Earth, and r is the distance from the centre of the Earth.

The first derivative of *U* in any directions gives the component of gravity in that direction. (Kearey et al., 2002)

The gradient of *U* is equal to the gravity *g*:

$$g = \nabla U \qquad (1.3)$$

So the gravity field g is:

$$g = \frac{\partial U}{\partial x} i + \frac{\partial U}{\partial y} j + \frac{\partial U}{\partial z} k \qquad (1.4)$$

Where *i*, *j*, *k* represents unit vectors in the direction of the positive *x*, *y*, *z* axes respectively. The gradient of the gravity field *g* is:

$$\nabla g = \nabla^2 U = \frac{\partial^2 U}{\partial x^2} + \frac{\partial^2 U}{\partial y^2} + \frac{\partial^2 U}{\partial z^2} \qquad (1.5)$$

In non mass-free space:

$$\nabla g = \nabla^2 U = 4\pi\gamma\rho \qquad (1.6)$$

ρ is the density of mass distribution at the point considered. Equation 1.6 is Poisson's equation and describes the potential at all points, even inside the mass distribution. Laplace's equation (1.1) is simply a special case of Poisson's equation valid for mass-free regions of space (Blakely 1996).

Gravimeters measure the vertical component of *g* given by:

$$g_z = \frac{\partial g}{\partial z}$$

Before the results of a gravity survey can be interpreted it is necessary to correct for all variation in the Earth's gravitational field which do not result from the differences of density in the underlying rocks.
The observed gravity is the sum of the following components (Blakely, 1996):

-attraction of the reference ellipsoid (theoretical gravity)
-effect of elevation above sea level (free air effect)
-effect of "normal" mass above sea level (Bouguer slab and terrain effects)
-time-dependent variations (tidal and instrumental drift effects)
-effect of moving platform (Eötvös effect)
-effect of masses that support topographic loads (isostatic effects)
-effect of crust and upper mantle density variations ("geology").

Our goal is to isolate the last quantity, the effect of crustal and upper mantle density variations, from all other terms. This process is referred to as gravity reduction.

The mean value of gravity at the Earth's surface is about 9.8 ms^{-2}. Variations in gravity caused by density variation in the subsurface are of the order of 100 μms^{-2}. In honor of Galileo, the cgs unit of acceleration due to gravity (1 cms^{-2}) is the Gal and its sub-units milliGal (1 mGal=10^{-3} Gals) (Kearey et al. 2002).
The measurement of gravity gradients is often given in the Eötvös unit which equals 10^{-4} mGal/m or 0.1 mGal/km.

1.3 Magnetic field

Magnetic fields can be defined in term of magnetic potentials in a manner similar to gravitational fields. For a single dipole of strength *m* the magnetic potential *V* at a distance *r* from the pole is given by:

$$V = \frac{\mu_0 m}{4\pi\mu_r r} \qquad (1.7)$$

where μ_0 and μ_r are the free space magnetic permeability and the relative magnetic permeability of the medium separating the poles respectively (Kearey et al. 2002).
Magnetic field can also be defined in terms of a force field which is produced by electric currents. This magnetizing field strength *H* is defined as being the field strength at the centre of a loop of wire of radius *r* through which a current *I* is flowing such that *H=I/2r*.
Materials can acquire a component of magnetization in the presence of an external magnetic field. For low-amplitude magnetic fields, say on the order of the Earth's magnetic field, this induced magnetization is proportional in magnitude and is parallel (or antiparallel) in direction to the external field, that is:

$$M_i = \chi H \qquad (1.8)$$

The proportionality constant χ is called the *magnetic susceptibility (*Blakely, 1996*).*
Susceptibility is in essence a measure of how susceptible a material is to becoming magnetized (Reynolds 1997) and is dimensionless.
The susceptibility χ is related to *magnetic permeability* μ by the following equation:

$$\mu = \mu_0(1+\chi) \qquad (1.9)$$

where μ_0 is the free space magnetic permeability.

The magnetic permeability μ correlates the magnetic induction field *B* with magnetization *H*:

$$B = \mu H \qquad (1.10)$$

The relationship between *M* and *H* is not necessarily linear as implied by equation 1.8; χ may vary with field intensity, may be negative, and may be represented more accurately in some materials as a tensor.

There are many kinds of magnetization (Blakely, 1996):

Diamagnetism, for example, is an inherent property of all matter. In diamagnetism, an applied magnetic field disturbs the orbital motion of electrons in such a way as to induce a small magnetization in the opposite sense to the applied field. Consequently, diamagnetic susceptibility is negative.

Paramagnetism is a property of those solids that have atomic magnetic moments. Application of a magnetic field causes the atomic moments to partially align parallel to the applied field thereby producing a net magnetization in the direction of the applied field. Thermal effects tend to oppose this alignment, and paramagnetism vanishes in the absence of applied fields because thermal effects act to randomly orient the atomic moments. All minerals are diamagnetic and some are paramagnetic, but in either case these magnetizations are insignificant contributors to the geomagnetic field.

There is, however, a class of magnetism of great importance to geomagnetic studies. Certain materials not only have atomic moments, but neighboring moments interact strongly with each other. This interaction is a result of a quantum mechanical effect called *exchange energy.* Suffice it to say that the exchange energy causes a

spontaneous magnetization that is many times greater than paramagnetic or diamagnetic effects. Such materials are said to be *ferromagnetic.* There are various kinds of ferromagnetic materials too, depending on the way that the atomic moments align. These include ferromagnetism proper, in which atomic moments are aligned parallel to one another; *antiferromagnetism,* where atomic moments are aligned antiparallel and cancel one another; and *ferrimagnetism,* in which atomic moments are antiparallel but do not cancel.

At the scale of individual mineral grains, spontaneous magnetization of a ferromagnetic material can be very large. At the outcrop scale, however, the magnetic moments of individual ferromagnetic grains may be randomly oriented, and the net magnetization may be negligible. The magnetization of individual grains is affected, however, by the application of a magnetic field, similar to but far greater in magnitude than for paramagnetism. Hence, rocks containing ferromagnetic minerals will acquire a net magnetization, called *induced magnetization* and denoted by M_i, in the direction of an applied field H, where of course the Earth's magnetic field produces the same response in such materials, and the material is magnetic in its natural state. In small fields, with magnitudes comparable to the earth's magnetic field, the relationship between induced magnetization and applied field is essentially linear, and the susceptibility χ is constant.

Induced magnetization falls to zero if the rock is placed in a field-free environment. However, ferromagnetic materials also have the ability to retain a magnetization even in the absence of external magnetic fields.

This permanent magnetization is called *remanent magnetization,* which we denote here by M_r. In crustal materials, remanent magnetization is a function not only of the atomic, crystallographic, and chemical make-up of the rocks, but also of their geologic, tectonic, and thermal history. In geophysical studies, it is customary to

consider the total magnetization *M* of a rock as the vector sum of its induced and remanent magnetizations, that is:

$$M=M_i+M_r=\chi H+ M_r \qquad (1.11)$$

The relative importance of remanent magnetization M_r to induced magnetization M_i is expressed by the *Koenigsberger ratio Q:*

$$Q=\frac{M_r}{M_i} \qquad (1.12)$$

These may be oriented in different direction and may differ significantly in magnitude. The magnetic effects of a rock arise from the resultant *M* of the two magnetization vectors.

Magnetic anomalies caused by rocks are localized effects superimposed on the normal magnetic field of the Earth. Consequently, knowledge of the behavior of the magnetic field is necessary both in the reduction of magnetic data to a suitable datum and in the interpretation of the resulting anomalies. The magnetic field is geometrically more complex than the gravity field of the Earth and exhibits irregular variation in both orientation and magnitude with latitude, longitude and time (Kearey *et al.* 2002).

Total-field magnetometers are usually the instrument of choice for airborne and shipborne magnetic surveys. As the name implies, total-field magnetometers measure the magnitude of the total magnetic field without regard to its vector direction.

The total field **T** is given by:

$\mathbf{T}= \mathbf{F} + \Delta\mathbf{F}$

where and **F** is the geomagnetic field and $\Delta\mathbf{F}$ represents the perturbation of **F** due to some crustal magnetic source.

The *total-field anomaly* is calculated from total-field measurements by subtracting the magnitude of a suitable regional field, usually the IGRF model appropriate for the date of the survey. If *T* represents the total field at any point, and *F* is the regional field at the same point, then the total-field anomaly is given by (Blakely, 1996):

$$\Delta T = |\mathbf{T}| - |\mathbf{F}| \qquad (1.13)$$

If $|\mathbf{F}| \gg |\Delta\mathbf{F}|$ the total field ΔT can be considered as the component of the anomalous field $\Delta\mathbf{F}$ in the direction of **F** and thus it can be considered a harmonic function (e.g., Blakely, 1996). This condition is usually verified in crustal magnetic studies.

The SI unit of magnetic field strength is the tesla (T). The tesla is too large a unit in which to express the small magnetic anomalies caused by rocks and therefore a subunit, the nanotesla (nT), is commonly used (1 nT=10^{-9}T) (Kearey *et al.* 2002).
The strength of *F* varies from about 25000 nT in equatorial regions to about 70000 nT at the poles (Kearey *et al.* 2002).

CHAPTER II

Elementary inversion theory

Much of the content of this Section follows the book by Menke (1989), which the reader is invited to consult for further details.

2.1 Introduction

The starting place in most inverse problems is a description of the data. Since in most inverse problems the data are simply a table of numerical values, a vector provides a convenient means of their representation. If *N* measurements are performed in a particular experiment, for instance, one might consider these numbers as the elements of a vector **d** of length *N.* Similarly, the model parameters can be represented as the elements of a vector **m** is of length *M.*

data: $\mathbf{d} = [d_1, d_2, d_3, d_4, \ldots, d_N]^T$

(2.1)

model parameters: $\mathbf{m} = [m_1, m_2, m_3, m_4, \ldots, m_M]^T$

The basic statement of an inverse problem is that the model parameters and the data are in some way related. This relationship is called the *model.* Usually the model takes the form of one or more formulas that the data and model parameters are expected to follow.

The simplest and best-understood inverse problems are those that can be represented with the explicit linear equation:

$$\mathbf{Am} = \mathbf{d} \qquad (2.2)$$

The matrix **A** (with *N* X *M* dimension) is called kernel, this equation, therefore, forms the foundation of the study of discrete inverse theory. Many important inverse problems that arise in the physical sciences involve precisely this equation. Others, while involving more complicated equations, can often be solved through linear approximations (Menke, 1989).

The simplest kind of solution to an inverse problem is an estimate $\mathbf{m}_{est}$ of the model parameters. An estimate is simply a set of numerical values for the model parameters.

One remedy to the problem of defining the quality of an estimate is to state additionally some bounds that define its certainty. These bounds can be either absolute or probabilistic. Absolute bounds imply that the true value of the model parameter lies between two stated value.
When they exist, bounding values can often provide the supplementary information needed to interpret properly the solution to an inverse problem (Menke, 1989).

2.2 Least squares solution

When the number of the data (*N*) is greater than the number of model parameters (*M*) the problem in eq. 2.2 is called *overdetermined* problem.

The simplest of methods for solving this kind of problem is based on measures of the size, or length, of the estimated model parameters $\mathbf{m}_{est}$ and of the predicted data $\mathbf{d}_{PR} = \mathbf{A}\mathbf{m}_{est}$.

One of the most common measures of length is the least squares method.

For each observation one defines a prediction error, or misfit, $\mathbf{e}_i = \mathbf{d}_i^{obs} - \mathbf{d}_i^{pre}$. The least square solution is then the one with model parameters that leads to the smallest overall error *E,* defined as:

$$E = \mathbf{e}^T\mathbf{e} = \sum_{i=1}^{N} e_i^2 \qquad (2.3)$$

The total error *E* (the sum of the squares of the individual errors) is exactly the squared Euclidean length of the vector **e**.

Note that although the Euclidean length (eq. 2.3) is one way of quantifying the size or length of a vector, it is by no means the only possible measure.

Extending the least squares to general linear inverse problem we obtain the *least square solution* of the problem 2.2 (Menke, 1989):

$$\mathbf{m} = \left[\mathbf{A}^T\mathbf{A}\right]^{-1}\mathbf{A}^T\mathbf{d} \qquad (2.4)$$

2.3 Minimum length solution

When the number of the data (*N*) is less than the number of model parameters (*M*) the problem in eq. 2.2 is called *underdetermined* problem.

For these problems it is possible to find more than one solution for which the prediction error *E* is zero. (In fact, we shall show that underdetermined linear inverse problems have an infinite number of such solutions).

To obtain a solution $\mathbf{m}_{est}$ to the inverse problem, we must have some means of singling out precisely one of the infinite number of solutions with zero prediction error *E.* To do this, we must add to the problem some information not contained in the equation **Am** = **d.** This extra information is called a priori information and can take many forms, but in each case it quantifies expectations about the character of the solution that are not based on the actual data (Menke, 1989).

The first kind of a priori assumption we shall consider is the expectation that the solution to the inverse problem is "simple," where the notion of simplicity is quantified by some measure of the length of the solution. One such measure is simply the Euclidean length of the solution:

$$L = \mathbf{m}^T\mathbf{m} = \sum m_i^2 \qquad (2.5)$$

A solution is therefore defined to be simple if it is small when measured under the L_2 norm.

We pose the following problem: find the $\mathbf{m}_{est}$ that minimizes $L = \mathbf{m}^T\mathbf{m} = \sum m_i^2$ subject to the constraint that **e = d - Am** = 0 and we obtain the *minimum length solution:*

$$\mathbf{m} = \mathbf{A}^T\left[\mathbf{A}\mathbf{A}^T\right]^{-1}\mathbf{d} \qquad (2.6)$$

2.4 Conjugate gradient

In typical geophysical inverse problem, the dimension of matrix **A** can be very big and can be prohibitive perform the matrix – matrix multiplication and the inverse matrix required by eq. 2.4 and 2.6. In this case it is possible to use the conjugate gradient (CG) algorithm (Appendix A).

The CG algorithm is a very efficient method to resolve large systems, because we never form explicitly the matrices $\mathbf{A}^T\mathbf{A}$ (eq. 2.4) or $\mathbf{A}\mathbf{A}^T$ (eq. 2.6) and do not need to calculate their inverses. The CG algorithm requires only the matrix-vector product of type $\mathbf{Ap}$ and $\mathbf{A}^T\mathbf{q}$ where $\mathbf{p}$ and $\mathbf{q}$ are some vectors with dimension of M and N respectively.

If **A** is overdetermined ($N > M$) the CG converges to least square solution (eq. 2.4).

If **A** is underdetermined ($N < M$) the CG converges to minimum length solution (eq. 2.6).

2.5 Add a priori information

There are many instances in which $L = \mathbf{m}^T\mathbf{m}$ is not a very good measure of solution simplicity. One may not want to find a solution that is smallest in the sense of closest to zero but one that is smallest in the sense that it is closest to some other value. The obvious generalization of eq. 2.5 is then (Menke, 1989):

$$\mathbf{L} = (\mathbf{m} - \mathbf{m_0})^T(\mathbf{m} - \mathbf{m_0}) \qquad (2.7)$$

Where $\mathbf{m_0}$ is the a priori value of the model parameters.

Sometimes the whole idea of length as a measure of simplicity is inappropriate and then we can introduce a weighting matrix $\mathbf{W_m}$ that represents our a priori information. So the eq. 2.7 becomes:

$$\mathbf{L} = (\mathbf{m} - \mathbf{m_0})^T \mathbf{W_m} (\mathbf{m} - \mathbf{m_0}) \qquad (2.8)$$

By suitably choosing the a priori model vector $\mathbf{m_0}$ and the weighting matrix $\mathbf{W_m}$ we can quantify a wide variety of measures of simplicity.

Weighted measures of the prediction error can also be useful. Frequently some observations are made with more accuracy than others. In this case one would like the prediction error e_i, of the more accurate observations to have a greater weight in the quantification of the overall error E than the inaccurate observations. To accomplish this weighting, we define a generalized prediction error and the eq. 2.3 becomes:

$$E = \mathbf{e}^T \mathbf{W_d} \mathbf{e} \qquad (2.9)$$

where the matrix $\mathbf{W}_d$ defines the relative contribution of each individual error to the total prediction error (Menke, 1989).

Now we can define the *weighted least squares solution*:

$$\mathbf{m} = \left[\mathbf{A}^T \mathbf{W_d} \mathbf{A}\right]^{-1} \mathbf{A}^T \mathbf{W_d} \mathbf{d} \qquad (2.10)$$

and the *weighted minimum length solution*:

$$\mathbf{m} = \mathbf{m_0} + \mathbf{W}_m^{-1}\mathbf{A}^{\mathrm{T}}\left[\mathbf{A}\mathbf{W}_m^{-1}\mathbf{A}^{\mathrm{T}}\right]^{-1}\left[\mathbf{d} - \mathbf{A}\mathbf{m_0}\right] \qquad (2.11)$$

If the equation **Am** = **d** is slightly underdetermined, it can often be solved by minimizing a combination of prediction error (E) and solution length (L), ($E+\mu^2 L$).
The damping parameter μ is chosen to yield a solution that has a reasonably small prediction error.
The estimate of the solution is called *weighted dumped least squares solution*:

$$\mathbf{m} = \mathbf{m_0} + \left[\mathbf{A}^{\mathrm{T}}\mathbf{W_d}\mathbf{A} + \mu^2\mathbf{W_m}\right]^{-1}\mathbf{A}^{\mathrm{T}}\mathbf{W_d}\left[\mathbf{d} - \mathbf{A}\mathbf{m_0}\right] \qquad (2.12)$$

which is equivalent to

$$\mathbf{m} = \mathbf{m_0} + \mathbf{W_m}^{-1}\mathbf{A}^{\mathrm{T}}\left[\mathbf{A}\mathbf{W_m}^{-1}\mathbf{A}^{\mathrm{T}} + \mu^2\mathbf{W_d}^{-1}\right]^{-1}\left[\mathbf{d} - \mathbf{A}\mathbf{m_0}\right] \qquad (2.13)$$

2.6 Tikhonov regularization

When the problem is affected by numerical instability, it is called 'ill-posed'. From the numerical point of view, the discretization produces highly ill-conditioned systems of linear equations.
This problem needs to be regularized to be solved. The most common and well-known form of regularization is the one known as *Tikhonov regularization (*Tikhonov and Arsenin, 1977). Here, the idea is to define the regularized solution $\mathbf{m}_\mu$ as the minimum of the following weighted combination of the residual norm and the side constraint (Hansen, 2008):

$$\mathbf{m}_\mu = \arg\min\left\{\left\|\mathbf{A}\mathbf{m} - \mathbf{d}\right\|_2^2 + \mu^2\left\|(\mathbf{m})\right\|_2^2\right\} \qquad (2.14)$$

where the *regularization parameter,* μ controls the weight given to minimization of the side constraint relative to minimization of the residual norm. Clearly, a large value of μ, (equivalent to a large amount of regularization) favors a small solution seminorm at the cost of a large residual norm, while a small, (i.e., a small amount of regularization) has the opposite effect. This parameter also controls the sensitivity of the regularized solution $\mathbf{m}_\mu$ to perturbations in ***A*** and **d**, and the perturbation bound is proportional to μ^{-1}. Thus, the regularization parameter μ is an important quantity which controls the properties of the regularized solution, and should therefore be chosen with care.

2.6.1 Choosing the regularization parameter

A good regularization parameter should yield a fair balance between the perturbation error and the regularization error in the regularized solution. A variety of strategies to choose this parameter have been proposed. These methods can roughly be divided into two classes depending on their assumption about the norm of the perturbation $\|\mathbf{e}\|_2$. The two classes can be characterized as follows (Hansen, 2008):

1. Methods based on knowledge, or a good estimate, of $\|\mathbf{e}\|_2$.
2. Methods that do not require $\|\mathbf{e}\|_2$, but instead seek to extract the necessary information from the given right-hand side.

The first methods are based on the *discrepancy principle* which, in all simplicity, amounts to choosing the regularization parameter such that the residual norm for the regularized solution satisfies (Hansen, 2008):

$$\|\mathbf{Am}-\mathbf{d}\|_2 \leq \|\mathbf{e}\|_2 \qquad (2.15)$$

The second method does not requires the knowledge of the error and is called *Generalized cross-validation* (GCV). This method is based on the fact that if an arbitrary element d_i of the right-hand side **d** is left out, then the corresponding regularized solution should predict this observation well. This leads to choosing the regularization parameter which minimizes the GCV function:

$$G \equiv \frac{\left\|\mathbf{Am}_{\mathbf{reg}}-\mathbf{d}\right\|_2^2}{\left(trace\left(\mathbf{I}_m\mathbf{AA}^T\right)\right)^2} \qquad (2.16)$$

where $\mathbf{A}^T$ is a matrix which produces the regularized solution $\mathbf{m}_{\mathbf{reg}}$ when multiplied with **d**, i.e., $\mathbf{m}_{\mathbf{reg}} = \mathbf{A}^T\mathbf{d}$. (Hansen, 2008).

2.7 Preconditioning

Preconditioning is a technique for improving the condition number of a matrix. Let's introduce a symmetric positive-definite matrix **P** , which is a good approximation of **A**, but is easier to invert. Let us premultiply equation **Am**=**d** by $\mathbf{P}^{-1}$ and then solve:

$$\mathbf{P}^{-1}\mathbf{Am}=\mathbf{P}^{-1}\mathbf{d} \qquad (2.17)$$

If the condition number $k(\mathbf{P}^{-1}\mathbf{A})<<k(\mathbf{A})$ then equation (2.17) converges faster then **Am=d**

The simplest choice is a diagonal matrix, which elements are those of **A**, and is called *Diagonal Preconditioner* or *Jacobi Preconditioner*. (e.g.:Cerovský I., 2004**).**

CHAPTER III

Potential field inversion

3.1 Introduction

The variability of the geologic problems to be studied by the inversion of potential field data implies the need to use different algorithms. The choice of the inversion algorithm depends also on to the available a priori information and on the possibility to exploit it in the inversion algorithm. For these reasons in this thesis we have studied and implemented three different algorithms for potential field inversion, in particular those proposed by Li and Oldenburg (2003), Portniaguine and Zhdanov (2002) and Pilkington (2009).

Each of these allows incorporating different prior information and then provides different solutions of the inverse problem.

The implementation of the algorithms by Portniaguine and Zhdanov (2002) and Pilkington (2009), originally presented only for the magnetic case, was extended also to the gravity problem.

3.2 The problem of minimum length solution: depth weighting function

In paragraph 2.3 we introduced the minimum length solution as the solution for the underdetermined problem. This hypothesis on the solution is the first and the most common a priori information that can be used and in fact all three algorithm studied use this type of constraint. This kind of minimization, without other constraints,

provides solutions with model parameter values as close as possible to zero. Then, because the kernel decays with distance, the minimum length solution will be always concentrated near the surface. In Fig. 3.1 we show a simple example of minimum length inversion of a magnetic field (Fig. 3.1a) generated by a synthetic model composed by one source at *x*=2000m, y=2000 m and z=500 m, with a 100 m^3 volume and 1A/m magnetization (Fig. 3.1 b). The 3D source domain was discretized with 40x40x20 cubic cells, each sized 100x100x100 m^3. We assumed a vertical direction for both the inducing field and the magnetization vector. The minimum length solution is shown in Fig. 3.1c and, as predicted above, the density distribution is concentrate near the surface. This kind of density distribution does not depend on the characteristics of the observed data, but is a direct consequence of the supplied a priori information.

To avoid this too strong influence of the minimum length hypothesis, we need to introduce more a priori information. Li and Oldenburg (1996) were the first that studied this problem and introduced a *depth weighting function* able to counteract the natural decay of the kernel in **A**:

$$w_z = \frac{1}{\left(z + z_0\right)^{\beta}} \qquad (3.1)$$

where *z* is the depth of each layer in the 3D model and the value of z_0 depends upon the observation height and cell size (Li and Oldenburg, 2005). Li and Oldenburg propose to use for β a value equal to 3 in the magnetic case (Li and Oldenburg, 1996) and equal to 2 in the gravity case (Li and Oldenburg, 1998), assuming 3 and 2 as the rate decay of the magnetic or gravity field of a single, small, cubic cell.

Oldenburg and Li (2005) later suggested that the exponent value used in a particular inversion could be chosen, by finding the best performance of different exponent

values applied to trial inversions of synthetic data from forward models similar to the expected solution.

The next sections will be devoted to a complete discussion about the use of the depth weighting exponent.

In Fig. 3.1d we show the solution obtained using the depth weighting function (eq. 3.1): the depth of the center is now correctly estimated.

All three algorithms studied in this thesis use the same (or equivalent) depth weighting function proposed by Li and Oldenburg (1996,1998).

One of the major goals of this work is to study this function and analyze how the solution changes varying the depth weighting function parameters. We will also study the dependence of the three algorithms on this function. As we will see, in fact, the importance of depth weighting function is strictly linked with other a priori information and thus its influence on the solution changes not only using different algorithms, but also in the same algorithm if we use different a priori information.

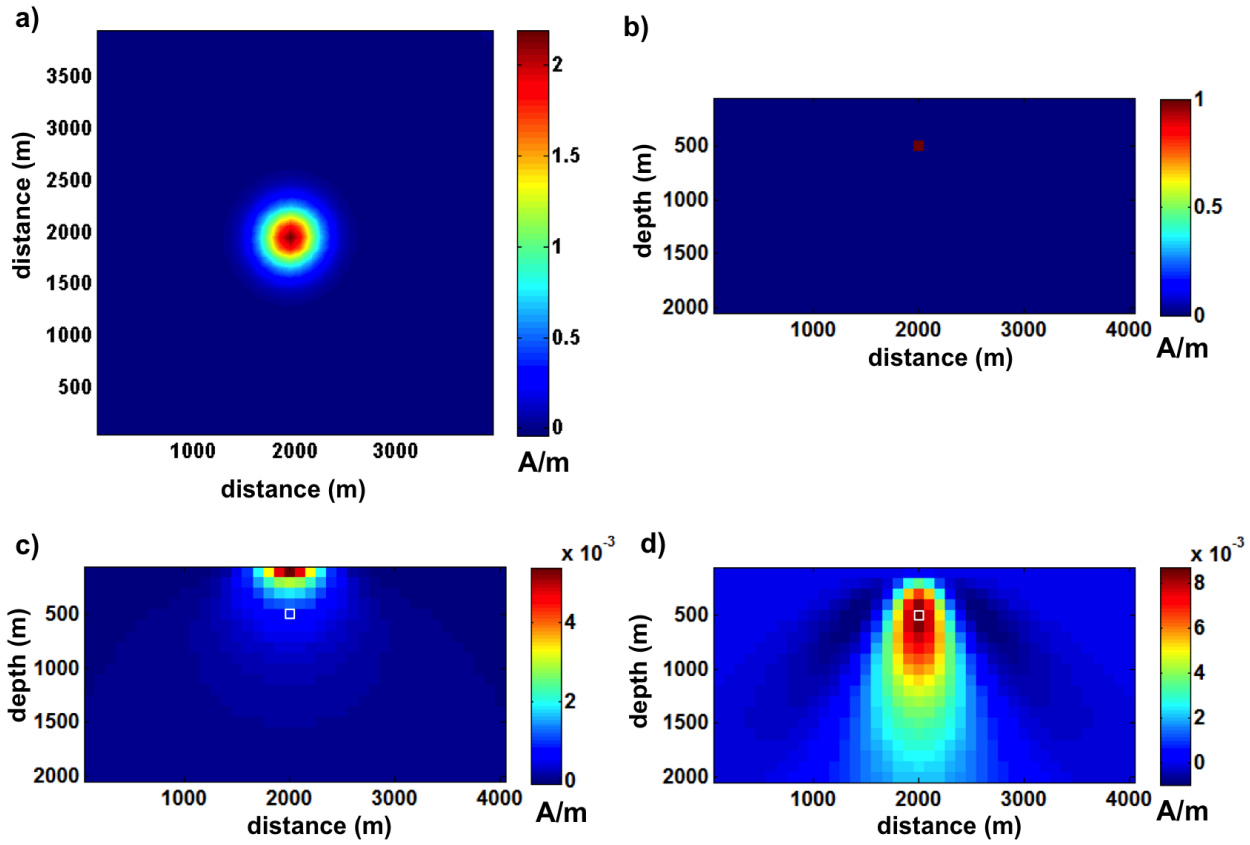

Figure 3.1. *a) magnetic field generated by a single cubic cell shown in b); c) cross section at y=2000m of minimum length solution without depth weighting; d) cross section at y=2000m of minimum length solution obtained using depth weighting function.*

3.3 Forward problem: gravity case

The vertical component of the gravity field produced by a density distribution is given by:

$$F_z(\vec{r}_0) = \gamma \int_V \rho(\vec{r}) \frac{z - z_0}{|\vec{r} - \vec{r}_0|^3} dv \qquad (3.2)$$

wherer_0 is the vector denoting the observation location and *r* is the source location. *V* represents the volume of the anomalous mass, and *γ* is the gravitational constant. Here we have adopted a Cartesian coordinate system having its origin on the Earth's surface and the z-axis pointing vertically downward.

Forward modeling of gravity data is a linear problem and can be carried out by performing the integration in eq. 3.2. We divide the region of interest into a set of 3D prismatic cells by using a 3D orthogonal mesh and assume a constant density within each cell. Given such a discretization, the gravity field at the i^{th} location can be written as:

$$d_i = F_z(\vec{r}_{0i}) = \sum_{j=1}^{M} \rho_j \left\{ \gamma \int_{\Delta V_j} \frac{z - z_0}{\left| \vec{r} - \vec{r}_{0i} \right|^3} dv \right\} = \sum_{j=1}^{M} \rho_j A_{ij} \qquad (3.3)$$

whereρ_j and V_j are the density and volume of the j^{th}cell, d_i is the ith datum.
In matrix notation eq. 3.3 becomes:

$$\mathbf{d=A\rho} \qquad (3.4)$$

or in explicit matrix notation:

$$\begin{pmatrix} d_1 \\ \vdots \\ d_i \\ \vdots \\ d_n \end{pmatrix} = \begin{pmatrix} a_{1,1} & \cdots & a_{1,m} \\ \vdots & a_{ij} & \vdots \\ a_{n,1} & & a_{n,m} \end{pmatrix} \begin{pmatrix} \rho_1 \\ \vdots \\ \rho_j \\ \vdots \\ \rho_m \end{pmatrix} \qquad (3.5)$$

A is the forward modeling operator, called the kernel or sensitivity matrix. This is a rectangular matrix of dimensions *N x M*, defined by the expression in brackets in eq. 3.3 and quantifies the contribution of the j^{th}cell with unit physical parameter (i.e. density = 1.0) to the i^{th} datum, ρ is vector of model parameters of length *M* and **d** is vector of observed data of length *N*. The elements along the columns correspond to different observation locations (x_0, y_0, z_0), while the elements along the rows correspond to different source locations (x, y, z).

To compute the elements of the matrix **A**, any formula for 2D or 3D forward model can be used. In this thesis, 3D polyhedral cells are used. The gravity field is computed using the formula derived by Plouff (1976). The magnetic field is computed using the formula derived by Bhattacharyya (1964).

3.4 Forward problem: magnetic case

We can define the forward problem to magnetic case similarly to the gravity case.

The anomalous field produced by the distribution of magnetization $\vec{J}$ is given by the following integral equation:

$$\vec{B}\left(\vec{r}_0\right) = \frac{\mu_0}{4\pi}\int_V \nabla\nabla\frac{1}{\left|\vec{r}-\vec{r}_0\right|}\cdot\vec{J}dv \qquad (3.6)$$

where $\boldsymbol{r_0}$ is the vector denoting the observation location and ***r*** is the source location, *V* represents the volume of magnetization and μ_0 is the free space magnetic permeability.

3.5 Large scale problems

From the numerical point of view one of the major problems of potential field data inversion is the solution of large-scale problems. The computational complexity increases rapidly with the increasing size of the problem and the solution of large-scale inversion of gravity or magnetic data faces two major obstacles. The first Is the large amount of computer memory required for storing the kernel matrix. The second obstacle is the large amount of CPU time required for the multiplication of the kernel matrix and vectors. These two factors directly limit the size of practically solvable problems. To avoid the first obstacle, one can generate the kernel matrix at the time of processing, but these options will pay the heavy price of increased CPU time for matrix generation (Li and Oldenburg, 2003). To avoid this problem Li and Oldenburg (1996, 1998) introduced a subspace algorithm to perform the inversion. An alternative approach is to carry out the matrix-vector multiplication using the fast Fourier transform (Pilkington, 1997, 2009). This last approach will alleviate the memory limitation and reduce the CPU time dramatically, but the observation must lie over a regular grid on a flat surface above the topography. A different approach was adopted by Portniaguine and Zhdanov (2002) which form a sparse representation of the sensitivity matrix to reduce the computer memory required to store the kernel. Li and Oldenburg (2003) face the problem of large-scale inversion using wavelet transforms to form a sparse representation of the sensitivity matrix.
Cuma et al. (2012), introduce a moving footprint to form, once again, a sparse sensitivity matrix.

3.6 Li and Oldenburg algorithm

3.6.1 Introduction

The Li and Oldenburg (2003) algorithm allows to solve underdetermined problems, with the number of cells significantly larger than the amount of available data. They use an objective function that has the flexibility to construct many different models that generate practically the same data. This goal was reached using appropriate weighting functions whose parameters are empirically selected, based on numerical modeling and qualitative analysis of typical gravity or magnetic anomalies.

3.6.2 Algorithm

The solution is obtained by the following minimization problem (Oldenburg and Li, 2005):

minimize $\varphi = \varphi_d + \mu\varphi_m$

subject to $m_{min} \leq m \leq m_{max}$ (3.7)

where m_{min} and m_{max} are vectors containing the lower and upper bounds on the model values, and m is the vector containing model values.

The prior information that this algorithm allow to introduce might be: (a) knowledge of a background or reference model and (b) a general assumption that the structures should be smooth or that they have sharp edges (Oldenburg and Li, 2005).

The algorithm uses the primal logarithmic barrier method with the conjugate gradient technique (CG) as the central solver. In the logarithmic barrier method, the bound constraints are implemented as a logarithmic barrier term.

The objective function is given by (Gill et al. 1991):

$$\varphi(\lambda) = \varphi_d + \mu\varphi_m - 2\lambda\sum_{j=1}^{M}\left[\ln\left(m_j - m_j^{\min}\right) + \ln\left(m_j^{\max} - m_j\right)\right] \qquad (3.8)$$

where μ is the regularization parameter, λ is the barrier parameter.

φ_d is the weighted data misfit and φ_m is the model objective function. The weighted data misfit is given by:

$$\phi_d = \left\|\mathbf{W_d}\left(\mathbf{d} - \mathbf{d_{obs}}\right)\right\|^2 \qquad (3.9)$$

where d are the predicted data, d_{obs} are the observed data-vector and W_d is the inverse data covariance matrix.

$$\begin{cases} \varphi_m(m) = \alpha_s \int_{vol} w_s w^2(z)\left(\mathbf{m} - \mathbf{m_0}\right)^2 dv + a_x \int_{vol} w_x \left(\dfrac{\partial w(z)\left(\mathbf{m} - \mathbf{m_0}\right)}{\partial x}\right)^2 dv + \\ a_y \int_{vol} w_y \left(\dfrac{\partial w(z)\left(\mathbf{m} - \mathbf{m_0}\right)}{\partial y}\right)^2 dv + a_z \int_{vol} w_z \left(\dfrac{\partial\, w(z)\left(\mathbf{m} - \mathbf{m_0}\right)}{\partial z}\right)^2 dv \end{cases} \qquad (3.10)$$

where m is the unknown model, m_0 is a reference model and $w(z)$ is the depth-weighting function (equation 3.1):

$$w(z) = \frac{1}{(z + z_0)^{\beta/2}}$$

Li and Oldenburg propose to use for β a value equal to 3 in the magnetic case (Li and Oldenburg, 1996) and equal to 2 in the gravity case (Li and Oldenburg, 1998), assuming these values as corresponding with the rate decay with distance of a single small cubic cell in magnetic and gravity field respectively.

As explained in paragraph 3.2 the purpose of this function is to counteract the geometrical decay of the kernel with the distance from the observation location so that the recovered susceptibility is not concentrated near the observation locations.

The terms w_s, w_x, w_y, w_z are spatially dependent weighting functions to input additional prior information about density or susceptibility model. In particular w_s controls the relative closeness of the final model to the reference model at any location, for example we are often more certain about its value in some locations than in others. This is especially true when a reference model has been derived from borehole measurements. Our confidence in the reference model is likely high around the boreholes but decreases away from there. The weights w_x, w_y, w_z, with or without a reference model, control the degree of smoothness of the solution along the three directions (Oldenburg and Li, 2005); finally α_s, α_x, α_y and α_z are coefficients controlling the importance of each term.

The logarithmic barrier term forms a barrier along the boundary of the feasible domain and prevents the minimization from crossing over to the infeasible region.

The method solves a sequence of nonlinear minimizations with decreasing λ and, as λ approaches zero, the sequence of solutions approaches the solution of eq (3.7).

In Fig. 3.2 we show an example of logarithmic barrier function for different values of λ when boundary constraints of 0 and 1 are imposed. Decreasing λ reduces the barrier function value and this allows the model parameters to approach the boundary values.

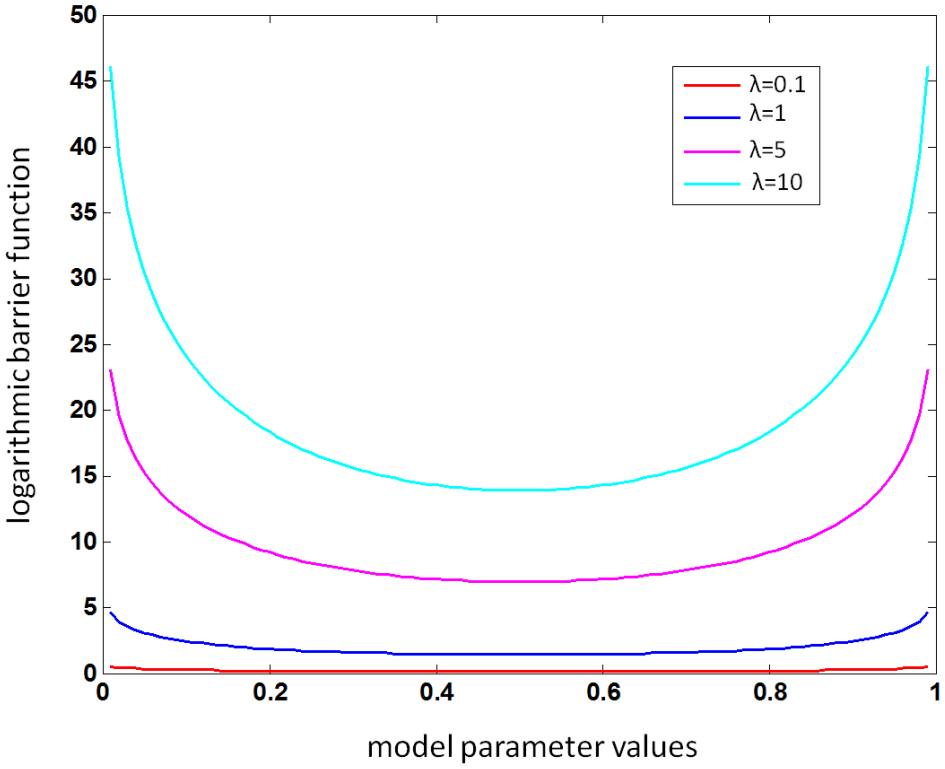

Figure 3.2. *Logarithmic barrier function for different values of λ*

To perform a numerical solution, the model objective function (ϕ_m) in eq. (3.10) is discretized using a finite difference approximation on the mesh defining the model parameters. This yields:

$$\phi_m(m) = (\mathbf{m}-\mathbf{m_0})^{\mathrm{T}}\left(\mathbf{W_s^{\mathrm{T}}W_s} + \mathbf{W_x^{\mathrm{T}}W_x} + \mathbf{W_y^{\mathrm{T}}W_y} + \mathbf{W_z^{\mathrm{T}}W_z}\right)(\mathbf{m}-\mathbf{m_0}) =$$
$$= (\mathbf{m}-\mathbf{m_0})^{\mathrm{T}}\left(\mathbf{W_m^{\mathrm{T}}W_m}\right)(\mathbf{m}-\mathbf{m_0}) = \qquad (3.11)$$
$$= \left\|\mathbf{W_m}(\mathbf{m}-\mathbf{m_0})\right\|^2$$

where:

$\mathbf{W_i} = \alpha_i \mathbf{S_i D_i Z}$ i= s,x,y,z

$\mathbf{S_i}, \mathbf{D_i}, \mathbf{Z_i}$ are *M* X *M* (*M* is the number of model parameter) matrices and precisely:

$\mathbf{S_i}$ are diagonal matrices whose elements w_i (i= s,x,y,z) are defined by the weighting function described before;

$\mathbf{D_s}$ has elements $\sqrt{\Delta x \Delta y \Delta z}$ on its diagonal, where Δx, Δy and Δz are the cell width.

$\mathbf{D_x}$, $\mathbf{D_y}$ and $\mathbf{D_z}$ are matrices representing the finite difference operator along the three spatial directions and precisely:

$\mathbf{D_x}$ has two elements $\pm\sqrt{\Delta y \Delta z/\delta x}$ in each row, where δx is the distance between the centers of cells adjacent in the *x* direction. Similarly $\mathbf{D_y}$ and $\mathbf{D_z}$, have elements $\pm\sqrt{\Delta x \Delta z/\delta y}$ and $\pm\sqrt{\Delta x \Delta y/\delta z}$ respectively, where δy and δz are the distances between centers of adjacent cells in the *y* and *z* direction. **Z** is a diagonal matrix that represent the depth weighting function described in equation 3.1

Because it is not possible to calculate the matrix $\mathbf{W_m}$ we calculate directly $\mathbf{W_m^{\mathrm{T}}W_m}$ with the following expression (Oldenburg and Li, 1994):

$$\mathbf{W_m^{\mathrm{T}}W_m} = \alpha_s(\mathbf{S_s D_s Z})^{\mathrm{T}}(\mathbf{S_s D_s Z}) + \alpha_x(\mathbf{S_x D_x Z})^{\mathrm{T}}(\mathbf{S_x D_x Z}) +$$
$$+ \alpha_y(\mathbf{S_y D_y Z})^{\mathrm{T}}(\mathbf{S_y D_y Z}) + \alpha_z(\mathbf{S_z D_z Z})^{\mathrm{T}}(\mathbf{S_z D_z Z}) \qquad (3.12)$$

The minimization process starts with a large value of λ and a initial model **m** whose elements are all positive. It then finds the solution iteratively with the barrier parameter λ being decreased at each iteration. However, the minimization of the

nonlinear functional in eq. (3.8) at each barrier iteration, is an expensive process. Instead of carrying out the full minimization at each iteration, it is common to take a Newton step for each value of λ and adjust the step length so that the updated model remains positive (Gill et al. 1991). The step length is also used to determine the decreased value of the barrier parameter λ for the next iteration (Li and Oldenburg, 2003).

One step of the Newton method is given by;

$$\mathbf{m_k} = \mathbf{m_{k-1}} + \alpha \Delta \mathbf{m} \qquad (3.13)$$

where $\mathbf{m_k}$ is the updated model at the k^{th} iteration, $\mathbf{m_{k-1}}$ is the model at the previous iteration, α is the step length and

$$\Delta m = \frac{\nabla \varphi(\lambda)}{\nabla^2 \varphi(\lambda)} \qquad (3.14)$$

where $\nabla \varphi(\lambda)$ and $\nabla^2 \varphi(\lambda)$ are the first and second derivatives of the objective function (eq 3.8).

Assuming that the data and corresponding rows of the kernel have been normalized by standard deviations of data errors, at the k^{th} iteration the first and second order derivatives of the eq. 3.8 are given by:

$$\nabla \varphi(\lambda) = -\mathbf{A}^T \delta d - \mu \mathbf{W_m^T W_m} \delta m + \lambda^{(k)} \left(\mathbf{X_a^{-1}} \right) \qquad (3.15)$$

$$\nabla^2 \varphi(\lambda) = \mathbf{A^T A} + \mu \mathbf{W_m^T W_m} + \lambda^{(k)} \mathbf{X}_b^{-2} \qquad (3.16)$$

So at each iteration the algorithm uses the conjugate gradient iterative method to solve the following problem respect to Δm_k :

$$\left(\mathbf{A}^{\mathbf{T}}\mathbf{A}+\mu\mathbf{W}_{\mathbf{m}}^{\mathbf{T}}\mathbf{W}_{\mathbf{m}}+\lambda^{(k)}\mathbf{X}_b\right)\Delta\mathbf{m}=-\mathbf{A}^{\mathbf{T}}\delta\mathbf{d}-\mu\mathbf{W}_{\mathbf{m}}^{\mathbf{T}}\mathbf{W}_{\mathbf{m}}\delta\mathbf{m}+\lambda^{(kn)}diag\left(\mathbf{X}_a\right) \tag{3.17}$$

where:

$$\mathbf{X}_{\mathrm{a}}=\mathbf{I}\left[\mathrm{m}_1-\mathrm{m}_{\min},\ldots,\mathrm{m}_{\mathrm{M}}-\mathrm{m}_{\min}\right]^{-1}+\mathbf{I}\left[\mathrm{m}_{\max}-\mathrm{m}_1,\ldots,\mathrm{m}_{\max}-\mathrm{m}_{\mathrm{M}}\right]^{-1}$$

$$\mathbf{X}_{\mathrm{b}}=\mathbf{I}\left[\mathrm{m}_1-\mathrm{m}_{\min},\ldots,\mathrm{m}_{\mathrm{M}}-\mathrm{m}_{\min}\right]^{-2}+\mathbf{I}\left[\mathrm{m}_{\max}-\mathrm{m}_1,\ldots,\mathrm{m}_{\max}-\mathrm{m}_{\mathrm{M}}\right]^{-2}$$

$$\boldsymbol{\delta}\mathbf{d}=\mathbf{A}\mathbf{m}^{(\mathbf{n}-\mathbf{1})}-\mathbf{d}_{\mathbf{obs}}$$

$$\boldsymbol{\delta}\mathbf{m}=\mathbf{m}^{(\mathbf{n}-\mathbf{1})}-\mathbf{m}_{\mathbf{0}}$$

So we can update the solution according to eq. 3.13

$$\mathbf{m}_{\mathbf{k}}=\mathbf{m}_{\mathbf{k}-\mathbf{1}}+\alpha\boldsymbol{\Delta}\mathbf{m}$$

where α is the maximum permissible step length and is given by:

$$\alpha=\alpha_0\ \min\left[1,\min\left[\frac{m_j^{(k-1)}-m_{\min}}{\left|\Delta m_j\right|}\right]_{\Delta m_j<0},\min\left[\frac{m_{\max}-m_j^{(k-1)}}{\left|\Delta m_j\right|}\right]_{\Delta m_j>0}\right] \tag{3.18}$$

The parameter α_0 is equal to 0.925.

At each iteration, the barrier parameter λ is then updated by:

$$\lambda^k = \left[1 - \min\left(\alpha, \alpha_0\right)\right]\lambda^{(k-1)} \qquad (3.19)$$

The starting value of λ is given by:

$$\lambda^{(0)} = \frac{\phi_d^0 + \mu\phi_m^0}{2\sum_{j=1}^{M}\ln\left(m_j^{(0)}\right)} \qquad (3.20)$$

where $\mathbf{m}^{(0)}$ is the initial model.

The barrier iteration continues until the value of λ is sufficiently small such that barrier term has a negligible contribution to the total objective function (eq. 3.8) and the iteration stops when the objective function is changing less than 1 per cent.

3.6.3 Regularization parameter

The choice of the regularization parameter (μ in eq. 3.8), depends upon the magnitude of the error associated with the data. In fact, the inversion of noisy data requires a heavy regularization, thus a great value of μ is required.

The value of the regularization parameter can be selected a priori by the user or can be automatically estimated.

In the paragraph 2.6.1 we have seen that there are at least two ways to estimate μ. If the standard deviation associated with each datum is known, then the data misfit defined by eq.(3.9) has a known expected value ϕ^*, which is equal to the number of data when the errors are assumed to be independent Gaussian noise with zero mean. Thus the value of μ should be such that the expected misfit ϕ^* is achieved (Li and Oldenburg, 2003):

$$\phi_d^* = \left\| \mathbf{W}_d \left(\mathbf{d} - \mathbf{d}_{obs} \right) \right\|^2 \qquad (3.21)$$

In practical applications the estimate of data error is often not available, and the value of the regularization parameter must be determined using other criteria. A commonly used method in linear inverse problems is the generalized cross-validation (GCV) technique (eq. 2.16, par. 2.6.1).

Li and Oldenburg (2003) show that a good estimate of μ can be obtained applying GCV without positivity.

In the absence of positivity, the solution to the inverse problem is obtained by solving the following equation:

$$\left(\mathbf{A}^{\mathrm{T}} \mathbf{A} + \mu \mathbf{W}_{\mathbf{m}}^{\mathrm{T}} \mathbf{W}_{\mathbf{m}} \right) \Delta \mathbf{m} = -\mathbf{A}^{\mathrm{T}} \delta \mathbf{d} \qquad (3.22)$$

where:

$$\delta \mathbf{d} = \mathbf{A} \mathbf{m}_{\mathbf{0}} - \mathbf{d}_{\mathbf{obs}}$$

So the GCV equation shown in paragraph 2.6.1 becomes (Golub et al. 1979):

$$V(\mu) = \frac{\left\| \left[\mathbf{I} - \mathbf{A} \left(\mathbf{A}^{\mathrm{T}} \mathbf{A} + \mu \mathbf{W}_{\mathbf{m}}^{\mathrm{T}} \mathbf{W}_{\mathbf{m}} \right)^{-1} \mathbf{A}^{\mathrm{T}} \right] \mathbf{d} \right\|^2}{\left\{ N - trace \left[\mathbf{A} \left(\mathbf{A}^{\mathrm{T}} \mathbf{A} + \mu \mathbf{W}_{\mathbf{m}}^{\mathrm{T}} \mathbf{W}_{\mathbf{m}} \right)^{-1} \mathbf{A}^{\mathrm{T}} \right] \right\}^2} \qquad (3.23)$$

where *N* is the number of data.

The numerator is the data misfit obtained solving the eq. 3.22 using CG solver.

Because it is computationally onerous evaluate the trace of the term in brackets, this is carried out by using the stochastic trace estimator of Hutchinson (1990), which states that an unbiased estimate of the trace of a matrix **A** is given by:

$$\text{trace } (\mathbf{A}) = \mathbf{u}^{\mathbf{T}} \mathbf{A} \mathbf{u} \qquad (3.24)$$

where **u** is a random vector of -1 e 1 each having a probability of 0.5.

The GCV function is then approximated by (Li and Oldenburg, 2003):

$$V(\mu)=\frac{\left\|\left[\mathbf{I}-\mathbf{A}\left(\mathbf{A}^{\mathrm{T}}\mathbf{A}+\mu\mathbf{W}_{\mathbf{m}}^{\mathrm{T}}\mathbf{W}_{\mathbf{m}}\right)^{-1}\mathbf{A}^{\mathrm{T}}\right]\mathbf{d}\right\|^{2}}{\left\{N-\mathbf{u}^{\mathrm{T}}\mathbf{A}\left(\mathbf{A}^{\mathrm{T}}\mathbf{A}+\mu\mathbf{W}_{\mathbf{m}}^{\mathrm{T}}\mathbf{W}_{\mathbf{m}}\right)^{-1}\mathbf{A}^{\mathrm{T}}\mathbf{u}\right\}^{2}} \qquad (3.25)$$

The evaluation of *V(μ)* for each value of μ is equivalent to inverting eq. 3.22 two times with different right-hand side. The first inversion is applied to the data vector **d** the second to the random vector **u.** Therefore we choose the μ that minimizes *V(μ)*.

To find the correct value of μ using equation 3.25 we have developed a particular two-step strategy. We first start the search with a set of few μ values, spaced logarithmically, with a very big difference between the maximum and minimum value. In this mode we assure that the function V(μ) in eq. 3.25 will present a point of minimum. Then, to obtain a more accurate estimate of μ, the search is repeated by using more closely spaced values of μ around the μ that minimized the V(μ) at the first step.

3.6.4 Pre conditioner

As barrier iterations progress, many model elements approach the zero bound. Thus the barrier component, λX^{-2}, in eq. (3.17) can cause the matrix **A** to be poorly conditioned and this makes the CG solver converge very slowly. This difficulty is treated by applying a Jacobian pre-conditioner to the CG solver (see par 2.7). The diagonal pre-conditioner P consists of the square root of the diagonal elements of the matrix **G** (Li and Oldenburg, 2003):

$$\mathbf{P} = diag\left\{\sqrt{G_{ij}}\right\} \qquad (3.21)$$

where **G** is the matrix used in the CG algorithm:

$$\mathbf{G} = \mathbf{A}^{\mathrm{T}}\mathbf{A} + \mu\mathbf{W}_{\mathbf{m}}^{\mathrm{T}}\mathbf{W}_{\mathbf{m}} + \lambda^{(k)}\mathbf{X}_b$$

The pre-conditioner is updated at each barrier iteration.

3.6.5 Example

In this section we show some examples of magnetic inversions using the algorithm described above. We computed the magnetic field (Fig. 3.3a) generated by two different sources at two different depths (Fig. 3.3 b).). The shallow source is sized 100 x 100 x 100 m^3 and depth to center z=450 m, with a 100 m^3 volume and 1 A/m magnetization; the deepest source is sized 500 x 500 x 500 m^3 and extend from z=900 m to z= 1400 m with a 0.25 A/m magnetization. The 3D source domain was discretized as 30x30x30 cubic cells, each sized 100x100x100 m^3. We assumed a vertical direction for both the inducing field and the magnetization vector.

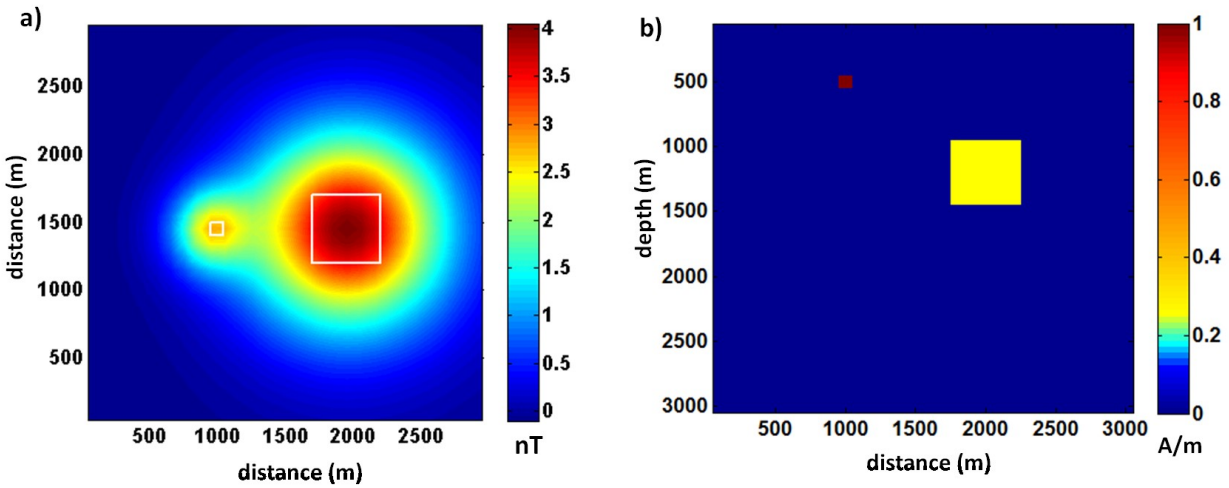

Figure 3.3. *a) Magnetic field of the synthetic model shown in b; b) Cross section at y= 1500 m of the synthetic model with 2 sources: the shallow source is a 100 m^3 block with a 1 A/m magnetization; the deepest source is a cubic prism of 500 m^3 with a 0.25 A/m. magnetization. We assumed a vertical direction for both the inducing field and the magnetization vector.*

We set the α parameters as: α_s=0.0001, α_x=1, α_y=1, α_z=1, and we use for β a value of 3. In Fig. 3.4a we show the solution obtained without positivity constraint, In Fig. 3.4b we show the solution obtained by imposing positivity.

How it is possible to see, without the a priori information about the model positivity, we obtain a very smoothed solution, with a strong underestimation of magnetization values. The resolution of the model is clearly improved using the positivity constraint, although the model is still much smoother than the true sources and consequently the found magnetizations are still severely underestimated.

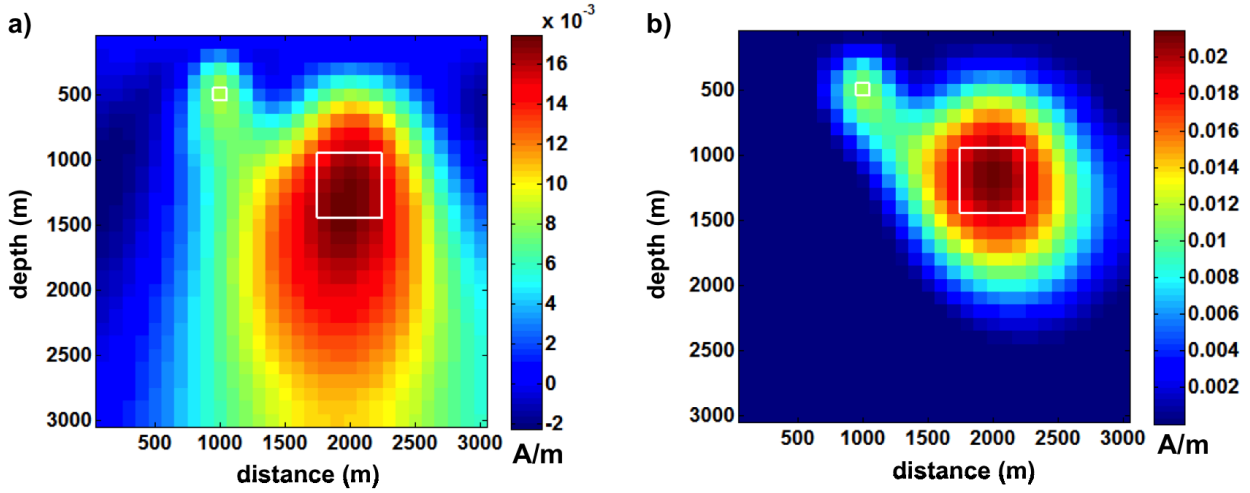

Figure 3.4. *Cross section at y=1500m of magnetization model obtained inverting the anomaly in Fig. 3.3a without positivity constraint (a) and with positivity constraint (b).*

3.7 Focusing inversion (Portniaguine and Zhdanov, 2002)

3.7.1 Introduction

The inversion algorithm developed by Portniaguine and Zhdanov (1999, 2002), presents different features with respect to the Li and Oldenburg algorithm, especially regards the a priori information that it is possible to introduce.

Also this method follows the traditional Tikhonov regularization theory. The authors use the minimum support stabilizing functional, similar to the one introduced by Last and Kubik (1983), for compact 2-D inversion of gravity data. This functional helps generating a sharp, focused inverse models similar to the 3-D gravity inversion considered in Portniaguine and Zhdanov (1999).

3.7.2 Focusing algorithm

Consider the general solution obtained by Tikhonov regularization (eq. 2.14):

$$\mathbf{m} = \arg\min\left\{\left\|\mathbf{Am}-\mathbf{d}\right\|_2^2 + \mu^2\left\|(\mathbf{m})\right\|_{\mathbf{2}}^{\mathbf{2}}\right\} \qquad (3.22)$$

Last and Kubik (1983) were the first proposing to minimize the area (volume in three dimensions) of the model. If *d* and *h* are the cell dimensions, a definition of area for 2-D model is (Last and Kubik, 1983):

$$area = dh\lim_{\varepsilon\to 0}\sum_{k=1}^{M}\frac{m_k^2}{m_k^2+\varepsilon^2} \qquad (3.23)$$

where ε is a small positive number needed to avoid the singularity.

Portniaguine and Zhdanov (1999), introduced a minimum support stabilizing functional $f_{ms}(\mathbf{m})$ to generate a sharp, focused inverse gravity problem solution, similar to the one developed by Last and Kubik (1983):

$$f_{ms} = \sum_{k=1}^{M} \frac{m_k^2}{m_k^2 + \varepsilon^2} \qquad (3.24)$$

Substituting the minimum norm support in eq. (3.22) with f_{ms} we obtain:

$$\mathbf{m} = \arg\min\left\{ \left\| \mathbf{Am} - \mathbf{d} \right\|_2^2 + \mu^2 \sum_{k=1}^{M} \frac{m_k^2}{m_k^2 + \varepsilon^2} \right\} \qquad (3.24)$$

The solution of the minimization problem in eq. 3.24 provides compact solutions with the smallest possible volume.

Also this algorithm use a depth weighting function to counteract the decay of kernel with depth (see par.3.2). This function is defined differently with respect to Li and Oldenburg algorithm, but the effect is very similar. Portniaguine and Zhdanov (2002) propose this weighting function:

$$\mathbf{W}_z = \sqrt{\mathbf{S}} \qquad (3.25)$$

where **S** is a diagonal matrix given by:

$$S_k = \sqrt{\sum_i \left(A_{ik}\right)^2} \qquad (3.26)$$

where **A** is the kernel matrix.

So we can write the eq. 3.24 introducing the sensitivity weight $\mathbf{W_z}$

$$\mathbf{m} = \arg\min\left\{\left\|\mathbf{Am}-\mathbf{d}\right\|_2^2 + \mu^2 \sum_{k=1}^{M} \frac{w_k^2 m_k^2}{m_k^2 + \varepsilon^2}\right\} \qquad (3.27)$$

where w_k are the elements of $\mathbf{W_z}$.

Then it is possible to define an iterative diagonal weighting matrix as follow:

$$\mathbf{W_m^2}(m) = diag\left[\mathbf{m}^2 + \varepsilon^2 \mathbf{I}\right]\mathbf{W}_z^{-2} \qquad (3.28)$$

$\mathbf{W_m}$ changes with each iteration. At the first iteration $\mathbf{W_m}=\mathbf{I}$ and we obtain the maximum smoothness solution (Portniaguine and Zhdanov, 2002).

We can write the eq. 3.27 in matrix notation:

$$\mathbf{m} = \arg\min\left\{\left\|\mathbf{AW_m}(\mathbf{m})\mathbf{W_m^{-1}}(\mathbf{m})\mathbf{m}-\mathbf{d}\right\|_2^2 + \mu^2\left\|\mathbf{W_m^{-1}}(\mathbf{m})\mathbf{m}\right\|^2\right\} \qquad (3.29)$$

So the problem in eq. 3.29 is transformed into a space of weighted model $\mathbf{m_w}$ by replacing the variables:

$$\mathbf{m} = \mathbf{W_m}(\mathbf{m})\mathbf{m_w}, \quad \mathbf{A_w} = \mathbf{AW_m}(\mathbf{m}) \qquad (3.30)$$

Substituting equation (3.30) in expression (3.29), we find

$$\mathbf{m} = \arg\min\left\{\left\|\mathbf{A_w m_w}-\mathbf{d}\right\|_2^2 + \mu^2\left\|\mathbf{m_w}\right\|^2\right\} \qquad (3.31)$$

The matrix $\mathbf{W_m}$ and the forward operator $\mathbf{A_w}$ changes with each *k* iteration:

$$\mathbf{W}_{\mathbf{m}}^{(k+1)\mathbf{2}} = diag\left[\mathbf{m}^{(k)2} + \varepsilon^2\mathbf{I}\right]\mathbf{W}_z^{-\mathbf{2}} \qquad (3.32)$$

$$\mathbf{A}_w^{(\mathrm{k}+1)} = \mathbf{A}\mathbf{W}_m^{(\mathrm{k}+1)} \qquad (3.33)$$

Then the problem is solved with respect to $\mathbf{m_w}$**:**

$$\mathbf{m}_w^{(\mathrm{k}+1)} = \mathbf{A}_w^{T(\mathrm{k}+1)}\left[\mathbf{A}_{\mathbf{w}}^{(\mathrm{k}+1)}\mathbf{A}_w^{T(\mathrm{k}+1)}\right]^{-\mathbf{1}}\mathbf{d} \qquad (3.34)$$

$$\mathbf{m}^{(\mathrm{k}+1)} = \mathbf{W}_m^{(\mathrm{k}+1)}\mathbf{m}_w^{(\mathrm{k}+1)} \qquad (3.35)$$

The problem in eq. (3.34) is solved in each step for $\mathbf{m_w}$ with fixed $\mathbf{A_w}$ using the conjugate gradient algorithm. Then, $\mathbf{A_w}$ and **m** are updated at each iteration using eq. 3.33 and 3.35 and $\mathbf{W_m}$(**m**) is updated using equation (3.32). This algorithm generates a set of equivalent solutions of the inverse problem which fit the data with the same accuracy. The different models within this set have different degrees of focusing. The model after the first iteration is actually a maximum smoothness solution. The process continues until the required degree of focusing is reached.

3.7.3 Boundary constrains

The iterations start from the least-squares solution and proceed by increasing the compactness of the model, using the weighting function of equation (3.28) at each step. The effect of this procedure is to increase the densities of some blocks and decrease the densities of most of the others Last and Kubik (1983). With the increase of the iterations at least one block will reach a density which exceeds the postulated density of the body; then, it is necessary to introduce a constraint on the

maximum and minimum value that can be achieved. To do this we follow an algorithm similar to one proposed by Last and Kubik (1983):

$m_i = m_{max_i}$ if $m_i > m_{max_i}$

$m_i = m_{min_i}$ if $m_i < m_{min_i}$

When a cell m_i exceeds its own upper or lower bound on the source density value, the algorithm resets the density of the block equal to m_{max_i} or m_{min_i} and essentially freezes the block out of the next step in the iterative inversion process.

This is done by:

(1) subtracting its gravity effect from the total gravity anomaly;

(2) assigning it a very large weight (in practice ε^{-1}).

This is implemented as follows. After the k^{th} iteration we compute a reduced data vector **d*** with elements:

$$d_i^{*k+1} = d_i - m_{\max} \sum_{i=1}^{N} a_{ij} \theta \left[\frac{m^k}{m_{\max}} \right] \qquad i=1....N \qquad (3.36)$$

a_{ij} is the i^{th}, j^{th} element of the kernel **A**,

θ is the unit Heaviside step function, defined by:

θ(x)=1 if $x \geq 1$

θ(x)=0 if $x < 1$

Then we update the matrix $\mathbf{W_m}$:

$$\left[W_m^{*k+1}\right]_{jj} = \varepsilon + \left[m_j^k\right]^2 Wz_j^{-2}\left\{1 - \theta\left[\frac{m^k}{m_{\max}}\right]\right\} \qquad j=1...M \qquad (3.37)$$

The same is done for the lower boundary m_{min}.

Following this procedure, at iteration *k+1* the value of the model cell m_i that at iteration *k* exceeded m_{max_i} or m_{min_i} will be about 0, because of the large weight given to eq. 3.37. Then, at the end of *k+1* iteration, we sum at this cell the m_{max_i} or m_{min_i} value relative at that cell.

3.7.4 Regularization

The regularization is carried out using the regularized conjugate gradient (Portniaguine and Zhdanov, 2002). In this method the regularization parameter μ changes with CG iterations.

We can write the problem in eq. 3.22 for usage in iterative minimization methods reformulated in block matrix notation:

$$\begin{bmatrix} \mathbf{A} \\ \sqrt{\rho}\mathbf{I} \end{bmatrix}\mathbf{m} = \begin{bmatrix} \mathbf{d} \\ \mathbf{0} \end{bmatrix} \qquad (3.38)$$

where **I** is the identity matrix.

Introducing the block matrices:

$$\mathbf{A}^* = \begin{bmatrix} \mathbf{A} \\ \sqrt{\rho}\mathbf{I} \end{bmatrix} \quad \mathbf{d}^* = \begin{bmatrix} \mathbf{d} \\ \mathbf{0} \end{bmatrix} \qquad (3.39)$$

the eq. 3.22 becames:

$$\mathbf{A^*m=d^*} \qquad (3.40)$$

The problem in eq. (3.40) is clearly overdetermined, because the dimensions of **A*** are (*N*+*M*) x *M*, where *N* is the number of data and *M* is the number of model parameters. For an overdetermined system, the conjugate gradient method converges to the least-squares solution (Portniaguine and Zhdanov, 2002). This is equivalent to the minimization of the parametric functional expressed in combined matrix notations:

$$\left\| \mathbf{A}^* \mathbf{m} - \mathbf{d}^* \right\|_2^2 = \min \qquad (3.41)$$

To select the regularization parameter the typical choice is to use the Tikhonov method. After the first non-regularized iteration, the regularization parameter is set to balance the contribution from misfit (residual) and stabilizing functional:

$$\mu_1 = \left\| \frac{\mathbf{r}_{\mathbf{start}}}{\mathbf{m}_{\mathbf{start}}} \right\|, \quad \mathbf{m}_{\mathbf{start}} = \alpha_1 \mathbf{A}^{\mathbf{T}} \mathbf{d} \ , \quad \mathbf{r}_{\mathbf{start}} = -\mathbf{d} - \alpha_1 \mathbf{A}\mathbf{m} \qquad (3.42)$$

and α_1 is the step length of the first iteration of conjugate gradient.

The subsequent iterative values are determined by :

$$\mu_{k+1} = \frac{\mu_k}{2} \qquad (3.43)$$

3.7.5 Examples

To test this algorithm we use the same synthetic model with two sources at different depth previously used (Fig. 3.3). We also use the same model discretization.

In this case we perform different inversions changing the upper boundary of the magnetization value. In Fig. 3.5a we don't use any upper boundary and as expected we obtain the maximum focused solution. The shallow source is perfectly defined for shape and magnetization value, because it consists of just one cell and then the solution with minimum volume is precisely the correct solution. The deeper source, instead, is over focused and the magnetization value is strongly over estimated. The solution Fig. 3.5b is obtained using an upper boundary value of 1 A/m. This is precisely value of magnetization of shallow source. Obviously this source is once again perfectly determined and the deeper source is better reconstructed than previously case, but the volume is again over focused and the magnetization is over estimated. In Fig. 3.5c, instead, we use 0.25 A/m as upper boundary value, In this case is the deeper source to be perfectly reconstructed for shape and magnetization value, instead the volume of shallow source is overestimated and consequently also the magnetization value is underestimated. Finally, in Fig. 3.5d results obtained by using two upper boundary values, different for the region of shallow and deeper source and we use 1 A/m and 0.25 A/m respectively. In this case the inversion process perfectly reconstruct the shape and magnetization value for both sources.

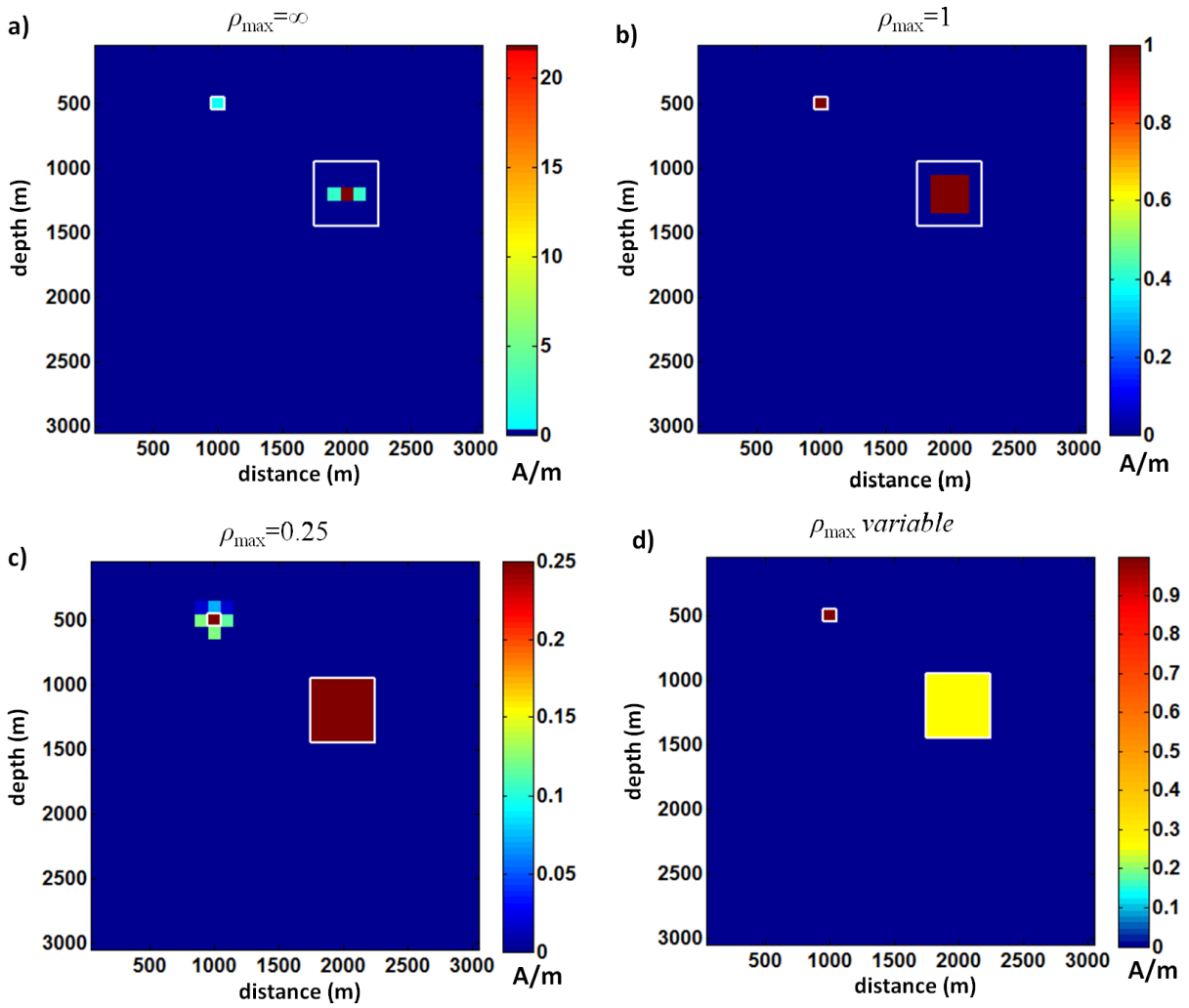

Figure 3.5. *Cross section at y=1500m of focused solutions obtained by inverting the anomalies in Fig. 3.3a and using: a) no upper boundary; b) upper boundary of 1 A/m for the whole model; c) upper boundary of 0.25 A/m for whole model; d) variable upper boundary value of 1 A/m and 0.25 A/m.*

In the above example we assumed to know the upper bound values of magnetization, but if we don't have any idea about the possible range of the model parameter we can't constrain the model. In this case we need to perform many iterations and choose the model that best reflect our idea about the geological model of subsurface. In Fig. 3.6 we show the solutions obtained at 9 iterations; as expected, the compactness of solutions increases with the iteration number.

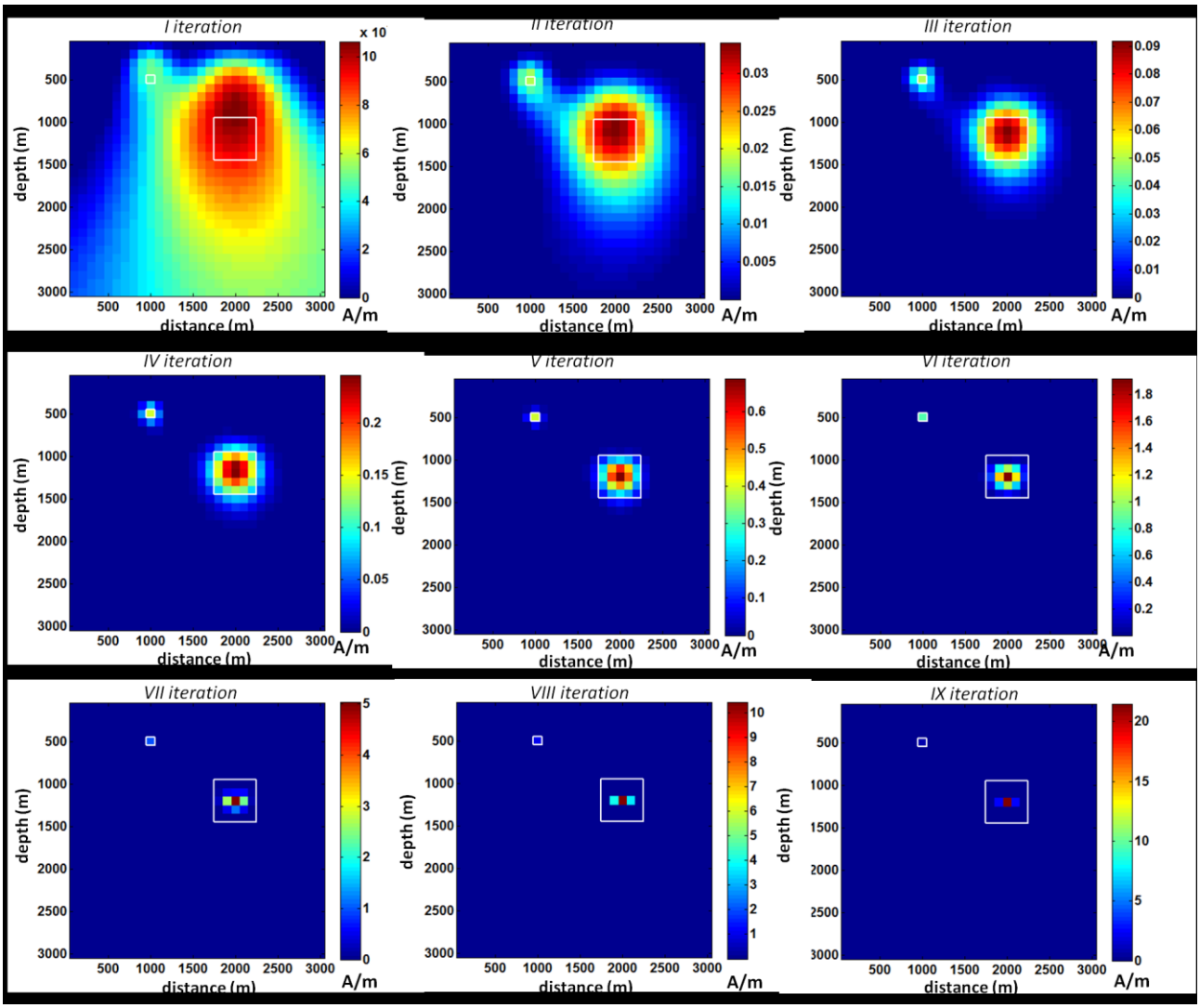

Figure 3.6. *Cross section at y=1500m of focused solutions obtained by inverting the anomalies in Fig. 3.3a without any upper boundary constrain.*

3.8 Data space inversion (Pilkington, 2009)

3.8.1 Introduction

The inversion algorithm proposed by Pilkington, (2009), uses the Cauchy norm (Sacchi and Ulrych, 1995), as a stabilizing functional to solve the 3D magnetic inverse problem for sparse models, in which the number of nonzero values that fit the data is minimized. Model sparseness ensures that the solution is simple and tends to penalize smooth variations, so favoring a blocky character in the source density distribution (Pilkington, 2009). Also this algorithm uses the positivity constraint.

To reduce the computer memory and the CPU time needed to the inversion process, this algorithm presents some new powerful features. The problem is solved in the data space (*N*-dimensional) rather than in the model space (*M*-dimensional), where *N*<<*M*, uses a preconditioned conjugate gradient method to solve the resulting set of linear equations and performs all matrix-vector products in the Fourier domain. This last very interesting feature allows to solve very large-scale problems, because it does not necessarily store the kernel matrix **A,** whose size can be very big.

3.8.2 Forward problem in Fourier domain

Let's consider the classic forward problem in the space domain:

$$\mathbf{d} = \mathbf{Am} \qquad (3.44)$$

As we have already seen in paragraph 3.3, the kernel matrix **A** quantifies the contribution of the j^{th} cell to the i^{th} datum, **m** is the model parameter vector (density or susceptibility) and **d** is data vector.

If all data are regularly spaced on a grid, all model cells have the same shape and dimension and there is one data point per model cell in the horizontal plane. In these conditions we can solve the forward problem in eq. 3.44 in the frequency domain.

The gravity field in the frequency domain resulting from each layer of prismatic cells is given by (Naidu and Mathew, 2008):

$$g_z(u,v,h) = 8\pi\gamma ab\,\mathrm{sinc}(au)\,\mathrm{sinc}(bv)\frac{exp(-sh)}{s}(1-exp(-2cs))\cdot F[\rho(r)] \quad (3.45)$$

where:

γ is gravitational constant;

a, *b* and *c* are the dimension of the cell along *x*, *y* and z direction respectively;

h is the depth to the top of the layer;

u and *v* are the wavenumbers in *x* and *y* directions respectively;

s is given by:

$$s = \sqrt{u^2 + v^2}$$

$F[\rho(r)]$ is the Fourier transform of the density distribution within the layer.

The gravity field in the frequency domain, resulting from total 3D model, is the sum of effect of each layer:

$$g_z(u,v) = 8\pi\gamma ab\,\mathrm{sinc}(au)\,\mathrm{sinc}(bv)\sum_{l=1}^{Nl}\frac{exp(-sh)}{s}(1-exp(-2cs))\cdot F[\rho_l(r)] \quad (3.46)$$

where *Nl* is the number of layers of the model.

The corresponding expression for the magnetic field in the frequency domain is (Naidu and Mathew, 2008):

$$T(u,v) = 8\pi\gamma ab\left(j\alpha u + j\beta v - s\gamma\right)\left(juI_x + jvI_y - sI_z\right)$$
$$\times \operatorname{sinc}(au)\operatorname{sinc}(bv)\sum_{l=1}^{Nl}\frac{exp(-sh)}{s^2}(1-exp(-2cs))\cdot F\left[\chi_l(r)\right] \qquad (3.47)$$

where α, β and γ are the direction cosines of the earth's magnetic field in free space, I_x, I_y, and I_z are the direction cosines of the magnetization.

$F[\chi(r)]$ is the Fourier transform of the susceptibility distribution within the layer.

3.8.3 The algorithm

The standard least-squares solution of equation 3.44 leads to a system based on the *M* X *M* (*M*= number of model parameter) matrix A^TA. Explicitly forming and finding the inverse of this matrix is impractical because of its size especially in large scale 3D problems (Pilkington, 2009).

In paragraph 2.7, eq. 2.21 and 2.13, we have seen an important equivalence allowing to express the same problem in terms of a system based on the *N*X*N* matrix $\mathbf{AA^T}$, rather than $\mathbf{A^TA}$**.** A similar problem is thus solved in data space instead than in the model space. This approach reduces considerably the computationally load and the CPU time.

Furthermore, the greater stability of the system based on the matrix $\mathbf{AA}^{\boldsymbol{T}}$ versus that based on $\mathbf{A}^{\boldsymbol{T}}\mathbf{A}$ implies that finding a suitable regularization parameter, which often requires repeated solving of the resulting system of equations, now requires less computational effort (Pilkington, 2009).

As previous algorithms, also this one uses a depth weighting function to counteract the kernel decay, defined likewise Li and Oldenburg (1996):

$$Z = \frac{1}{(z)^{\beta}} \qquad (3.48)$$

Pilkington (2009) uses β=3 for the magnetic case.

The positivity is imposed by transforming the model parameters into some function that might take on positive and negative values, but when inverse transformed (back into density or susceptibilities) gives only positive values (Pilkington, 2009).
Pilkington, (2009) uses the square root function to estimate the square root of model parameters values. Lelièvre and Oldenburg (2006) show that the Jacobian matrix needed for inversion has elements $a_{ij} \cdot 2m_j$.

Consider the minimization of the follow objective function:

$$(\mathbf{d} - \mathbf{Am})^{\mathrm{T}} \mathbf{D}^{-1} (\mathbf{d} - \mathbf{Am}) + C(\mathbf{m} - \mathbf{m_0}) \qquad (3.49)$$

the first term is the weighted data misfit with **D** diagonal weighting matrix, usually consisting of the estimated data-error variances, the second term is the model objective function $C(\mathbf{m})$ and consists of two parts: the depth-weighting function $Z(\mathbf{m})$ (eq. 3.48), plus a model norm term $P(\mathbf{m})$.
To impose sparseness constraints on the model **m**, the Cauchy norm $P(\mathbf{m})$ is used:

$$P(\mathbf{m}) = \sum_{i=1}^{M} \ln\left(1 + m_i^2 / \sigma^2\right) \qquad (3.50)$$

The level of sparseness is controlled by the parameter σ. $P(\mathbf{m})$ becomes small when the number of parameters m_i having amplitudes less than σ tends to increase. If σ is set too low, then the resulting nonzero values in **m** tend to become more isolated, assuming unrealistically large amplitudes (no upper bound on model values is used in the inversion). If σ is large compared with all the elements of **m**, then $P(\mathbf{m})$ has an effect similar to the minimum-norm solution and has no influence on sparseness of the model (Pilkington, 2009).

The choice of σ depends by the level of sparseness to be obtained according to available geological information.

The minimization of the function in eq. 3.50 is carried out iteratively :

$$\mathbf{m_{k+1}} = \mathbf{m_k} + \Delta\mathbf{m}_k \qquad (3.51)$$

Iterations proceed until the rms misfit reaches an acceptable level or the model corrections become acceptably small.

At iteration *k,* $\Delta\mathbf{m_k}$ expressed in data space is given by:

$$\begin{aligned}\Delta\mathbf{m_k} &= \mathbf{m_k} - \mathbf{m}_0 = \alpha\mathbf{W}_{\mathbf{m}_k}\mathbf{S}_\mathbf{k}^\mathbf{T}\mathbf{A}^\mathbf{T}\left(\mathbf{A}\mathbf{S}_\mathbf{k}\mathbf{W}_{\mathbf{m}_k}\mathbf{S}_\mathbf{k}^\mathbf{T}\mathbf{A}^\mathbf{T} + \mathbf{D}\right)^{-1} \\ &\times\left(\mathbf{d} - \mathbf{A}\mathbf{m_k} + \mathbf{A}\mathbf{S_k}\left[\mathbf{m_k} - \mathbf{m_0}\right]\right)\end{aligned} \qquad (3.52)$$

where $\mathbf{m_k}$ is the current model and the constant α is a step length, initially α is set to unity and then reduced by a factor of 3 until a reduction in the misfit is achieved.

$\mathbf{Wm_k}$ is a *M* X *M* diagonal matrix with depth weighting and sparseness constraints whose elements are:

$$w_{ii} = z_l^{\beta}\left(1 + m_i^2/\sigma^2\right) \qquad i=1\ldots M \qquad (3.53)$$

where z_l is the depth to the *l*th layer.

$\mathbf{S_k}$ is a diagonal matrix used to impose the positivity, with elements:

$s_{ii} = 2m_i$

It is possible to write the eq. 3.52 in compact form:

$$\Delta \mathbf{m_k} = \alpha \mathbf{W}_{\mathbf{m_k}} \mathbf{S_k^T A^T b_k} \qquad (3.54)$$

where

$$\mathbf{b_k} = \left(\mathbf{A S_k W}_{\mathbf{m_k}} \mathbf{S_k^T A^T} + \mathbf{D}\right)^{-1} \left(\mathbf{d} - \mathbf{A m_k} + \mathbf{A S_k}\left[\mathbf{m_k} - \mathbf{m_0}\right]\right) \quad (3.55)$$

$\mathbf{b_k}$ is found at each iteration by solving the following system using the conjugate gradient (CG) method:

$$\mathbf{f_k} = \mathbf{G_k b_k} \qquad (3.57)$$

where

$$\mathbf{G_k} = \left(\mathbf{A S_k W}_{\mathbf{m_k}} \mathbf{S_k^T A^T} + \mathbf{D}\right) \qquad (3.58)$$

and

$$\mathbf{f_k} = \left(\mathbf{d} - \mathbf{A m_k} + \mathbf{A S_k}\left[\mathbf{m_k} - \mathbf{m_0}\right]\right) \qquad (3.59)$$

We have already said in paragraph 1.4 that the CG algorithm is a very efficient method to solve large systems, because requires only matrix-vector product of type $\mathbf{Ap}$ and $\mathbf{A^T q}$ where $\mathbf{p}$ and $\mathbf{q}$ are some vectors with dimensions of *M* and *N*

respectively. Previously we saw that we can carried out the product **Ap** in Fourier domain reducing drastically the computational memory and time, the same is true for the product $\mathbf{A}^T\mathbf{q}$. The use of CG algorithm with products in frequency domain allow to solve quickly very large scale system (Pilkington, 2009).

To improve the efficiency of the algorithm we can use a preconditioner (see par. 2.7) that consist of just the inverse of diagonal elements of $\mathbf{G}_k$.

3.8.4 Example

To test this last algorithm we use the same synthetic problem show in Fig. 3.3a. In this case we perform different inversions using different values of σ parameter. As explained before, this parameter controls the sparseness level of the solution. The results of 4 inversions using, respectively σ=1, 0.25, 0.22 and 0.001, are shown in Fig. 3.7 Using σ = 1 (Fig. 3.7a) the sparseness constraint is not used. The solution is however more compact than the solution obtained using the Li and Oldenburg algorithm; this is due to the fact that the inversion is performed in the data space rather than in the model space.

As is it possible to see, decreasing the value of σ, increase the sparseness level and consequently the compactness of the solution. Similarly to the focusing inversion, increasing the compactness increases also the magnetization value and this can be overestimated. This algorithm does not include the possibility to use an upper boundary value and consequently the degree of compactness of the solution must be controlled only by σ parameter.

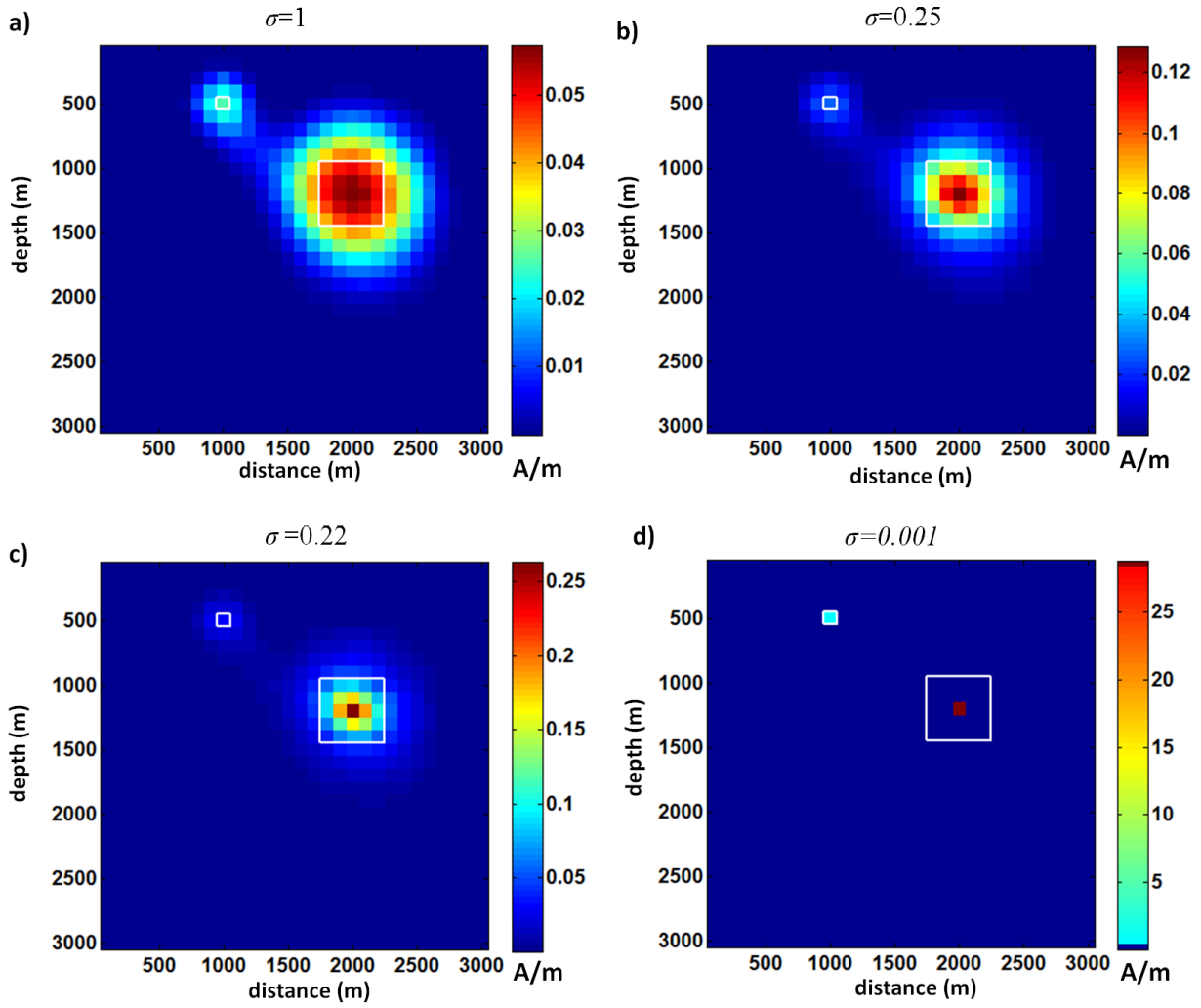

Figure 3.7. *Cross section at y=1500m of data space inversion solutions with different values of the sparseness constraints: a) σ=1, b) σ=0.25, d) σ=0.23, d) σ=0.001.*

CHAPTER IV

Invariance rules in the inversion of gravity and magnetic fields and their derivatives

4.1 Introduction

In the paragraph 3.2 we have introduced the problem of the minimum length solution and we showed that this is characterized by model parameter values as close as possible to zero. This leads to a distribution of the unknown density or susceptibility, which is very shallow and not representative of the true source distribution (Fig. 3.1). In fact, requiring the solution to be small corresponds to find a solution corresponding to the shallowest source distribution compatible with the measured data. More realistic models of the distribution of the physical property at depth can however be obtained by introducing a "depth weighting" in the problem, able to counteract the natural decay of the kernel. Li and Oldenburg (1996), (see paragraph 3.6) proposed to use a depth weighting function such as:

$$w(z) = \frac{1}{(z+q)^{\beta/2}} \qquad (4.1)$$

where z is the depth of the layers and q depends on the height of survey. They suggested to use β = 2 in the gravity case and β = 3 in the magnetic case, corresponding to the fall-off rates of the field produced by a small cubic cell in the gravity and magnetic cases, respectively. Thus, Li and Oldenburg (1996) and Li and Oldenburg (1998) chose to 'tune' their depth-weighting function according to the power-law decay of the field produced by one single cell in the source domain. Fedi and Cella (2012) showed instead that the appropriate value of β must be related to N, the structural index of the source (Table 4.1), rather than to the power-law decay

of the field generated by a single cell. The structural index may be, in turn, estimated with standard methods such as Euler Deconvolution or the study of the scaling function (Fedi, 2007; Florio et al., 2009).

SOURCE	N(gravity)	N(magnetism)
sphere	$2+k$	$3+k$
cylinder	$1+k$	$2+k$
sill/dike	$0+k$	$1+k$
contact	$-1+k$	$0+k$

Table 1. Structural index (k=order of differentiation)

In this section we will show the existence of invariance rules occurring in the inversion of potential fields of different orders. These invariance rules assure that the same solution is obtained inverting the magnetic (or gravity) field or any of its k^{th} order vertical derivatives. Such invariance will be rigorously derived for the minimum length solution and shown to occur also in the regularized inversion with depth-weighting and positivity constraints. A further invariance rule regards the homogeneity of the magnetization/density distribution. If the field is homogeneous, the obtained magnetization/density distribution models will be homogenous functions of the same degree of the magnetic field or of the vertical derivative of the gravity field, respectively, no matter the order k of the vertical differentiation of the field.

4.2 Cribb's theory: magnetic field

Consider the classic problem:

$$\mathbf{d} = \mathbf{Am} \qquad (4.2)$$

where **d** is the column vector of the observation data (magnetic or gravity field), **m** is the column vector of the unknown (susceptibility/magnetization or density) and **A** is the rectangular kernel matrix. As already described in section 2.3, if the number of unknowns is much greater than the number of data, the simplest solution of the system (4.2) is the minimum-length solution, given by (e.g., Menke, 1984):

$$\mathbf{m} = \mathbf{A}^{\mathrm{T}}\left(\mathbf{A}\mathbf{A}^{\mathrm{T}}\right)^{-1}\mathbf{d} \qquad (4.3)$$

Cribb (1976) showed that the minimum-length solution for the magnetic problem is proportional to the upward continuation of the magnetic field and gave its expression in the Fourier domain as:

$$\widetilde{m}_i = 4e^{-z_i s}\widetilde{T} \qquad i=1,\ldots, L \qquad (4.4)$$

where L is the number of layers of the model, T is the magnetic field, z_i is the layer depth, $\widetilde{m}_i$ and $\widetilde{T}$ are, respectively, the two-dimensional Fourier transforms of the source density distribution of the i^{th} layer $m_i(x,y)$ and of the observed data; $s=(u^2+v^2)^{1/2}$, with u and v being the wavenumbers in the x and y directions.

Being $e^{-z_i s}\widetilde{T}$ the magnetic field at the altitude z_i, it is important to note that equation (4.4) expresses an important property for homogeneous magnetic fields, namely that if the field T is homogeneous of degree $-n$, the magnetization distribution is also a homogeneous function of the same degree.

4.3 Cribb's theory: gravity field

In the case of the gravity problem, Cribb (1976) showed that the minimum-length solution is proportional to the upward continuation of the vertical derivative of the observed gravity field:

$$\widetilde{\rho}_i = \frac{1}{\pi\gamma} e^{-z_i s} s\widetilde{g} = \frac{1}{\pi\gamma} e^{-z_i s} \widetilde{g}^{(1)} \qquad i=1,\ldots, L \tag{4.5}$$

where γ is the gravitational constant, $\widetilde{\rho}_i$ is the two-dimensional Fourier transforms of the source density distribution of the i^{th} layer $\rho_i(x,y)$, and $\widetilde{g}^{(1)}$ is the Fourier transform of $\frac{\partial g}{\partial z}$.

Similarly, to the magnetic case, eg being $e^{-z_i s}\widetilde{g}^{(1)}$ the vertical derivative of the gravity field at the altitude z_i, we note that equation (4.5) expresses the important property that if the field g is homogeneous of degree $-n$, the density distribution is also a homogeneous function, having the same homogeneity degree of the vertical derivative of the gravity field, that is $-n-1$.

4.4 Invariance rules for the minimum length solution

In order to define invariance rules for the minimum length solution, first we need to extend the Cribb's relation (4.5) to the case of the k^{th} vertical derivative of the magnetic field.

We can use the fact that the Fourier transform of the k^{th}vertical derivative of the magnetic field is given by (e.g., Blakely, 1996):

$$T^{(k)} = \frac{\partial^k T}{\partial z^k}$$

$$\widetilde{T}^{(k)} = s^k \widetilde{T} \qquad (4.6)$$

and, by using the inverse of the vertical differentiation operator, we obtain from equation (4.6):

$$\widetilde{T} = s^{-k} \widetilde{T}^{(k)} \qquad (4.7)$$

Thanks to equation (4.7), it is now easy to generalize Cribb's relation (4.4) to the case of the k^{th} vertical derivative of the magnetic field:

$$\widetilde{m}_i = 4e^{-z_i s} s^{-k} \widetilde{T}^{(k)} = 4e^{-z_i s} T \qquad i=1,\ldots, L \qquad (4.8)$$

where $T^{(k)}$ represents the vertical integral of the field if k=-1, the magnetic field if k=0, the first vertical derivative of the magnetic field if k=1, and so on.

Equation (4.8) expresses an invariance rule for the minimum length solution: in fact the minimum-length solution for the k^{th} order vertical derivative of the magnetic field does not depend on the order of differentiation of the magnetic field, but always corresponds to that of the magnetic field (equation 4.4). From equation (4.8) we can also argue another invariant property for the magnetization distribution: if T is homogeneous of degree n, and so its k-order vertical derivative is homogeneous of order n-k, the magnetization m will be a homogeneous function of order n, independent on the differentiation order k of the field.

Based on the above reasoning, it is easy to obtain also for the gravity problem an invariant formula for the minimum length solution:

$$\tilde{\rho}_i = \frac{1}{\pi\gamma} e^{-z_i s} s^{-(k-1)} \tilde{g}^k = \frac{1}{\pi\gamma} e^{-z_i s} \tilde{g}^{(1)} \qquad i=1,\ldots, L \qquad (4.9)$$

where $g^{(k)}$ represents the gravity field if k=0, the first vertical derivative of the gravity field if k=1 and so on.

From equation (4.9) we can obtain a further invariant property for the density distribution: if g is homogeneous of degree n, so that its k-order vertical derivative is homogeneous of order n-k, the density ρ will be a homogeneous function of order $n+1$, independent on the differentiation order k of the field.

To illustrate the meaning of the invariance laws (4.8) and (4.9) we show in Fig. 4.1 the minimum-length solutions for the vertically-integrated magnetic field, k=-1, for the magnetic field, k=0 and for the first vertical derivative of the magnetic field, k=1. All the fields are calculated at the magnetic pole and the source is a cubic cell at x=20 km, z=5 km, with vertical magnetization of 1 A/m. The 3D source domain was discretized by means of 40x40x15 cubic cells, each sized 1x1x1 km^3 and the solutions were obtained by inverting a 40x40 data grid, the data being 1 km spaced.

It is evident that the three solutions are the same, independently of the data differentiation order k, in perfect agreement with the invariance rule (4.8).

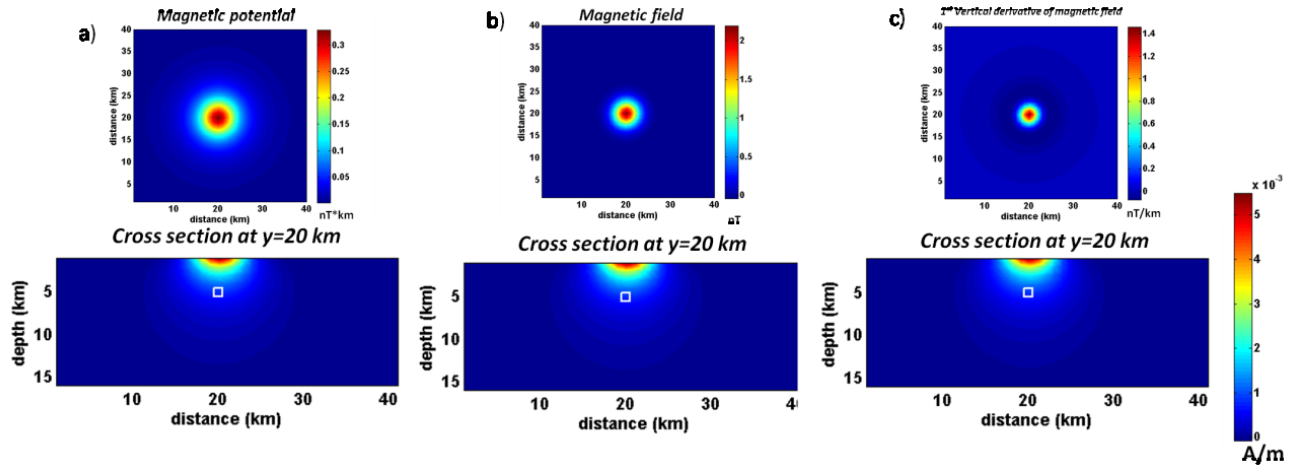

Figure 4.1. *Minimum length solution for: a) magnetic potential; b) magnetic field; c)1stvertical derivative of magnetic field. We assumed a vertical direction for both the inducing field and the magnetization vector. The white square indicates the true position of the source.*

4.5 Invariance rules: Tikhonov solution (noise free case)

In this section we investigate the invariance properties of the solutions obtained in the important case of the regularization with depth weighting.

Give the problem (4.2):

$$\mathbf{Am} = \mathbf{d}$$

and the minimum length solution (4.3):

$$\mathbf{m} = \mathbf{A}^{\mathrm{T}}\left[\mathbf{A}\mathbf{A}^{\mathrm{T}}\right]^{-1}\mathbf{d}$$

The problem in (1) can be rewritten in the equivalent form:

$$\mathbf{DAm} = \mathbf{Dd} \qquad (4.10)$$

where **D** is any invertible linear operator matrix like derivative.

Note that the linear operator of directional derivative is invertible in the vectorial quotient space, that is whenever we consider equivalent two functions differing for just a constant level.

The corresponding *minimum length solution* is:

$$\mathbf{m} = (\mathbf{DA})^{\mathrm{T}}\left[(\mathbf{DA})(\mathbf{DA})^{\mathrm{T}}\right]^{-1}\mathbf{Dd} \qquad (4.11)$$

In Appendix B we demonstrate mathematically the equivalence between eq. 4.11 and eq. 4.3 and we can write:

$$\mathbf{m} = (\mathbf{DA})^{\mathrm{T}}\left[(\mathbf{DA})(\mathbf{DA})^{\mathrm{T}}\right]^{-1}\mathbf{D} = \mathbf{A}^{\mathrm{T}}\left[\mathbf{A}\mathbf{A}^{\mathrm{T}}\right]^{-1}\mathbf{d} \qquad (4.12)$$

The eq. 4.12 is an alternatively demonstration of invariance rule for minimum length solution.

Now we extend this invariance rule also to regularized case with depth weighting. In Chapter 2 we have introduced the *weighted minimum length solution* for the problem in (4.2):

$$\mathbf{m} = \mathbf{W}_{\mathbf{m}}\mathbf{A}^{\mathrm{T}}\left[\mathbf{A}\mathbf{W}_{\mathbf{m}}\mathbf{A}^{\mathrm{T}}\right]\mathbf{d} \qquad (4.13)$$

In this case $\mathbf{W_m}$ is just the depth weighting function (eq. 3.1) and we consider $\mathbf{m_0} = 0$

Now we can also write the corresponding *weighted minimum length solution* to the problem in (4.10):

$$\mathbf{m} = \mathbf{W_m}(\mathbf{DA})^{\mathrm{T}}\left[(\mathbf{DA})\mathbf{W_m}(\mathbf{DA})^{\mathrm{T}}\right]^{-1}\mathbf{Dd} \qquad (4.14)$$

Also in this case In Appendix B we demonstrate mathematically the equivalence between eq. 4.14 and eq. 4.13 and we can write:

$$\mathbf{m} = \mathbf{W_m}(\mathbf{DA})^{\mathrm{T}}\left[(\mathbf{DA})\mathbf{W_m}(\mathbf{DA})^{\mathrm{T}}\right]^{-1}\mathbf{D} = \mathbf{W_m}\mathbf{A}^{\mathrm{T}}\left[\mathbf{A}\mathbf{W_m}\mathbf{A}^{\mathrm{T}}\right]\mathbf{d} \qquad (4.15)$$

The eq. 4.15 represent the invariance rule for the *weighted minimum length solution.*

Furthermore to respect the invariance of solution, the weight in $\mathbf{W_m}$ must be the same, therefore the exponent of weighting function (β) must not change with order of differentiation.

Now we consider the Tikhonov regularization with depth weighting and positivity constraints. We adopt the Li and Oldenburg (2003) formulation of the objective function with the logarithmic barrier:

$$\varphi(\lambda) = \varphi_d + \mu\varphi_m - 2\lambda\sum_{i=1}^{M}\ln(m_j) \qquad (4.16)$$

where μ is the regularization parameter, λ is the barrier parameter φ_d is the weighted data misfit and φ_m is the model objective function. The weighted data misfit is given by:

$$\phi_d = \left\|\mathbf{W_d}\left(\mathbf{d} - \mathbf{d_{obs}}\right)\right\|^2 \qquad (4.17)$$

where d are the predicted data, d_{obs} are the observed data-vector and W_d is the inverse data covariance matrix. The model objective function is given by:

$$\begin{cases} \varphi_m(m) = \alpha_s \int_{vol} w_s w^2(z)(m - m_0)^2 dv + a_x \int_{vol} w_x \left(\frac{\partial w(z)(m - m_0)}{\partial x} \right)^2 dv + \\ a_y \int_{vol} w_y \left(\frac{\partial w(z)(m - m_0)}{\partial y} \right)^2 dv + a_z \int_{vol} w_z \left(\frac{\partial w(z)(m - m_0)}{\partial z} \right)^2 dv \end{cases} \quad (4.18)$$

where m is the unknown model, m_0 is a reference model and $w(z)$ is the depth-weighting function (equation 4.1); $\alpha_s, \alpha_x, \alpha_y, \alpha_z$ are coefficients controlling the importance of each term; w_s, w_x, w_y, w_z are weighting functions to input additional prior information about susceptibility model (a detailed analysis of this inversion scheme is given in Section 3.6).

In the following we will set α_s=0.001, α_x=α_y=α_z=1, $\mathbf{m_0}$=0 and $\mathbf{w_s}$, $\mathbf{w_x}$,$\mathbf{w_y}$,$\mathbf{w_z}$ as identity matrices. We will also assume noise-free data and the same source as in Fig. 4.1.

Let us now verify if the invariance of the minimum-length inverse solution could extend also to our regularized depth-weighting inversion with positivity constraints.

First of all, differently from the minimum length case, we have now to fix the value of the exponent β in equation (4.1), related to the depth weighting. In the magnetic case, according to Fedi and Cella (2012), β=3 is a suitable depth weighting exponent for this source, since the structural index for a single small cell can be approximated by that of a dipole or homogeneous sphere (N=3). Similarly, one would expect β=2 for the magnetic potential and β=4 for the 1st order vertical derivative of the field, since N will be respectively equal to 2 (N=2 for a dipole model) in the case of the magnetic potential and to 4 (N=4 for a dipole model) for the 1st order vertical derivative of the magnetic field. Note that in this case, that is a field decaying as that of a dipole, the Fedi and Cella (2012) selection for β is equivalent to that proposed by Li and Oldenburg, based on the power-law decay of the field produced by one

single small cell in the source domain. However, with this choice the solution (Fig. 4.2) obtained for the magnetic potential (Fig. 4.2a) is too shallow, and that obtained for the vertical derivative (Fig. 4.2b) is too deep. Only the solution for the magnetic field is therefore correct.

However we recall that the magnetization distribution has the same homogeneity degree of the magnetic field (equation 4.4). So, for a dipole source: n=-3 and N=-n=3. Thus we can argue that, independently on the differentiation order k, the optimal choice is always β=3, because it is based on relating the depth weighting function to the homogeneity degree of the magnetization source distribution and not to that of the field. Comparing the so obtained magnetization models (Fig. 4.2c; d; e), we see in fact that:

a) this choice allows the depth to be correctly recovered in all the three cases;
b) the source magnetization models are equivalent, no matter the order of differentiation k.

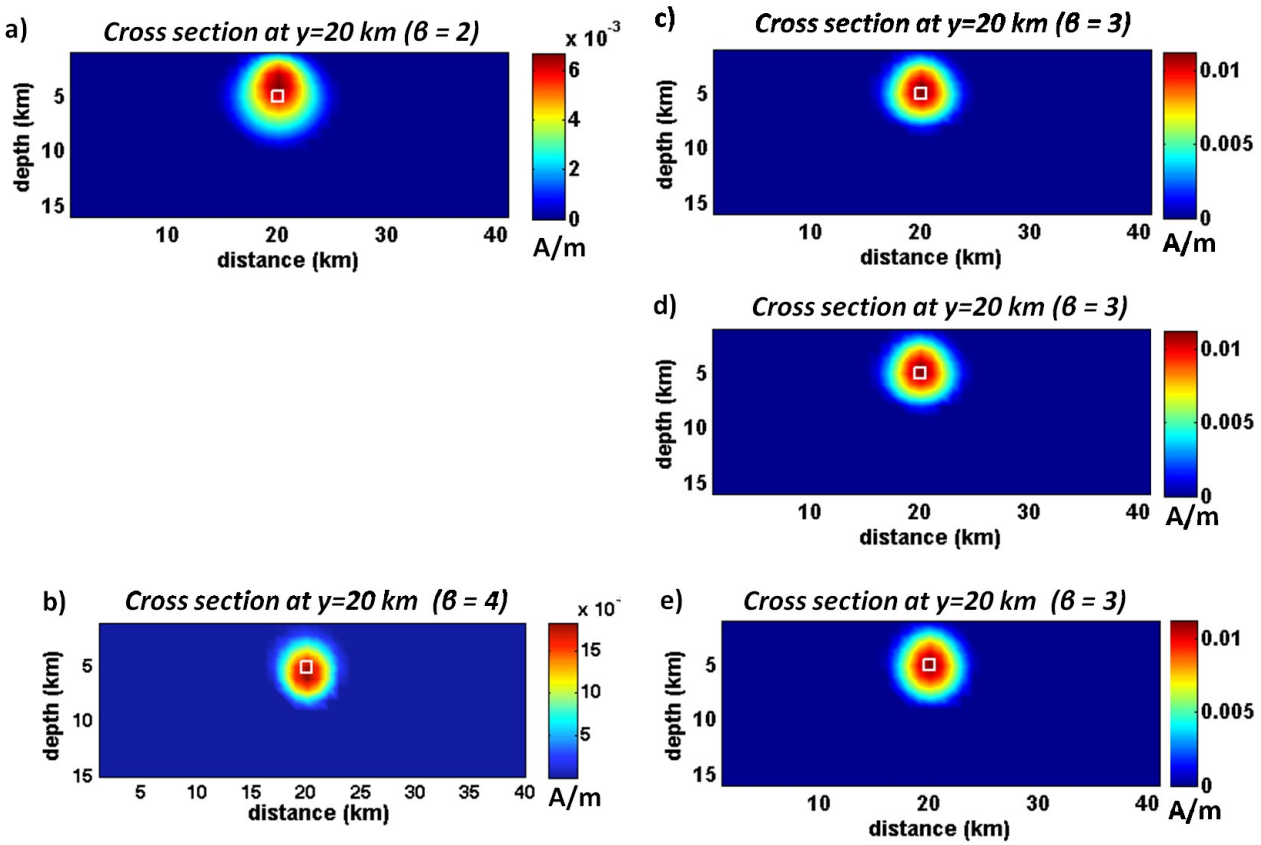

Figure 4.2. *Cross section (at y=20 km) of the magnetization model, obtained from inversion of: (a) magnetic potential, using β=2; (b) 1st vertical derivative of magnetic field, using β=4; (c) magnetic potential, using β=3; (d) magnetic field, using β=3; (e) 1st vertical derivative of magnetic field, using β=3. We assumed a vertical direction for both the inducing field and the magnetization vector.*

We may therefore conclude that, similarly to the minimum-length inverse case, the solution of the regularized inverse problem (4.18) is also invariant with respect to the magnetic field and it derivatives of order *k*, provided the depth weighting function exponent is chosen according to the structural index of the magnetic case.

We tested this rule for a number of different sources (lines, sheets or contacts), each one having a different structural index. In all these cases we always verified the invariance rule, provided that the correct value of β is used, corresponding to the structural index of the magnetic field of these sources.

4.6 The combined effect of depth weighting and regularization parameter (noisy case)

The essence of Tikhonov regularization is that the regularized solution would be sufficiently regular and, at the same time, would fit the data well enough. This is in practice determined by a suitable choice of the regularization parameter μ. In the noise-free case, μ was taken very small to get a slightly regularized solution providing a good data fit. In a general case, however, including the case of noisy data, we usually select higher values of μ to control the model norm and get a solution sufficiently smooth, where most of the large noise components are suppressed. We now investigate on how the source model is affected by varying the regularization parameter.

In our algorithm we have two ways to choose the regularization parameter μ.The first is the χ^2 method. Assuming a zero-mean Gaussian noise for each datum, the data misfit defined by equation (4.17) has a known expected value φ_d*, equal to the number of data (Li and Oldenburg 2003). So we choose the regularization parameter μ such that the value of data misfit φ_d is equal to φ_d*. However, in most cases the estimate of the data error is not available. Then the degree of regularization, and hence the value of μ, needs to be determined based on other criteria.

One more method used in linear inverse problems is the generalized cross-validation (GCV) technique. According to Li and Oldenburg (2003), the minimum of the GCV function:

$$GCV(\mu)=\frac{\left\|\left[\mathbf{I}-\mathbf{G}\left(\mathbf{G}^{\mathrm{T}}\mathbf{G}+\mu\mathbf{W}_{\mathbf{m}}^{\mathrm{T}}\mathbf{W}_{\mathbf{m}}\right)^{-1}\mathbf{G}^{\mathrm{T}}\right]\mathbf{d}\right\|^{2}}{\left\{N-\mathrm{trace}\left[\mathbf{G}\left(\mathbf{G}^{\mathrm{T}}\mathbf{G}+\mu\mathbf{W}_{\mathbf{m}}^{\mathrm{T}}\mathbf{W}_{\mathbf{m}}\right)^{-1}\mathbf{G}^{\mathrm{T}}\right]\right\}^{2}} \qquad (4.19)$$

can be used to select the optimal μ. (see Section 3.6.3).

In this section we study the combined effect of the depth weighting and of the regularization parameter μ obtained using both methods.

To this end we analyze a simple gravity case of a 40x40 dataset, with a 1 km spacing; the data have been contaminated by independent Gaussian noise having a zero mean and a standard deviation of 5% of each data plus 2% of the data maximum (Fig. 3a); the source is a block at *x*=20 km, *z*=5 km with 1 g/cm^3 density. The 3D source domain was discretized as 40x40x15 cubic cells, each sized 1x1x1 km^3.

Fig. 4.3 (b-c) shows different source models obtained minimizing the objective function (4.10) varying the depth weighting function exponent β and using the regularization parameter μ such that the value of data misfit φ_d* is equal to the number of data. In this case, according to the invariance rule established in the previous section, we used β=3 and computed the optimal regularization parameter by the χ^2 criterion, yielding μ=1.0585e+4. However, contrarily to the previous case, the depth is overestimated (Fig. 4.3b). The difference with the previous noise-free case is that now the solution is regularized. So, we tried to change the value of β to get the best solution, and obtained a good estimate of the source depth for β=2 and μ=1.9613e+3 (Fig. 4.3c). However, the stronger regularization produces a solution smoother than the previous case, especially at depth.

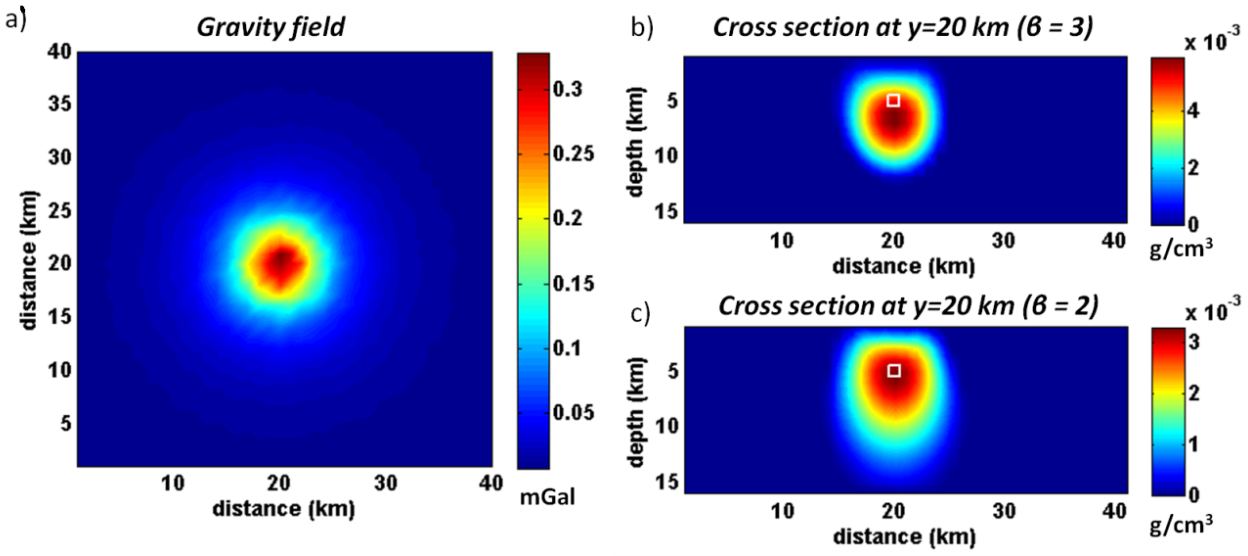

Figure 4.3. *Gravity field corrupted with Gaussian noise (a) and cross section (at y=20 km) of the density model obtained from inverting the gravity field using β=3 (b) and β=2 (c) using a value for β such that the value of data misfit φ_d* is equal to the number of data. The white square indicates the true position of the source.*

We show now the case of automatic estimation of the regularization parameter after minimization of the GCV function. Once again, according to the invariance rule established in the previous section, we used β=3 and computed the optimal GCV regularization parameter, yielding μ=177 (much smaller than the value obtained by the χ^2method). Now, the obtained source model yields a correct estimate of the source depth (Fig. 4.4a). Note also that the model has a much better resolution than the best solution obtained using a value of μ determined by the χ^2 method (Fig. 4.3c). In Fig. 4b we show the source model obtained using β=2 and the value of μ estimated by the GCV method, μ=64. The found solution is however too shallow, with respect to the true depth. We conclude that considering also that GCV does not need the estimate of data errors this criterion is likely to suggest an optimal regularization parameter, which allows us to find a correct source distribution model, according to the invariance criterion described in the previous section. Similar results can be obtained also by inverting vertical derivatives of the field. In

conclusion, it should be considered the fact that a strong regularization tends to overestimate the source depth, so that a correct choice of the regularization parameter is very important. Here we found that the GCV gives better estimates of μ than χ^2 criterion. Of course, there are other estimators of μ (e.g., L-curve method) that can be used to estimate the regularization parameter.

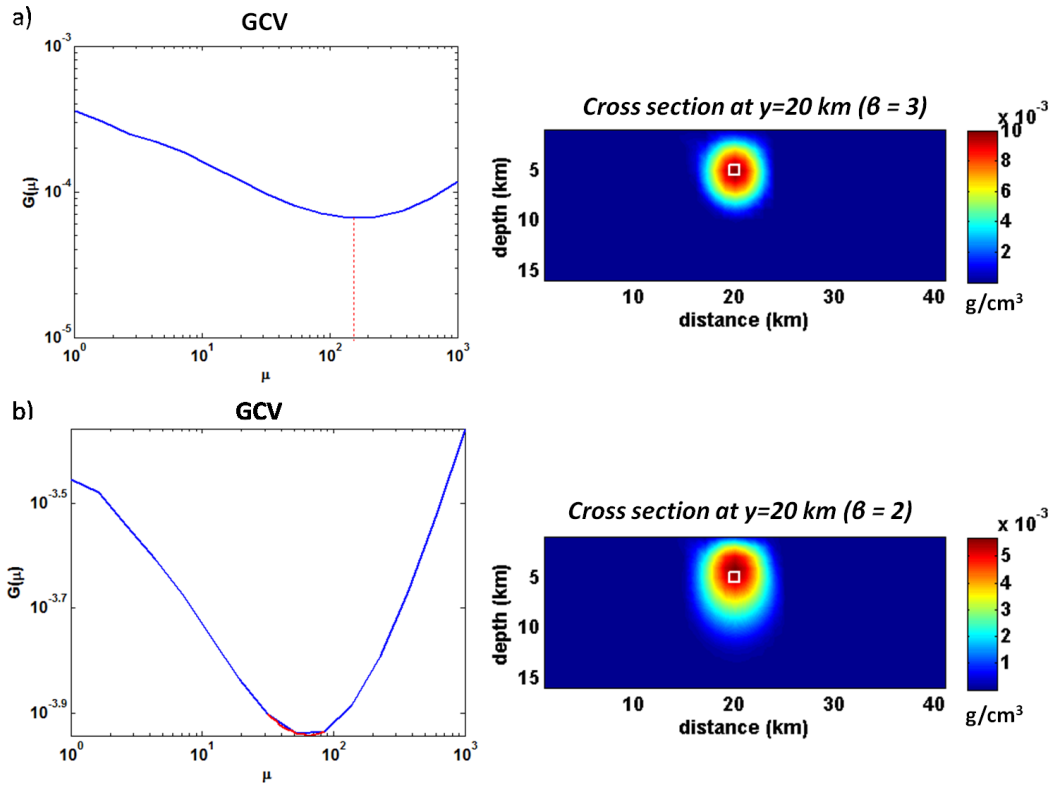

Figure 4.4. *a) GCV function and cross section (at y=20 km) of the density model obtained from inverting the gravity field (Fig. 3a) using β=3 and μ=177, this last obtained by GCV. b) GCV function and cross section (at y=20 km) of density model obtained from inverting gravity field (Fig. 3a) using β=2 and μ=64. The white square indicates the true position of the source.*

4.7 Synthetic case: two sources

In this Section we will show the validity of the invariance rules for a synthetic anomaly (Fig. 4.5a) composed by two different sources at two different depths (Fig. 4.5b). The shallow source is sized 100 x 100 x 100 m^3 and depth to center z=450 m, with a 100 m^3 volume and 1 A/m magnetization; the deepest source is sized 500 x 500 x 500 m^3 and extend from z=900 m to z= 1400 m with a 0.25 A/m magnetization. The magnetic potential generated by the two sources shows a strong interference, with the deepest source being the main contributor to the potential (Fig. 4.5a).

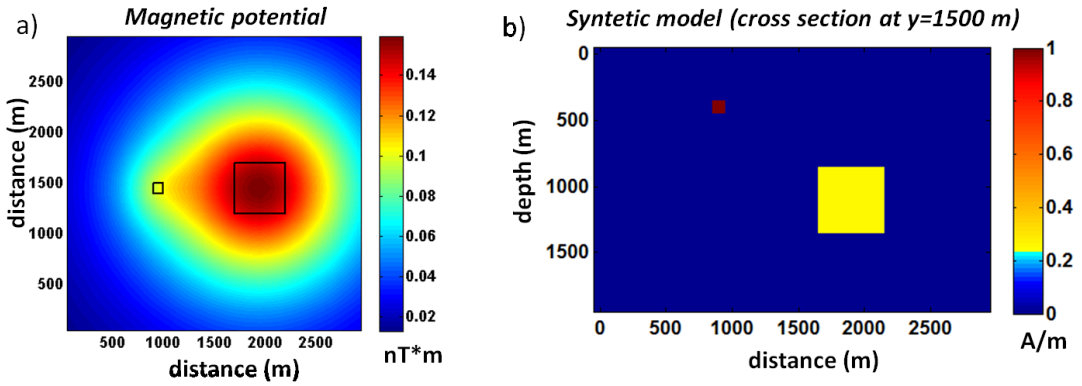

Figure 4.5. *a) magnetic potential of the synthetic model show in b; b) Cross section at y= 1500 m of the synthetic model with 2 sources: the shallow source is a 100 m^3 block with a 1 A/m magnetization; the deepest source is a cubic prism of 500 m^3 with a 0.25 A/m magnetization. We assumed a vertical direction for both the inducing field and the magnetization vector.*

The 3D source domain was discretized as 30x30x20 cubic cells, each sized 100x100x100 m^3. We first estimated the structural index of the sources by the scaling function method (Fedi 2007; Florio et al., 2009). The method is based on the computation of the scaling function τ, a dimensionless quantity, which characterizes

the scaling behavior of a homogeneous field *T* (either the magnetic or the gravity field):

$$\tau(z,\zeta) = \frac{\partial \log T}{\partial \log z} = -N\frac{z-\zeta}{z-z_0} \qquad (4.20)$$

where *N* is the structural index, *z* is the upward continuation height, z_0 is the unknown depth to the source and ζ is a guess about the source depth. Typically the scaling function is computed for the data along the so-called ridges, defined as the lines formed by the maxima of the absolute values of the field at a number of altitudes (see Florio et al., 2009 for further details). *N* may be estimated from τ in a number of ways (Fedi, 2007; Fedi and Florio, 2006). In this paper our technique was based on changing the guessed value of ζ until τ, when plotted vs. 1/z, has approximately a zero slope, so to evaluate –*N* as the intercept value. We choose the profile shown in Fig. 4.6a and analyzed the third-order vertical derivative of the magnetic potential (Fig. 4.6b). By the scaling function method applied to the two ridges *a* and *b,* relative to the shallow and deepest sources, respectively, we obtain *N*=2 (the intercept value, 5, must be in fact decreased by the differentiation order of the used field, *k*=3, see Table 4.1), for the structural index of both sources (Fig. 4.6 c,d) This value characterizes compact sources, like a sphere, in the gravity case and also in the magnetic potential case. Then, in virtue of the invariance rules, we should use as depth-weighting exponent the structural index corresponding to the magnetic case, that is β=3.

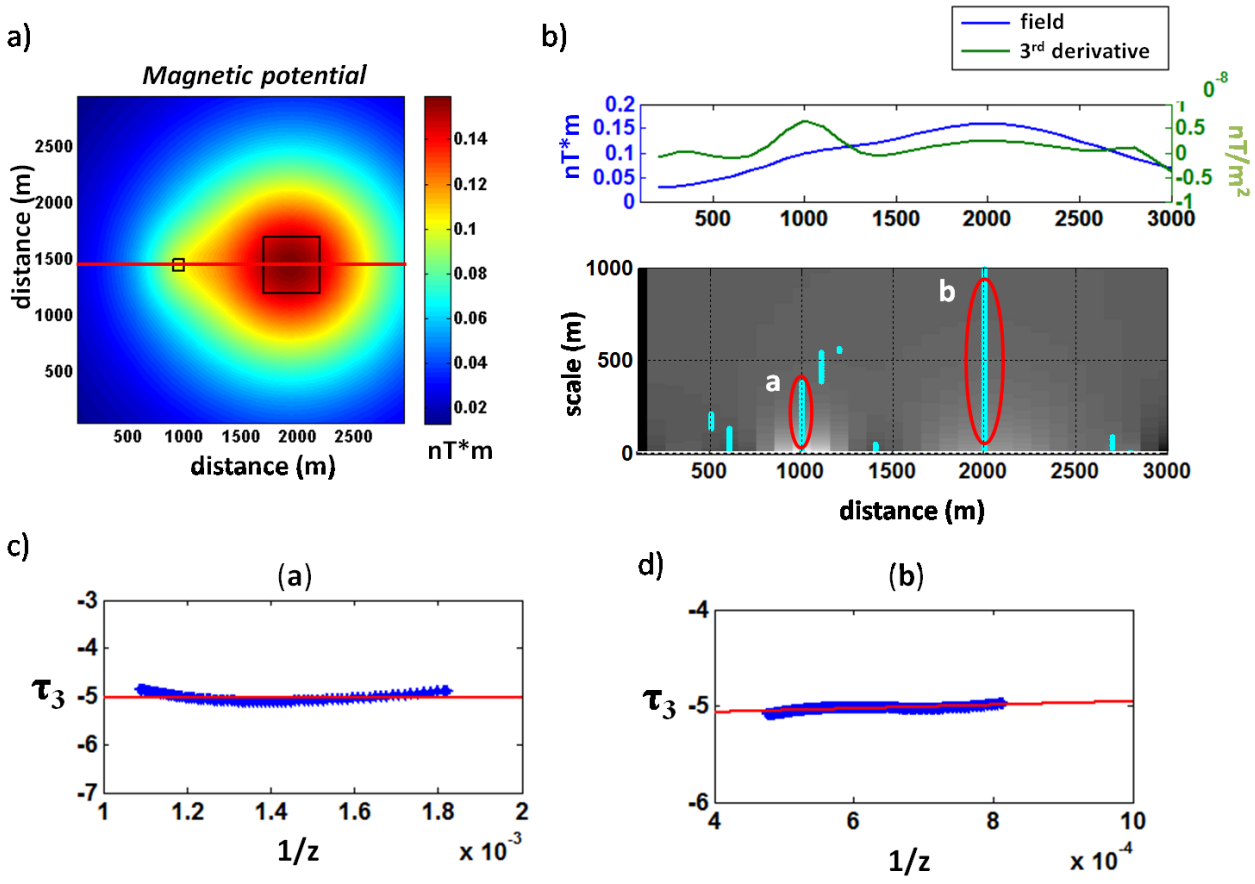

Figure 4.6. *Scaling function analysis: a) magnetic potential of the synthetic model show in Fig. 5 (the red line indicates the analyzed profile); b) ridge selection: we took into account the ridge a for the shallow source and the ridge b for the deepest source; c) scaling function relative to the ridge a; d) scaling function relative to the ridge b. The inducing field and magnetization vectors are vertical.*

We calculated also the magnetic field reduced to the pole and the first and second vertical derivative of the magnetic field generated by the same prismatic sources (Fig. 4.7 b; c; d). It is evident how the interference between the fields due to the two sources decreases with the differentiation order.

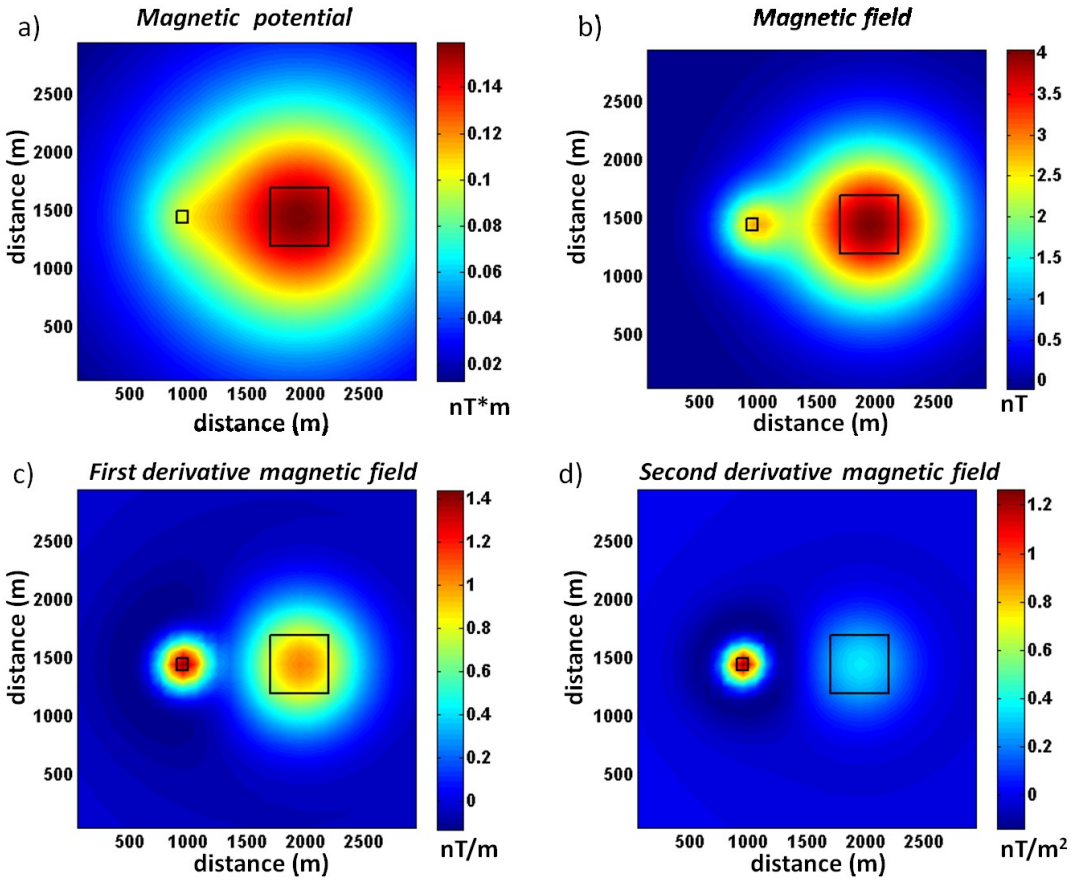

Figure 4.7. *Fields to be inverted: a) magnetic potential; b) magnetic field; c) 1st vertical derivative of the magnetic field; d) 2th vertical derivative of magnetic field. We assumed a vertical direction for both the inducing field and the magnetization vector.*

Following our invariance rules we invert the data by using in all the cases the depth weighting exponent β=3, corresponding to that of the magnetic case. The results (Fig. 4.8) well demonstrate that the found density distribution is invariant with respect to the differentiation order of the field. In all the four cases, a good estimation of the center of both sources is obtained.

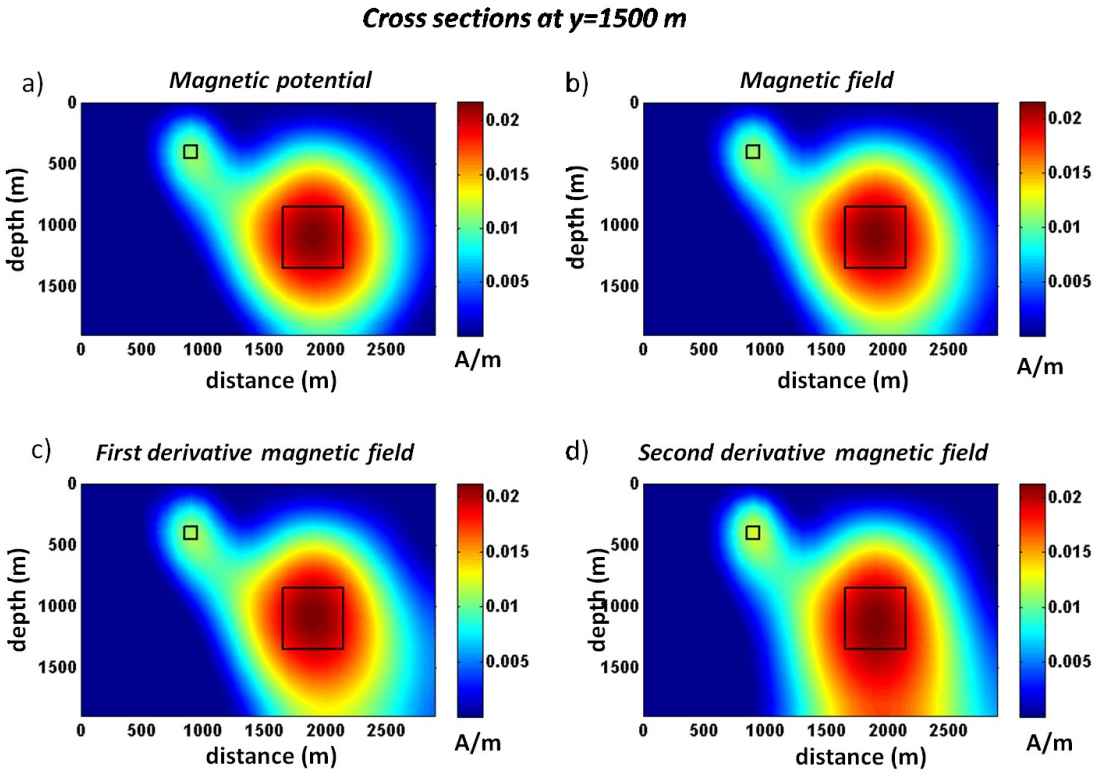

Figure 4.8. *Cross section at y=1500 m of the magnetization model, obtained from inversion of: (a) magnetic potential; (b) magnetic field; (c) 1st vertical derivative of magnetic field; (d) 2st vertical derivative of magnetic field. All the solutions are obtained using β=3 as depth weighting exponent.*

4.8 Real case: Noranda, Quebec

In this section we apply the invariance rules to the inversion of real gravity data measured near Noranda, Quebec (Grant and West, 1965; Fig. 4.9).

The anomaly pattern is associated with a massive body of base metal sulfide (mainly pyrite), which has displaced volcanic rocks of middle Precambrian age (Grant and West, 1965). Grant and West (1965), estimated a depth of about 50 m for the center of this massive body based on the rather unusual formula: $z=0.6x_{1/2}$ (where $x_{1/2}$ is the "half-width" of a profile normal to the strike direction, passing through the abscissa of the anomaly maximum). The formula was indeed assumed for a source

which is too elongated to be approximated by a sphere and too short to be approximated by an infinite cylinder (Grant and West, 1965).

The dataset consists of a regular grid of 47 x 41 data in *x* and *y* direction respectively, 15 m spaced, carefully digitized from Fig. 10.1 in Grant and West (1965).

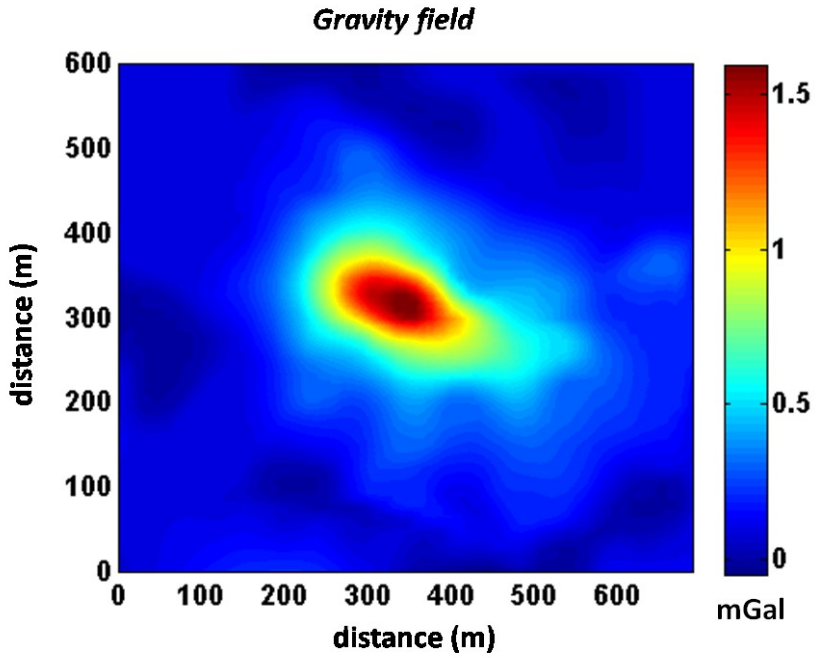

Figure 4.9. *Bouguer anomaly field of a mine in Noranda, Quebec*

Also in this case a necessary preliminary step to the data inversion is the estimation of the source structural index. To this aim we used, as in the previously discussed synthetic examples, the scaling function method (Fedi 2007; Florio et al., 2009). We selected the profile shown in Fig. 4.10a and analyzed the third order vertical derivative of the field. We perform the analysis on the data selected along ridge *a* in Fig. 4.10b. By the scaling function method (Fig. 4.10c) we obtain β=1.4 for the structural index of the source (the intercept value, 4.4, must be decreased by the differentiation order of the used field, 3, see Table 4.1). We estimated this value from gravity data, but by the gravity invariance rules (equation 4.9) we should

instead use, as depth weighting exponent, the structural index corresponding to the vertical derivative of gravity, namely β=1.4+1=2.4.

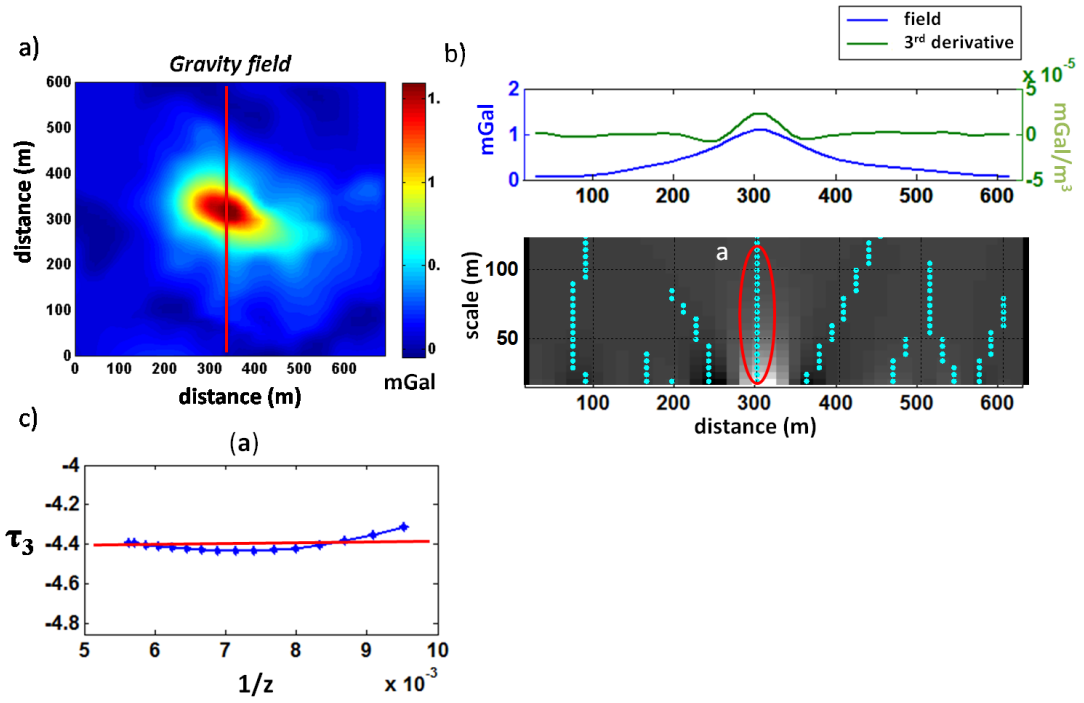

Figure 4.10. *Scaling function analysis: a) gravity field (red line is the chosen profile); b) analyzed ridge; c) scaling function relative to the ridge a.*

We discretized the source domain with 47 x 41 x 20 cells of 15 m in the *x* and *y* direction and 8 m in the *z* direction. The source domain included an external padding consisting of two cells. We inverted the data using both 1.4 (estimated structural index for gravity) and 2.4 (corresponding structural index after gravity invariance rule, equation 4.10) and estimated the regularization parameter μ by GCV method.

In Fig. 4.11 we show two cross-sections (at *y*=330 m and *x*=360 m) of the density model obtained using β =2.4. As expected, we obtained a good solution, also in agreement with the depth estimated by Grant and West (1965), the source being at a depth of about 50 m.

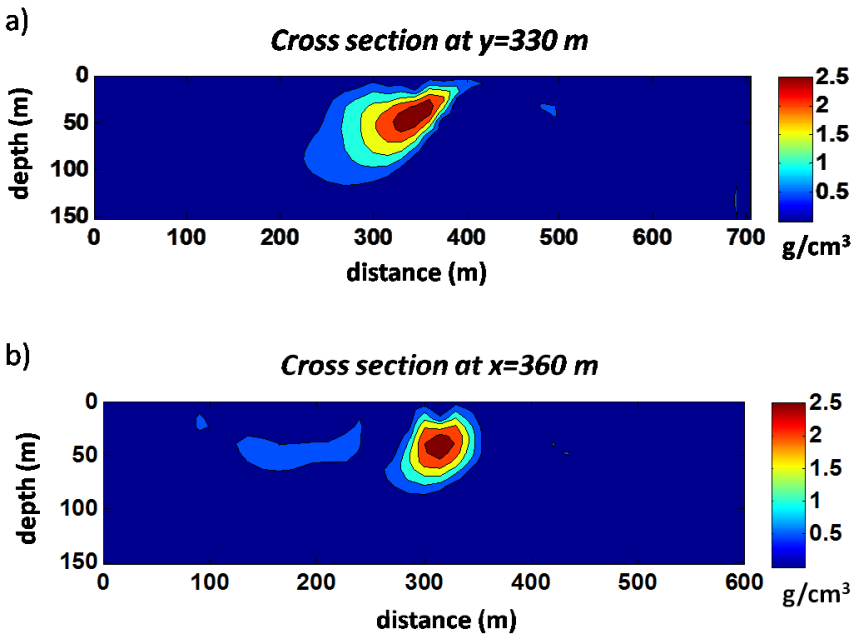

Figure 4.11. *Cross section at y=330 m (a) and at x=360 m (b) of the density model, obtained from inversion of the gravity field (Fig. 4.9), using 2.4 as depth weighting exponent.*

Using instead β =1.4 (Fig. 4.12) as depth weighting exponent, the solution results much shallower, the average depth being about 25 m.

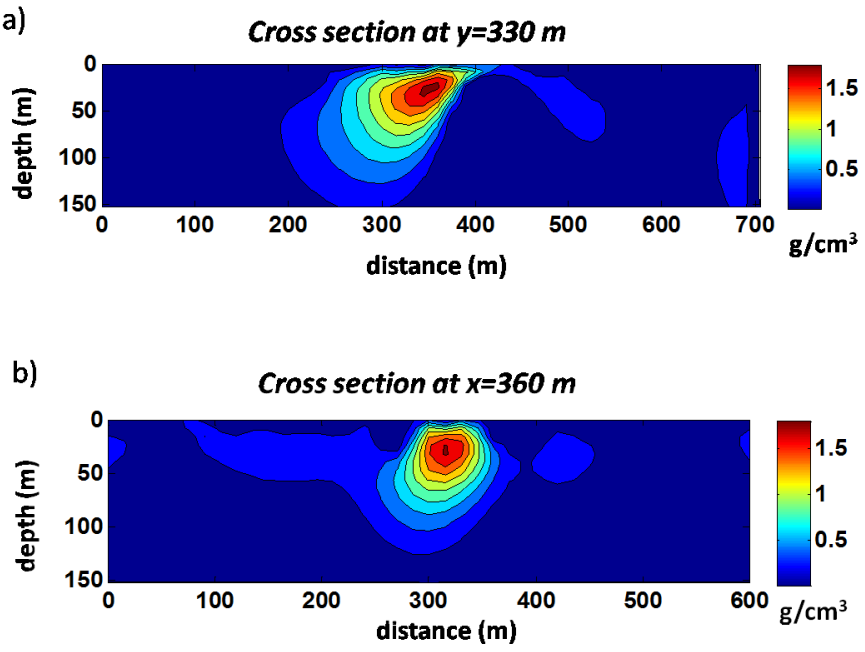

Figure 4.12. *Cross section at y=330m (a) and at x=360m (b) of the density model, obtained from inversion of the gravity field (Fig. 4.9), using 1.4 as depth weighting exponent.*

Finally, we now show that the density model is invariant by using any *k*-order derivative of gravity. To this end, we inverted also the first and the second order vertical derivatives of the field. In Fig. 4.13 it is evident the improvement in resolution obtained through the differentiation process of the data. The second vertical derivative map was slightly low-pass filtered prior to be inverted to avoid an excessive noise amplification. According to our invariance rules, the several fields were each one inverted by using the same value for the exponent of the depth-weighting function, that is β=2.4.

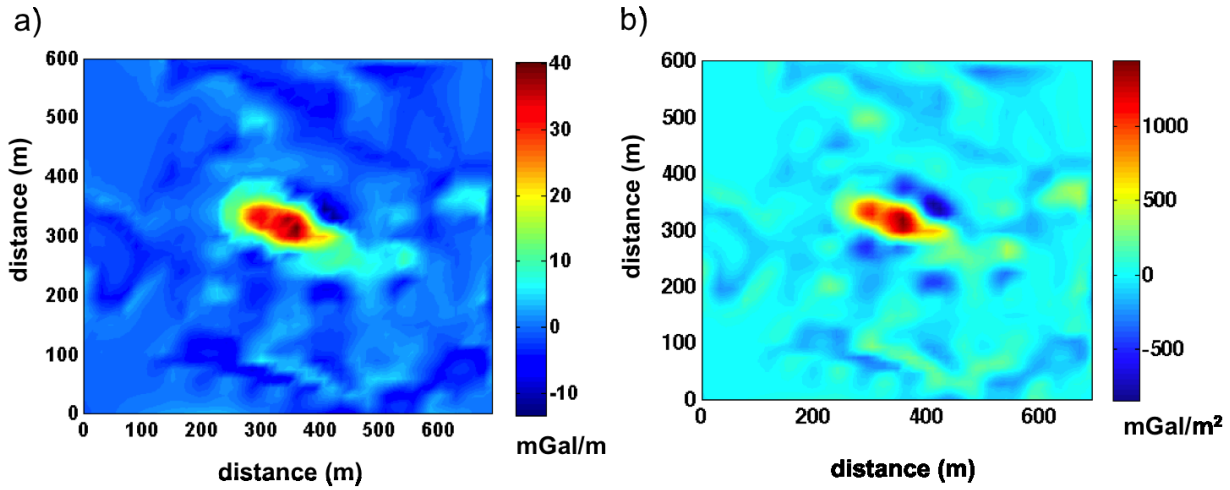

Figure 4.13. *First (a) and second (b) vertical derivative of the gravity anomaly shown in Fig. 4.9*

The model domain was discretized with the same parameters as those used for the inversion of the field. The regularization parameter was computed for each case by the GCV method.

In Fig. 14 and 15 we show the solutions obtained for the first order derivative and for the second order derivatives of the field, respectively.

The comparison of the respective density models (Fig. 4.14 and 4.15) with the density distribution obtained inverting the field (Fig. 4.11) demonstrates that the solution is very similar in all three cases: there is no improvement of resolution in

the models, although the data do have very different resolutions. Small differences in the model obtained by the second vertical derivative (Fig. 4.15), with respect to the models obtained from other fields, are probably due to the low-pass filtering of this second vertical derivative field.

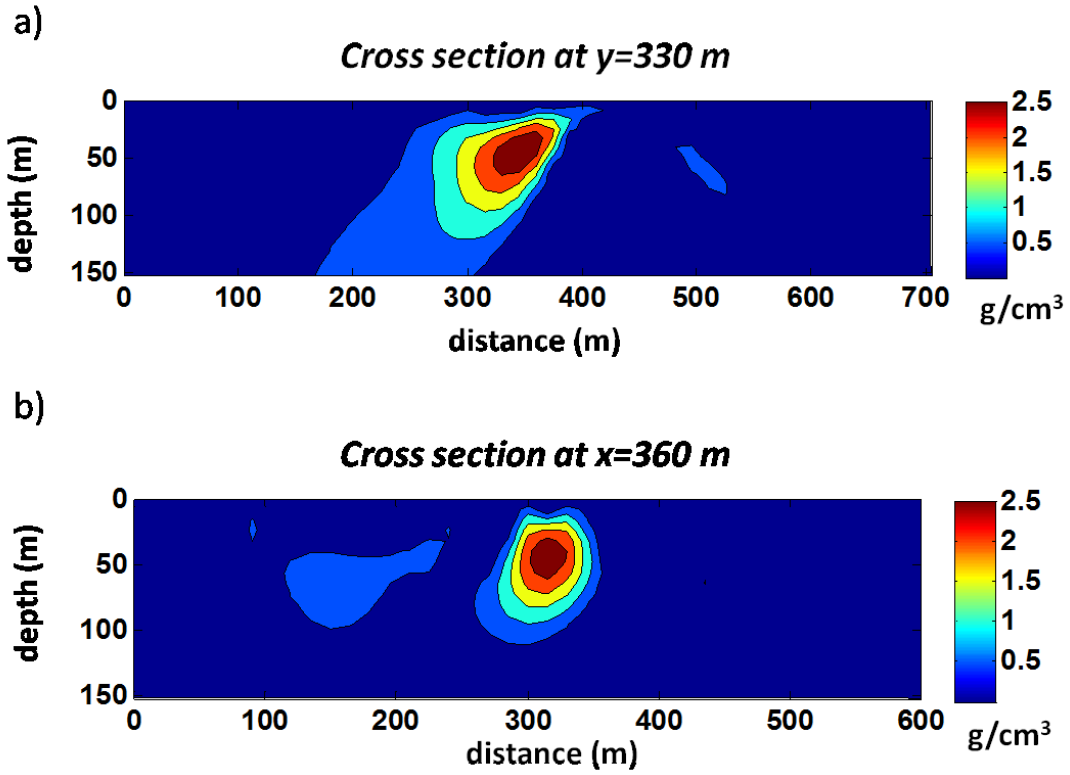

Figure 4.14. *Cross section at y=330m (a) and at x=360m (b) of the density model, obtained from inversion of the first vertical derivative of the gravity field (Fig. 4.13 a), using 2.4 as depth weighting exponent.*

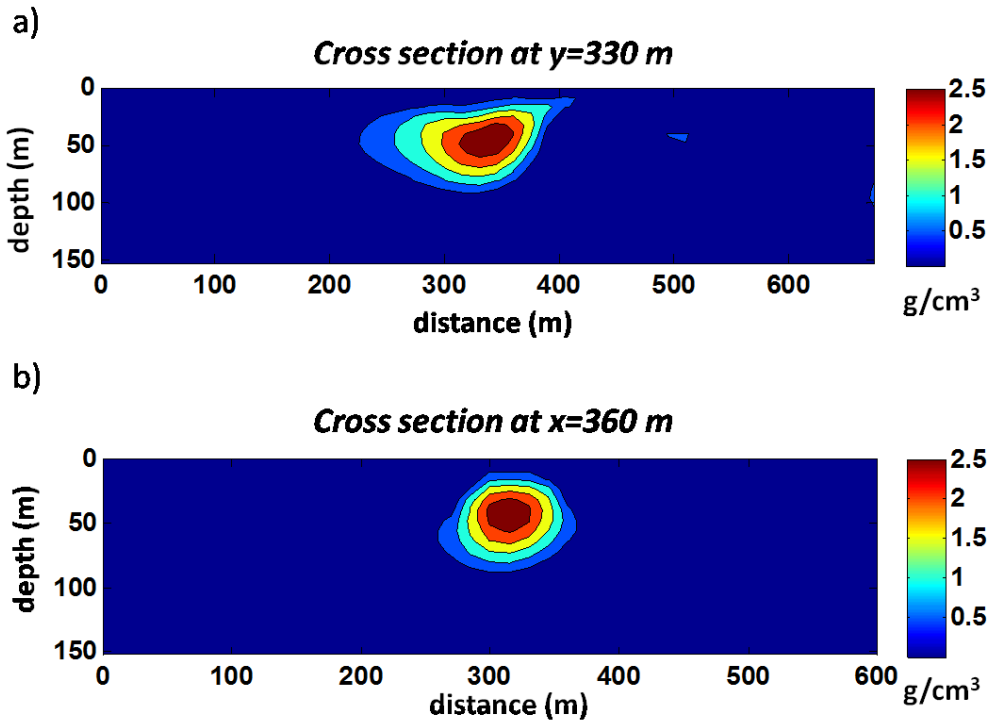

Figure 4.15. *Cross section at y=330m (a) and at x=360m (b) of the density model, obtained from inversion of the second vertical derivative of the gravity field (Fig. 4.13 b), using 2.4 as depth weighting exponent.*

4.9 Improvement of the model resolution

The invariance rules described before ensure that the solution does not change varying the order derivative of the field, and that the improvement in the data resolution does not reflect in any improvement in the model resolution. In this section a new method to increase the resolution of the solution will be described.

Consider the problem:

$$\mathbf{d} = \mathbf{A}\mathbf{m} \qquad (4.21)$$

This equation represents a convolution between the kernel **A** and model parameters **m**.

When we invert a potential field data or any of its n^{th} order derivatives, we use a kernel with the same differentiation order of the data, and the problem in 4.21 becomes (in the case of a n^{th} order vertical differentiation):

$$\frac{\partial^n \mathbf{d}}{\partial z^n} = \frac{\partial^n \mathbf{A}}{\partial z^n}\mathbf{m} \qquad (4.22)$$

The solution of the problem 4.22 is given by:

$$\frac{\partial^n \mathbf{d}}{\partial z^n}\left[\frac{\partial^n \mathbf{A}}{\partial z^n}\right]^{-1} = \mathbf{m} \qquad (4.23)$$

We see that this differentiation process does not affect the model vector **m** that remains the same, for the minimum length solution or the weighted minimum length solution. We have demonstrate this mathematically in Appendix B.

From these considerations we derive our idea: what happens if we invert the data with a different order differentiation with respect to the kernel?

The differentiation of a convolution has the following property:

$$D(f * g) = Df * g = f * Dg \qquad (4.24)$$

where *D* denotes differentiation.

Then we can write eq. 4.22 as:

$$\frac{\partial^n \mathbf{d}}{\partial z^n} = \mathbf{A}\frac{\partial^n \mathbf{m}}{\partial z^n} \qquad (4.25)$$

the solution to problem 4.25 is:

$$\frac{\partial^n \mathbf{d}}{\partial z^n}\mathbf{A}^{-1} = \frac{\partial^n \mathbf{m}}{\partial z^n} \qquad (4.26)$$

or in general form:

$$\frac{\partial^k \mathbf{d}}{\partial z^k}\left[\frac{\partial^n \mathbf{A}}{\partial z^n}\right]^{-1} = \frac{\partial^{(k-n)}\mathbf{m}}{\partial z^{(k-n)}} \qquad (4.27)$$

where *k* and *n* are differentiation orders of data and kernel respectively.

In this case if *k>n* we obtain the *k-n* order vertical derivative of the solution **m**, if *k<n* we obtain the n-k order integration of the solution **m**.

Therefore with this strategy we can obtain solution with different order differentiation and then with different resolution, similarly to what happens with the fields. Furthermore, in this case to obtain a correct estimate of depth we need to choose the exponent β of depth weighting function according to:

$$\beta = N + (k - n) \qquad (4.28)$$

where *N* is the structural index of the source. If *k=n* we return to classic problem described in the previous paragraphs, β depends only on the source type and does not change with order of derivation; if $k \neq n$, β increases if *k>n* or decreases if *k<n*, according to equation 4.24.

To demonstrate this we perform three inversions of three datasets with different differentiation orders: magnetic field (Fig 4.16a), first vertical derivative of magnetic field (Fig 4.16b), and second vertical derivative of magnetic field (Fig 4.16c). We use for each of the three cases the same kernel calculated for the magnetic case and use as depth weighting exponent β the values 3, 4 and 5 respectively, according to equation 4.24. As mentioned above, it is evident the improvement in resolution in the fields increasing the order of derivation.

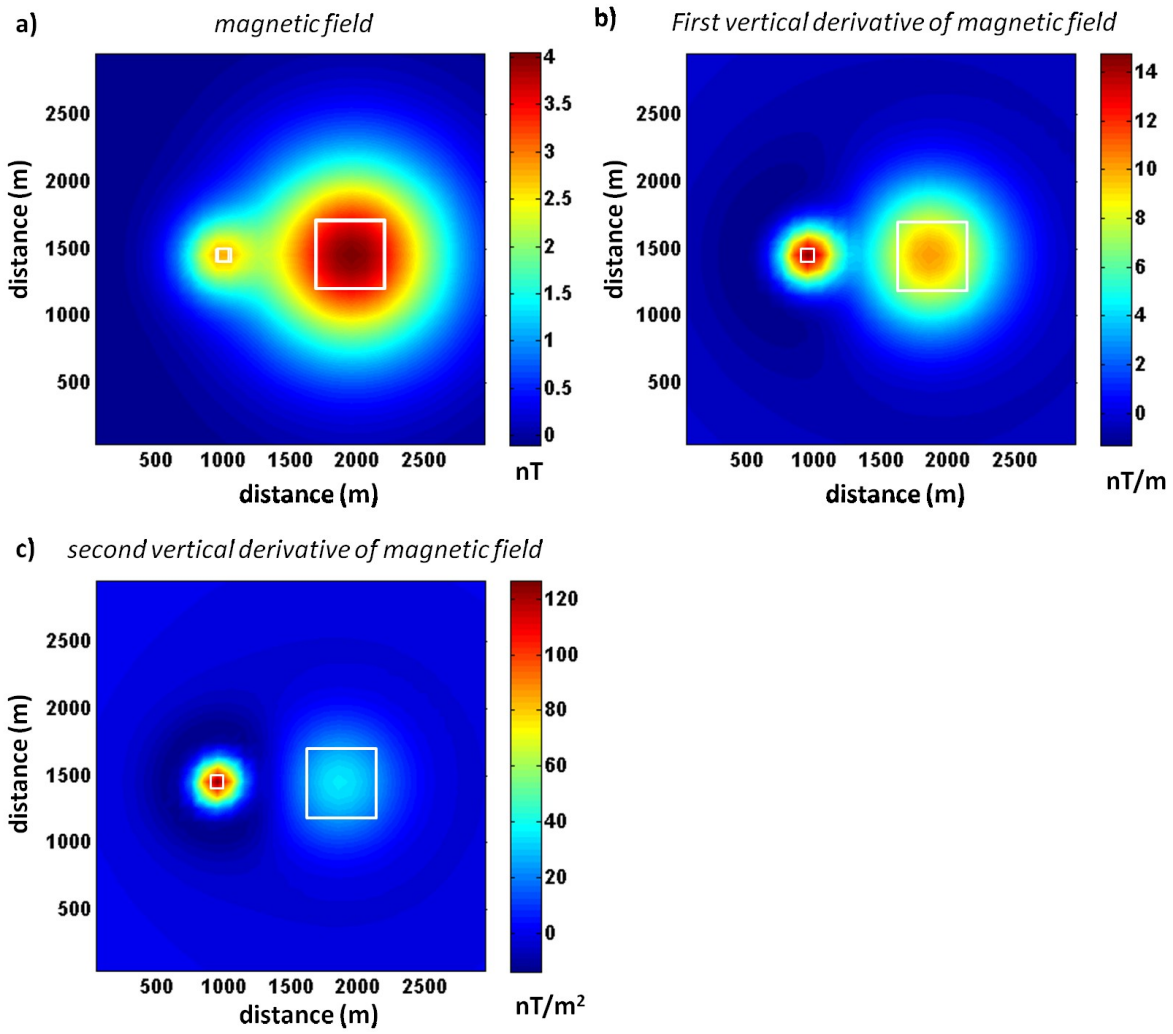

Figure 4.16. *a) magnetic* field; c) 1st vertical derivative of the magnetic field; d) 2th vertical derivative of magnetic field. The inducing field and the magnetization vector are vertical.

When we use this inversion strategy is not possible to use positivity constrains, because the derivative fields contain negative values that the kernel cannot generate, and therefore the model must contain negative values to fit the data. The inverted models (Fig. 4.17) demonstrate that in this case increasing the order of derivation increases also the resolution of model, meaning that the interference between the two sources decreases with the differentiation order.

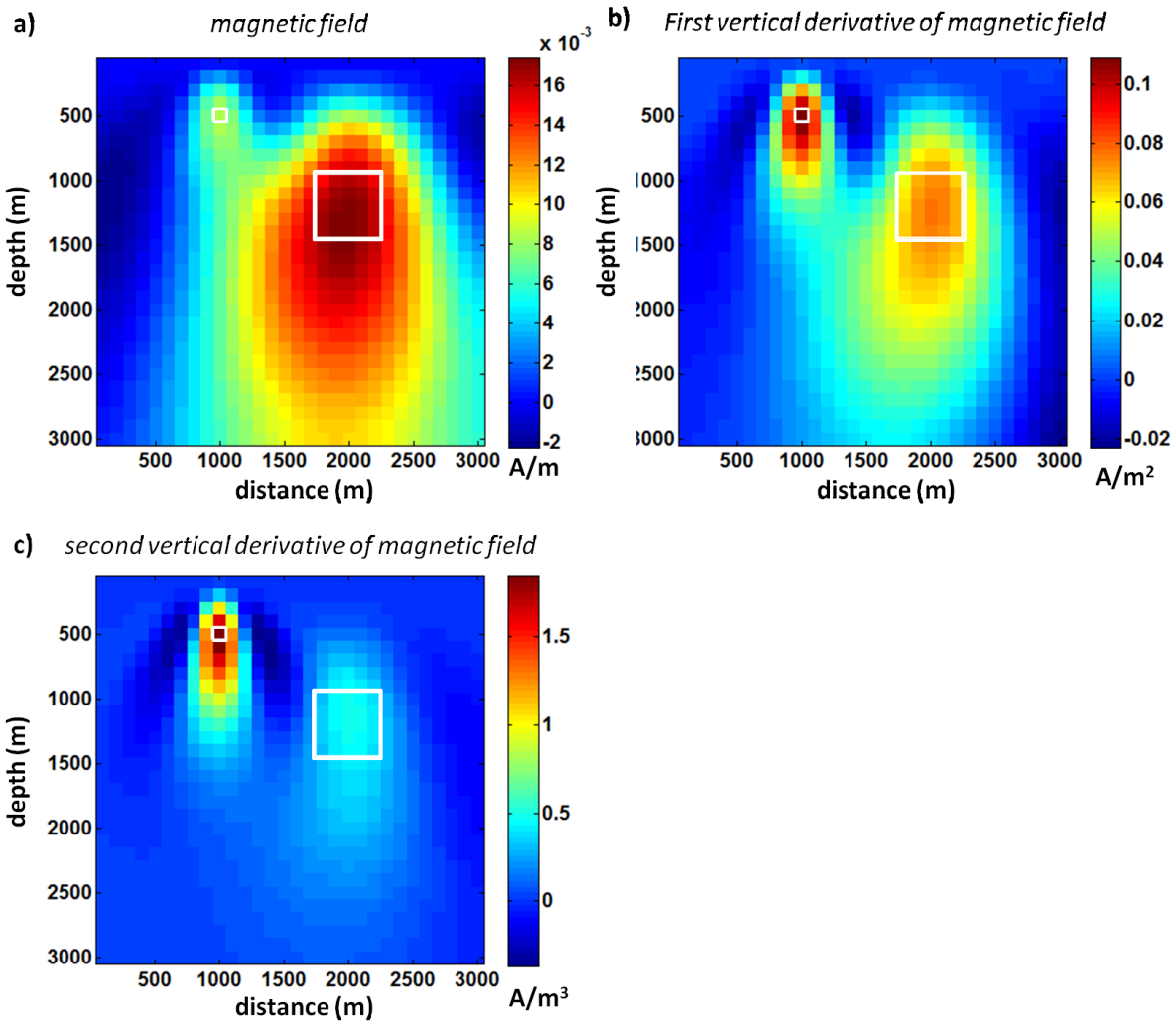

Figure 4.17. *Solutions obtained using the magnetic kernel and a)magnetic field; b) first vertical derivative of magnetic field; d) second vertical derivative of magnetic field. All fields are shown in Fig. 4.16.*

CHAPTER V

Inhomogeneous depth weighting

5.1 Introduction

Cella and Fedi (2012) showed that to obtain a correct estimate of depth to source in the inversion of undetermined problems it is necessary to use a depth weighting function as proposed by Li and Oldenburg (1996, 1998) with an exponent β equal to the correct structural index (*N*) of the source. In Chapter 4 we introduced some invariance rules, according to which we should always use the structural index related to the magnetic case, no matter the field type actually inverted.

In this Chapter the case of a field generated by sources with different structural index will be analyzed. This is a very important case, because it is the most common situation in real data. In this case, there isn't a unique value for β allowing us to obtain a correct depth estimation for all sources. In Fig. 5.1 a simple two source gravity synthetic field is shown. The two sources are a small compact source, that can be approximated by a sphere (*N*=2), at x= 100m y=200m and z=40m, with density of 2 g/cm^3 and a vertical dyke (*N*=0) centered at x=300m y=200m and z=40m (top of dyke) with density of 0.4 g/cm^3. The 3D source domain was discretized as 40x40x30 cubic cells, each sized 10x10x10 m^3. We do not use a reference model and set the following values for the α parameters: α_s*=0.0001* α_x=1*,* α_y=1*,* α_z=1.

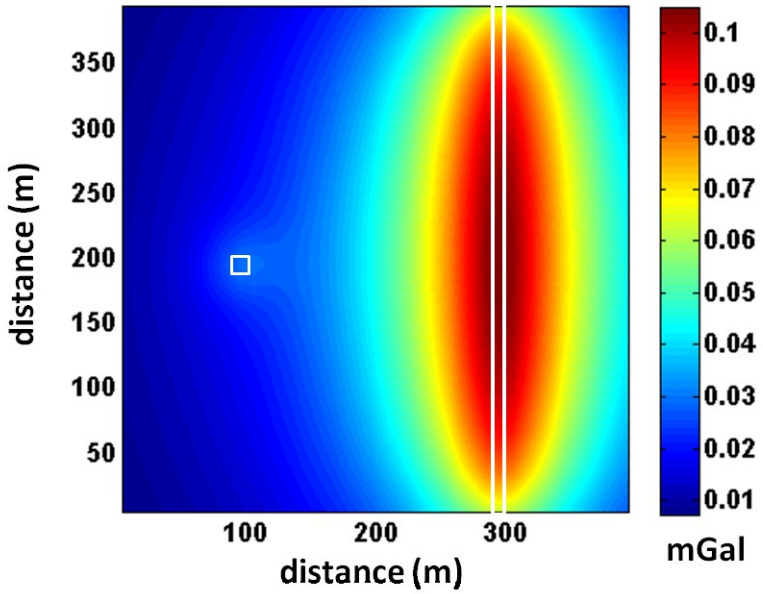

Figure 5.1. G*ravity field generate by a compact source at x=100m, y=200m, z=400m, with density of 2 g/cm^3 and a dyke centered at x=300m, y=200m and z=40m (top), with density of 0.4g/cm^3*

According to the invariance rules described in Chapter 4, the correct value to use as depth weighting exponent β is 3 for the compact source and 1 for the dyke. In Fig. 5.2a we show the solution obtained using β=3 (Fig. 5.2 a) and β=1 (Fig. 5.2b). Using β=3 we correctly estimate the center of sphere, but the depth to top of the dyke is about 80 m and the results overestimated. Vice versa, using β=1 a correct estimate of the depth to the top of the dyke is obtained, but the depth to the center of the sphere is about 20 m and the results underestimated.

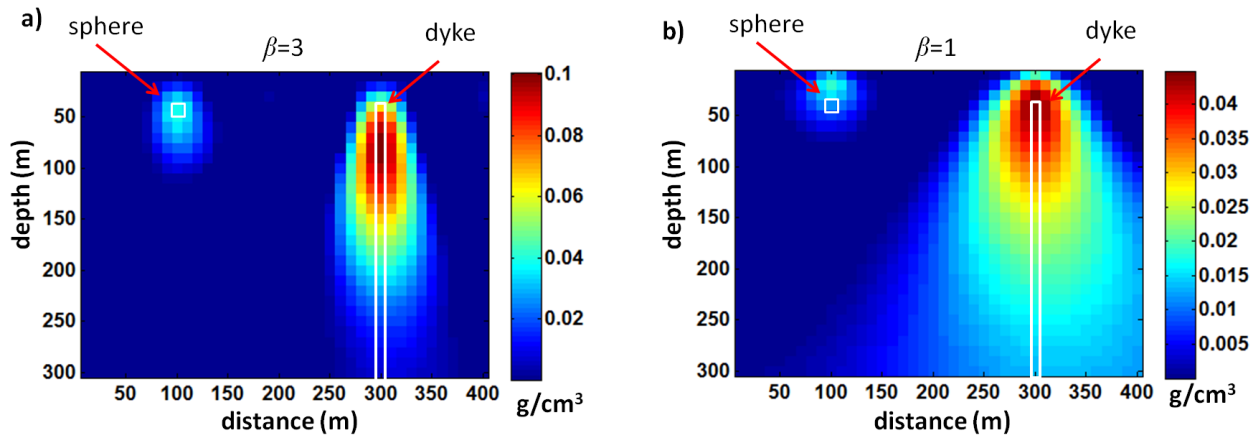

Figure 5.2. *Solutions obtained by inverting the field in Fig. 5.1 using a) β=3 and b) β=1.*

To solve this problem four different approaches are illustrated in the following Sections:

a) use of an average value of β (=*N*);
b) perform distinct inversions using different depth weighting functions, one for each source with different *N;*
c) use of an inhomogeneous depth weighting function that incorporates different values of *N;*
d) use of constraints.

5.2.1 Use of an average value for β (=N)

If the difference of the structural indices is not very big, we can assign to β the average value of the estimated structural indices, N_{AVE}. To show the performance of this first approach we consider the synthetic gravity field generated by two sources (Fig. 5.3a), a small compact source that can be approximated to a sphere (*N*=2) at x= 100m y=200m and z=40m, with density of 2 g/cm^3, and a horizontal cylinder (*N*=1) centered at x=300m y=200m and z=40m with density of 0.4 g/cm^3. The anomaly is

inverted by using the average value N_{AVE} (=1.5 and then, because of the invariance rules, β=2.5). By this approach the depth to sources are about 40m for the center of both sphere and cylinder, then the depth is correctly estimated for both sources simultaneously (Fig. 5.3b).

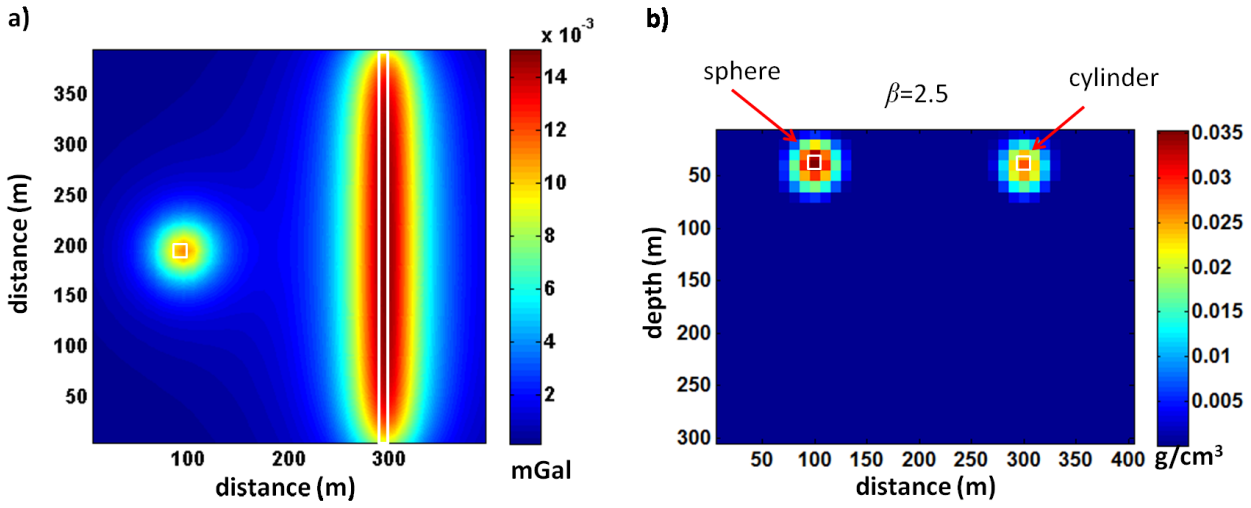

Figure 5.3. *a) Gravity field generated by a small compact source at x=100m, y=200m, z=400m, with density of 2 g/cm^3 and a horizontal cylinder at x=300m, y=200m and z=40m (top), with density of 0.4g/cm^3; b) solutions obtained by inverting the field in fig5.3a using β=2.5.*

5.2.2 Perform distinct inversions using different depth weighting functions

If the difference of structural indices is greater than previous example, to limit the errors it is more convenient to perform distinct inversions using different values for the depth weighting exponents and during the interpretation phase to consider as a valid solution only the portion of the model inverted with an exponent value consistent with the local structural index. In fig. 5.4 we consider the same case shown in Fig. 5.1 with a sphere-like source and a dyke.

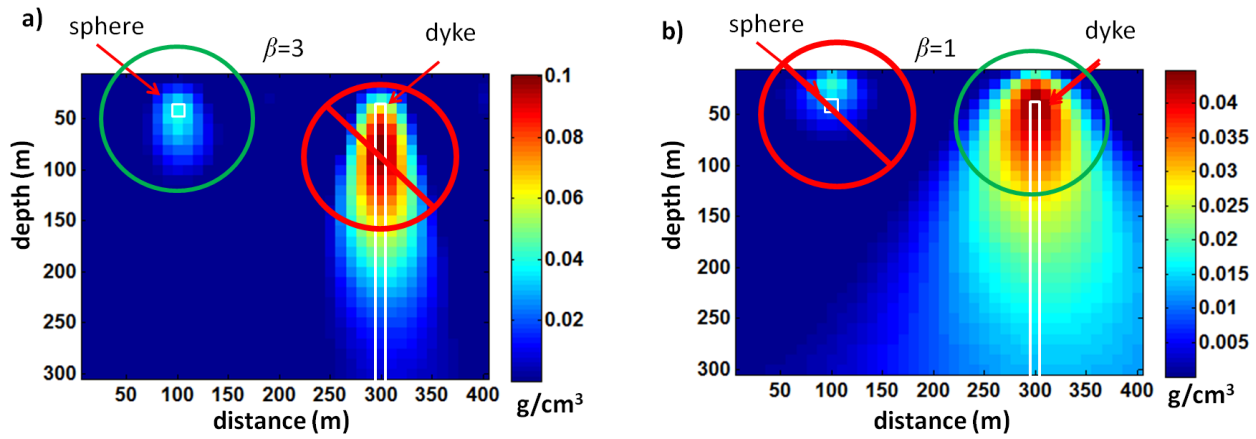

Figure 5.4. *Solutions obtained by inverting the field in Fig. 5.1 using a) β=3 and b) β=1. Only the portion of the model for which the value of β is consistent with the source structural index should be considered (green circle), while the density distribution highlighted by the red circle should be discarded.*

5.2.3 Use of an inhomogeneous depth weighting function that incorporates different values of N

The depth weighting introduced by Li and Oldenburg (1996, 1998), allow us to use a single value of exponent β, constant in the source volume. We can also set up an inhomogeneous depth weighting function, in which we can introduce different values of β in different portion of model:

$$w(x,y,z) = \frac{1}{z^{\beta(x,y,z)/2}} \qquad (5.1)$$

Consider again the synthetic gravity field generated by a sphere and dyke (Fig. 5.1). In this case we can build a depth weighting function with an exponent β that changes from 3 to 1 within the model.

A slice of a 3D inhomogeneous depth weighting function, normalized with respect to its maximum value is shown in Fig. 5.5a. The inversion results using this depth weighting function are shown in Fig. 5.5b. The followed coefficients were used:

α_s=*0.0001* α_x=1, α_y=1, α_z=1. In this case the depth is correctly estimated for both sources (center for the sphere and top for the dyke). However, along the boundary between the two domains (β=3 and β=1), an erroneous concentration of density is present.

This error can be considerably reduced if we change the values of the α coefficients. In Fig. 5.5c the solution obtained by using α_s=*0.0001,* α_x=100, α_y=100, α_z=100 is shown. The 'ghost' at the boundary between the two domains is now minimized, having very low density. Increasing the horizontal and vertical derivative coefficients (α_x, α_y, α_z) reinforces the minimization of gradients of the solution along the three spatial directions and then the solution will be smoother.

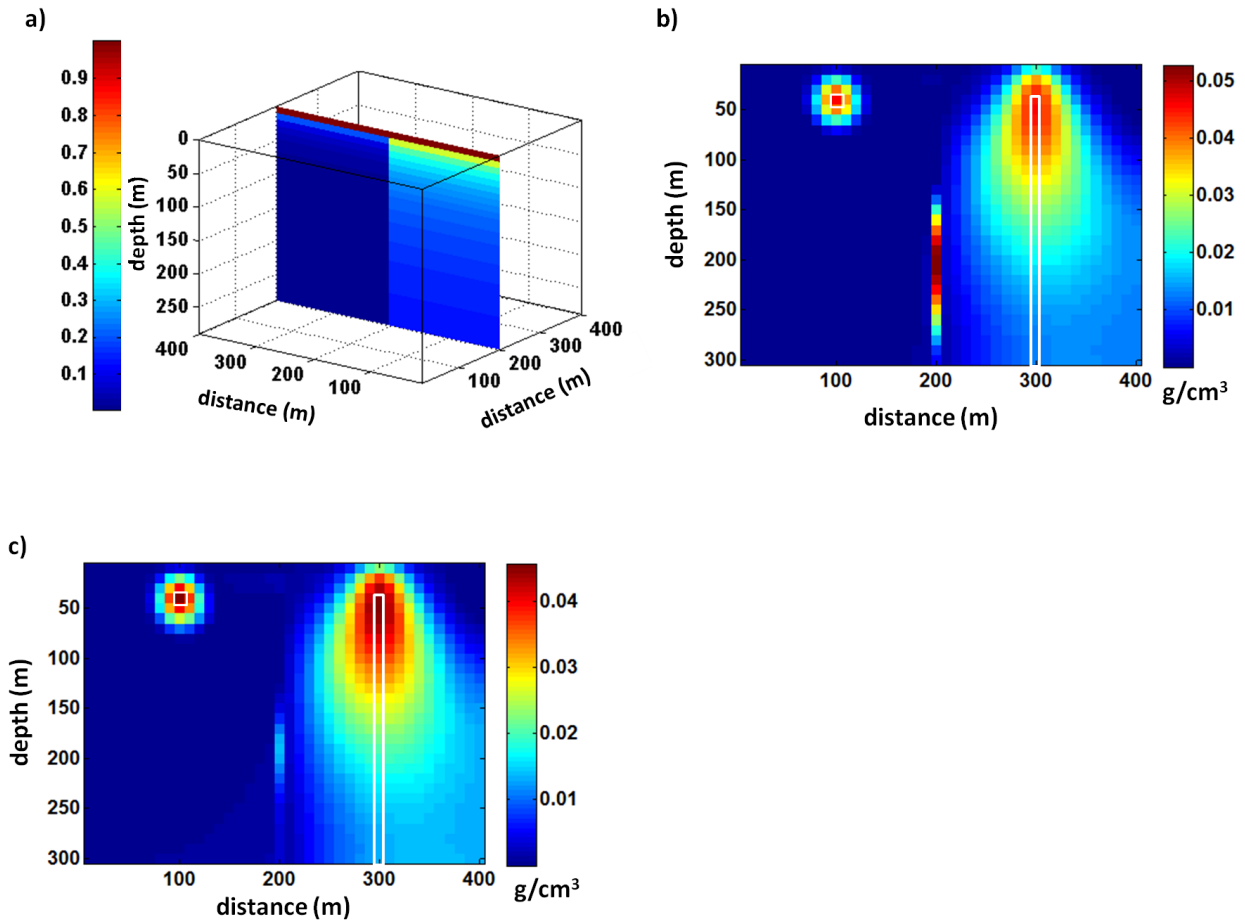

Figure 5.5. *a) Vertical slice of 3D inhomogeneous depth weighting function normalized with respect to its maximum value; b) vertical section at y=200m of the model inverted using the inhomogeneous depth weighting function (a) and α_s=0.0001 α_x=1, α_y=1, α_z=1; c) vertical section at y=200m of the model inverted using the inhomogeneous depth weighting function (a) and α_s=0.0001 α_x=100, α_y=100, α_z=100.*

There may be cases in which this approach does not work very well, for example when the sources are too close to each other. In Fig. 5.6 we show the gravity field generated by the same sources of the previous example, but now at x=120m, y=200m, z=40m (sphere) and at x=280m, y=200m, z=40m (dyke). The model obtained using inhomogeneous depth weighting and α_s=0.0001 α_x=100, α_y=100, α_z=100, is shown in Fig. 5.7b, and still presents an erroneous strong density feature at the boundary between the domains characterized by different values of β.

It is possible to reduce this error by building an inhomogeneous depth weighting function with a smooth variation between β=3 and β=1. An example of this depth weighting function and of the model obtained by using it, is shown in Fig. 5.7c and d, respectively. Comparison of results in Fig. 5.7d and b demonstrates the improvement achieved.

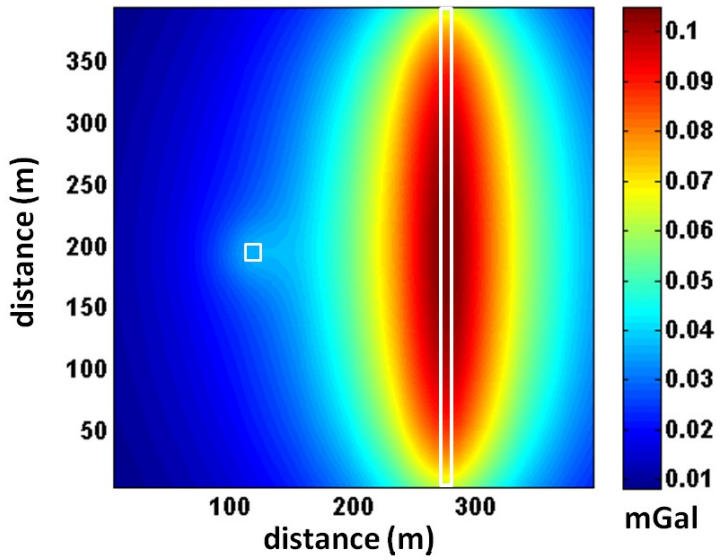

Figure 5.6. *Gravity field generated by a compact source at x=120m, y=200m, z=400m, with density of 2 g/cm^3 and a dyke centered at x=280m, y=200m and z=400m (top), with density of 0.4g/cm^3*

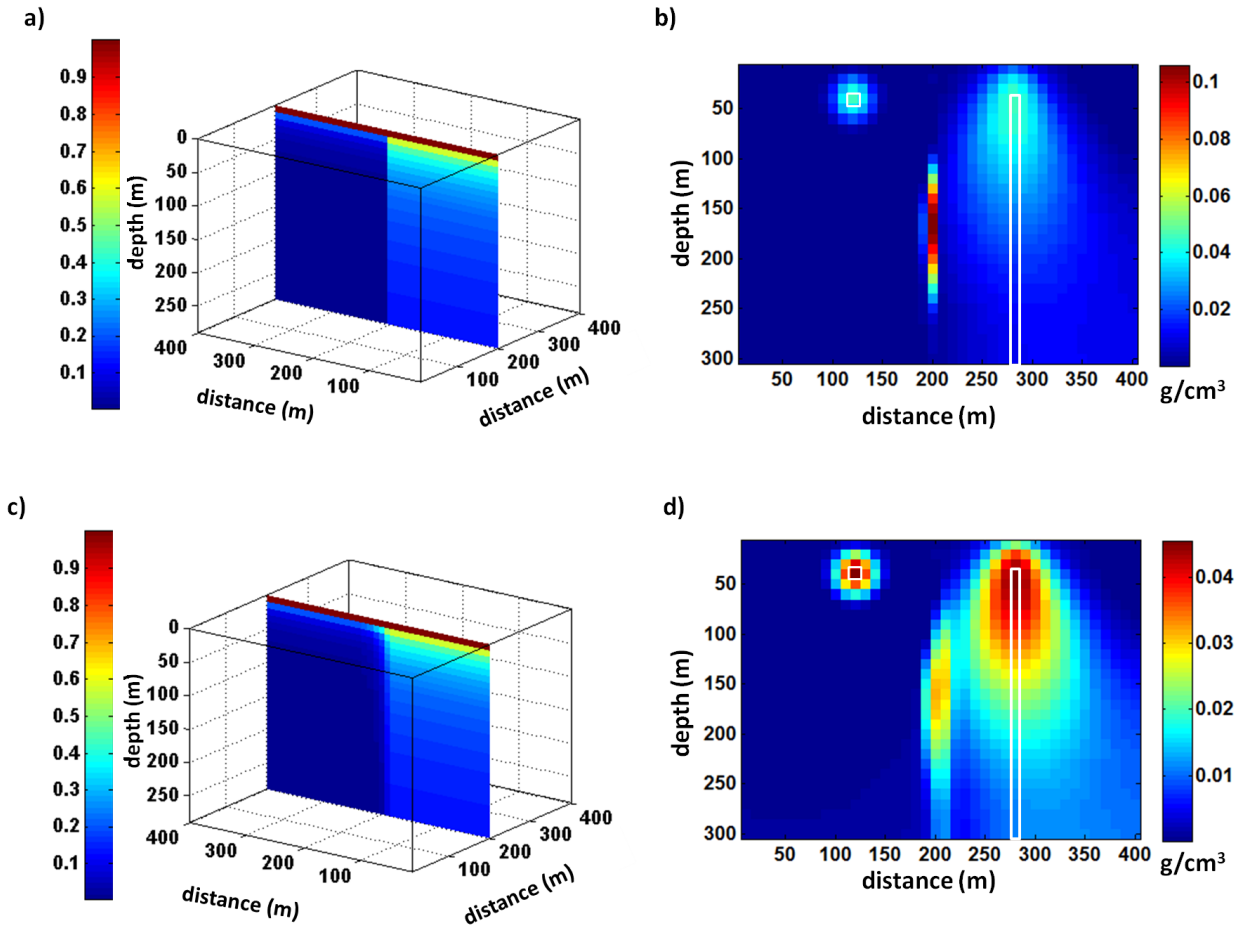

Figure 5.7. *a) Vertical slice of 3D inhomogeneous depth weighting function normalized with respect to its maximum value; b) vertical section at y=200m of the model inverted using the inhomogeneous depth weighting function in a), obtained using* α_s=0.0001 α_x=100, α_y=100, α_z=100; *c) vertical slice of 3D inhomogeneous depth weighting function with smooth variation; d) vertical section at y=200m of model inverted using inhomogeneous depth weighting function in c), obtained using* α_s=0.0001 α_x=100, α_y=100, α_z=100;

5.2.4 Use of constraints

Another approach to correctly deal with a gravity or magnetic field characterized by a source distribution causing a spatially variable structural index consists in introducing constraints of different types (reference model, upper and lower density

boundary, focusing and other) to reduce the dependency of solution on the depth weighting function.
In the next two chapters a detailed analysis about this point will be developed.

5.3 Real case: Vredefort Dome (South Africa)

5.3.1 Geology and geophysics

The Vredefort structure is located within the Witwatersrand basin, South Africa.
Boon & Albritton (1937) were the first to suggest an impact origin. In the early 1960s, Dietz (1961) and Hargraves (1961) cited the occurrence of shatter cones at Vredefort as evidence of an impact origin. After nearly a century of debate, the ca. 80-km wide Vredefort Dome is now widely accepted as the central uplift of a much larger impact structure (Gibson and Reimold, 2001).
Kamo et al. (1996) dated the impact event at 2.023±0.004 Ga based on the estimated age of pseudotachylite in the core region.
The original diameter of this impact structure was in excess of 250 km (Reimold and Gibson, 1996; Gibson and Reimold, 2000, 2001) and the Vredefort crater is one of the largest and oldest impact structures on Earth.

Reimold and Gibson (1996) reported a synthesis of the geologic knowledge about the Vredefort dome. Following these authors, the near circular Vredefort Dome, 70 km in diameter, located about 120 km to the southwest of Johannesburg, consists of Archaean granitoids in a 40-km-wide central core and of metasediments and metavolcanics in an outer collar belonging to the 2.9-2.72 Ga Witwatersrand, the ca. 2.7 Ga Ventersdorp, and 2.5-2.25 Ga Transvaal Supergroups (Fig. 5.8). Locally, along

the outer margin of the Witwatersrand Basin, felsic metasediments occur and mafic metavolcanics of the 3.074 Ga Dominion Group and 3.1-2.8 Ga basement granitoids. The crystalline core of the dome consists of an outer annulus of heterogeneous amphibolite-facies migmatites of the Outer Granite Gneiss (OGG) around the central Inlandsee Leucogranofels (ILG). The southeastern part of the Vredefort Dome is covered by Karoo (250-180 Ma) sediments and dolerites (Reimold and Gibson, 1996).

In 1990, McCarthy et al. mapped the presence of series of anticlines and synclines from the center to a radial distance of 150 km, arranged as concentric rings and clearly related to the formation of the Vredefort impact structure.

Dikes of the so-called Vredefort granophyre occur both in the central core and distal collar areas. In the core area, the dikes are radial with respect to the structure and are up to 20 m wide and 4–5 km long. In the collar, the dikes are concentric with respect to the structure and can be >50 m wide and about10 km long (Grieve and Therriault, 2000).

An integrated geophysical model of the Vredefort structure, based on refraction and reflection seismic, gravity, magnetic, and petrophysical data, was published by Henkel and Reimold (1996, 1998). This model demonstrated that the central uplift of this large impact structure, the Vredefort Dome, is deeply eroded, about 80 km wide, and still represents a structural uplift of about 12 km, at the present erosion level. This structural uplift is best illustrated by the rise of the lower parts of the upper crust (layers 3 and 4, Fig. 5.9).

The total uplift may originally have amounted to as much as 20 km (Henkel and Reimold, 1998).

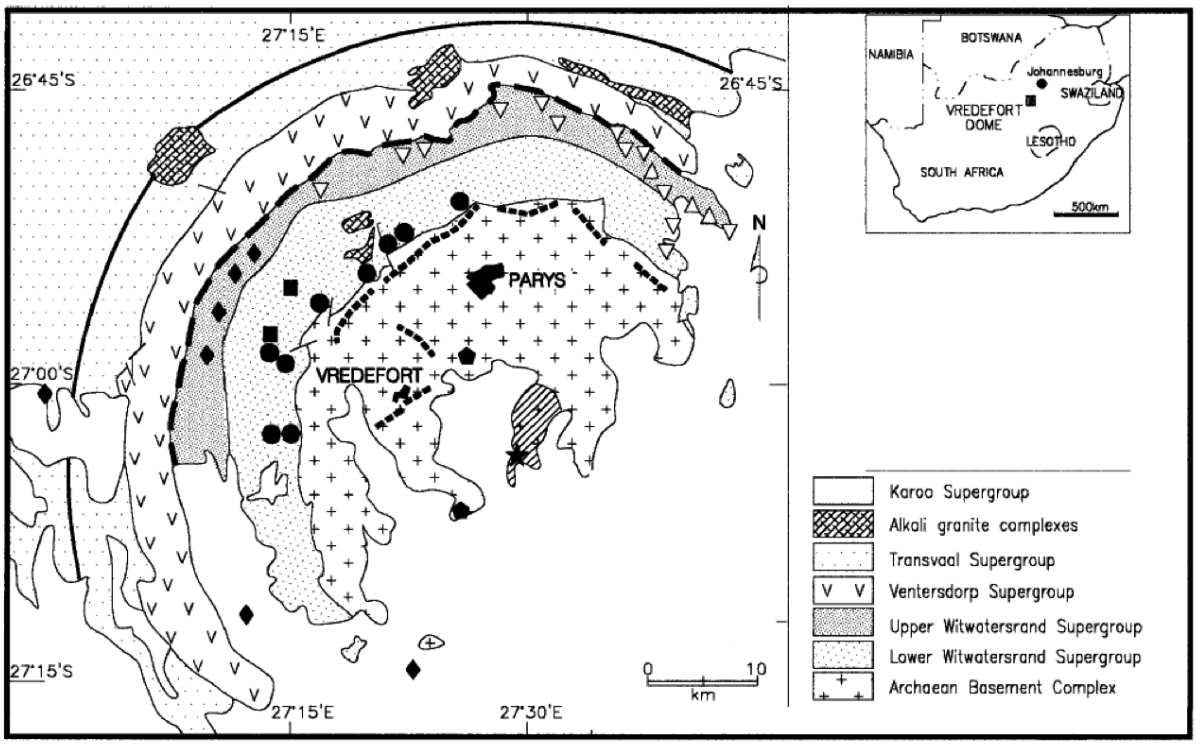

Figure 5.8. *Geological map of Vredefort Dome Area* (from Gibson, et al 2002)

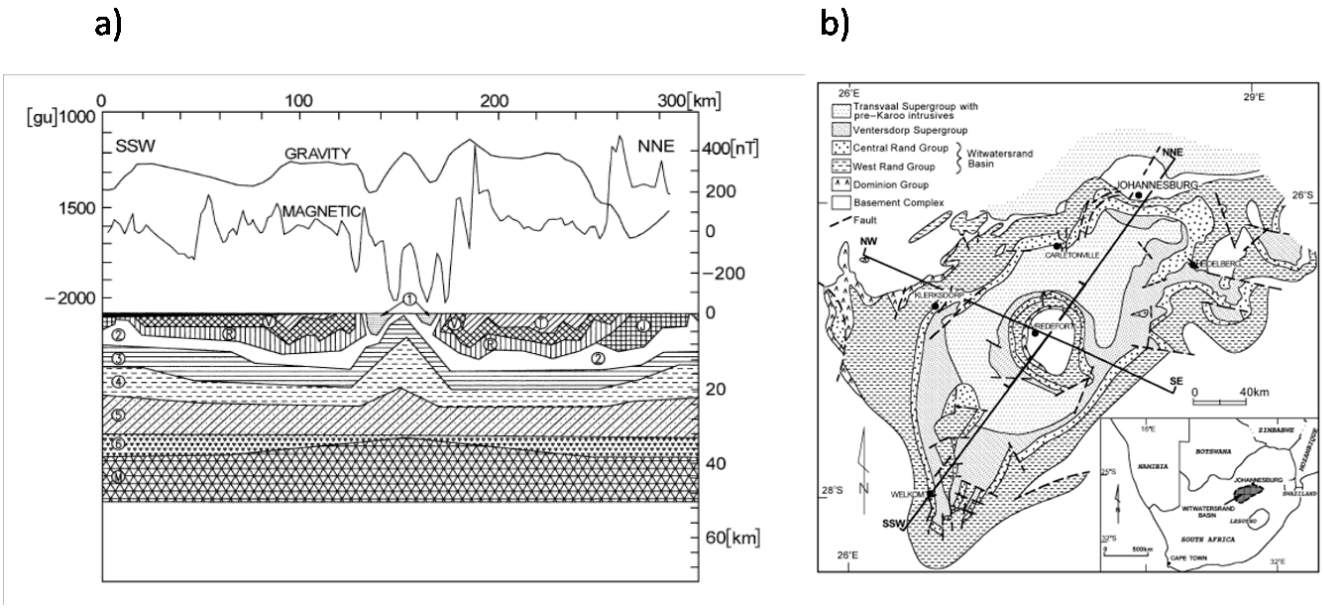

Figure 5.9. *a) Gravity model of the SSW–NNE section (see Figure 5.9 b) through the Vredefort impact structure* (Henkel and Reimold, 1996, 1998).

Hart et al. (1995) analyze the magnetic anomaly of the Vredefort area and claim that the data in the Vredefort basement are consistent with impact-related thermal remanent magnetization.

The aeromagnetic data over the structure (Corner et al., 1990) show strong, well-defined concentric patterns (Fig. 5.10). In the outer rim, the pattern reflect the different sedimentary strata. About halfway between the outer collar structures and the central uplift there is a prominent negative magnetic anomaly that extends in a broad semicircular belt; 2 to 4 km wide around most of the basement core. This anomaly is attributed to the contact of the ILG and OGG, the so-called Vredefort discontinuity (Hart et al., 1990).

Beiki and Pedersen (2010) analyze the Tzz component of the GGT data of the Vredefort dome area using an eigenvector analysis to estimate the depth and a dimensionality (*I*) parameter of the source. The dimensionality is a parameter that lies between zero and unity for any potential field (Beiki and Pedersen, 2010). If the causative body is strictly 2D, then *I* is equal to zero and approaches unity when the causative body is 3D-like. Using this method the authors show that quasi 2D geologic bodies are dominant specially in the outer rim, with depth to sources between 1000-1500 m or more than 1500, but in the central part of the dome the dimensionality approaches unity and the depth exceeds 1500 m. (Fig. 5.11).

Wilson et al., (2011) developed massively parallel software for inversion of gravity and gravity gradiometry data. They invert simultaneously all components of GGT and use a very large number of cubic cells of just 25m side. These authors extend their model only to 2400m depth and obtain results very similar to Beiki and Pedersen (2010).

Martinez and Li (2011) invert the single component T_{zz} of the gravity gradient tensor (GGT) and perform also a joint inversion of three components of the GGT tensor data: the two observed component (Tuv and Txy) and the calculated component Tzz.

They show that the joint inversion of these three components improves the model resolution, providing a more focused central high density structure. Their model shows the presence of dense rocks corresponding the central uplift at a depth of about 6000 m depth and also corresponding to the gravity highs in the outer collar at depths of about 2000 m.

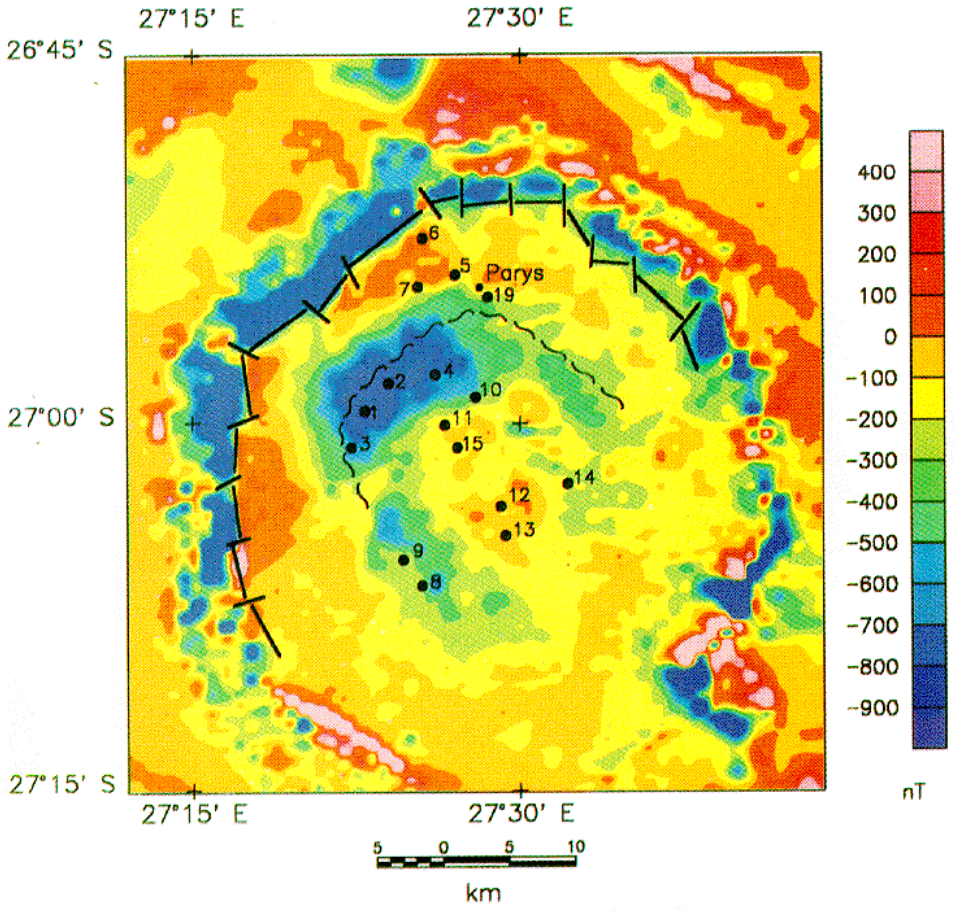

Figure 5.10 *Aeromagnetic anomaly map of Vredefort Dome area (from Hart et al 1995)*

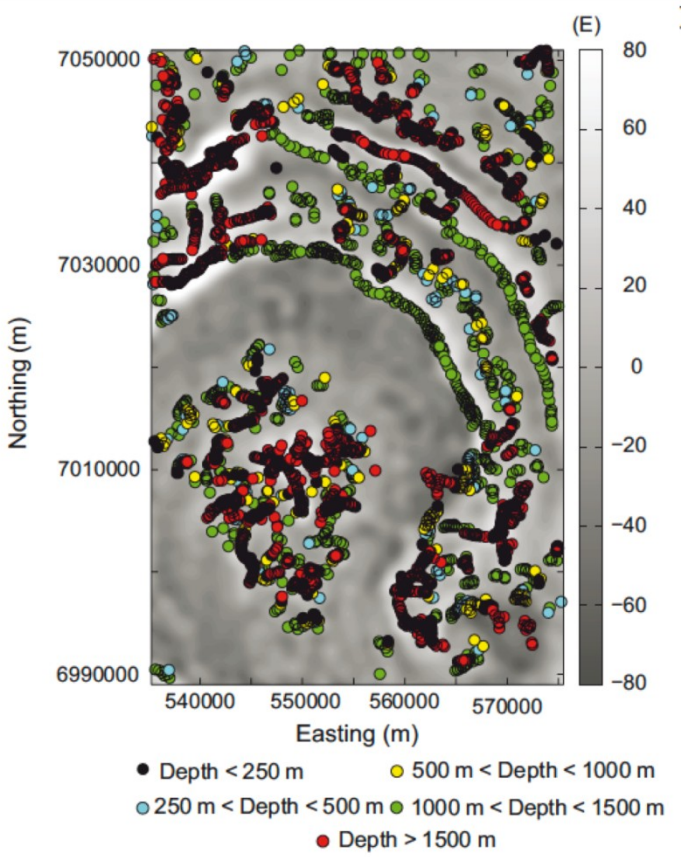

Figure 5.11. *Location and depth to the center of mass of gravity sources as estimated by Beiki and Pedersen (2010)*

5.3.2 GGT data

The gravity gradient tensor (GGT) data used in this work were acquired using the Falcon system by Fugro Airborne surveys. The data are were acquired with a north-south line spacing of 1 km and with east-west tie-lines 40 km spaced, over an area 60 km wide in the north-south direction and 40 km wide in the east-west direction covering most of the Vredefort Dome structure. The data were acquired flying draping the terrain with a ground clearance of about 80 m, corresponding to ellipsoidal heights in the range 1430–1740 m (Dransfield, 2010). In the Falcon AGG system, the full GGT is derived from the measured horizontal curvature components *Txy* and (*Txx*-*Tyy*)/2 (Dransfield and Lee, 2004). In Fig. 5.12 we show the two measured components and the component Tzz.

The terrain effect was removed using a density of 2.67 g/cm^3.

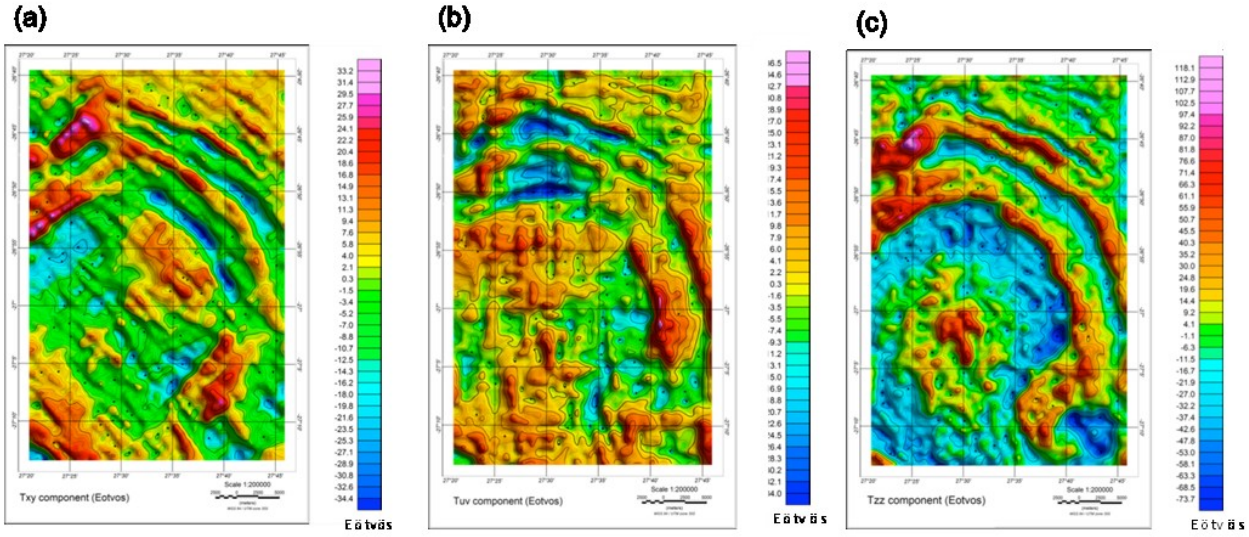

Figure 5.12. *a) Txy component; b) Tuv component (Txx-Tyy/2); c) Tzz component. The Txy and Tuv are measured, the Tzz is calculated.*

Observing the Tzz component (Fig. 5.12 c), we can recognize an alternation of highs and lows of semicircular shape.

Comparing the geological map (Fig. 5.8) with the Tzz component (Fig. 5.13), a good correlation between semicircular gravity anomalies and the geological units of the supracrustal strata can be noticed. In detail, the Dominion Group and the Lower Witwatersrand Group position correspond to the central maximum area, the Upper Witwatersrand Group position correspond to the minimum area and finally the Ventersdrop Supergrup corresponds to the external maximum anomaly.

Furthermore, the outline of the contact between the ILG and OGG (Hart et al., 1995, white circle in Fig. 5.13) separates very well, on the Tzz map, the central high area from the surrounding lows.

This good fitting between gravity anomaly and geological units, is in agreement with the average density contrast value of the geologic formations (Tab. 1) (Henkel and Reimold, 1998, Stepto, 1990).

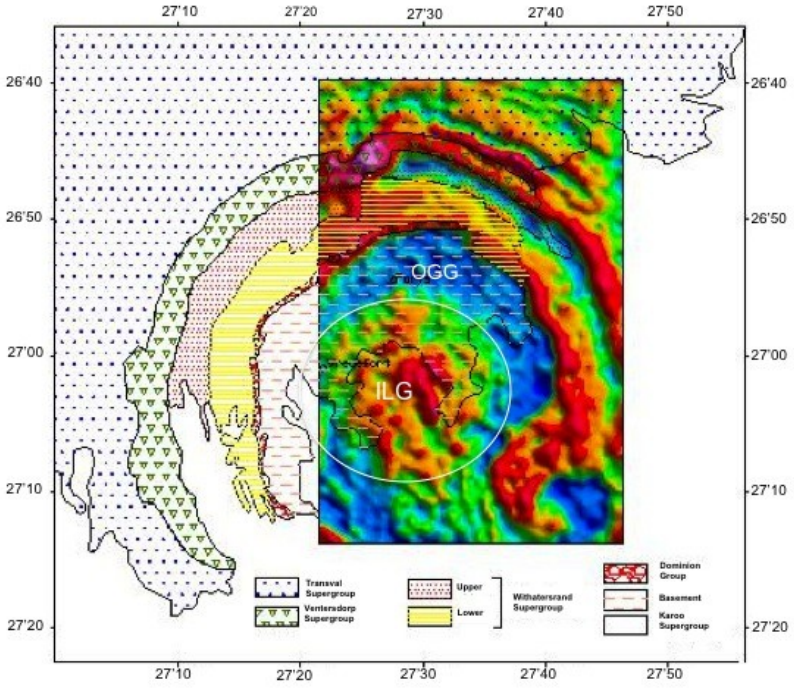

Figure 5.13. *Comparison of Tzz anomaly map and geological formation limits as* from Gibson, et al (2002)

GEOLOGICAL UNIT	DENSITY (g/cm^3)
ILG	2.85
OGG	2.65
WITWATERSRAND	2.72
VENTERSDORP	2.8
TRANSVAAL	2.83

Tab.1. Density of the geological units of the Vredefort Dome area (Henkel and Raimold, 1998, Stepto, 1990)

5.3.3 Inversion Results

The first and preliminary step consists in the estimate of the structural index of major sources. As in the previous cases (paragraph 4.7, Fig. 4.6) we use the scaling function method (Fedi, 2007; Florio et al., 2009), which allows a quick estimate of

this parameter from the analysis of a 3D dataset obtained by upward continuation, (see paragraph 4.7 for more details).

This analysis has identified two distinct groups of sources characterized by different structural indices. Fig. 5.15 shows the scaling function analysis applied to the profile chosen in correspondence of a semicircular shaped anomaly (profile p1 in Fig. 5.14). The second vertical derivative was analyzed, whose ridges are shown in Fig. 5.15a. We choose relatively high altitudes to reduce the high wavenumber noise affecting altitudes closer to the acquisition surface. The intercept of the plot of the scaling function vs. the inverse of the altitude lets us estimate the structural index (Fig. 5.15b), after subtracting from this value the degree of differentiation of the field. In this case N = 2.4 - 2 = 0.4. This value is intermediate between a sheet (N=0) and a pole line (N=1) and suggests that the source that generates the anomaly may be interpreted in terms of dike-like structure with a finite thickness.

Fig. 5.16 shows the same analysis for the second profile considered (profile p2 in Fig. 5.14), chosen to correspond to the central maximum of the gravity anomaly map.

The third order derivative of the field was again selected along with the high altitude portion of the ridge (Fig. 5.16a). In this case, the estimated structural index was found to be equal to N = 4-2 = 2 (Fig. 5.16b). This value suggests that the source that generates the anomaly intersected by the profile can be approximated by a sphere.

These results are in substantial agreement with the analysis of the eigenvectors of the gravity gradient tensor of Beiki and Pedersen (2010).

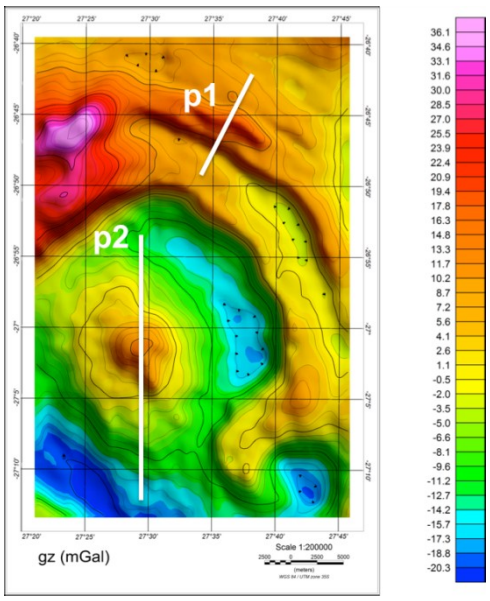

Figure 5.14. *Gravity field of Vredefort Dome area, with the two profiles chosen for the scaling function analysis.*

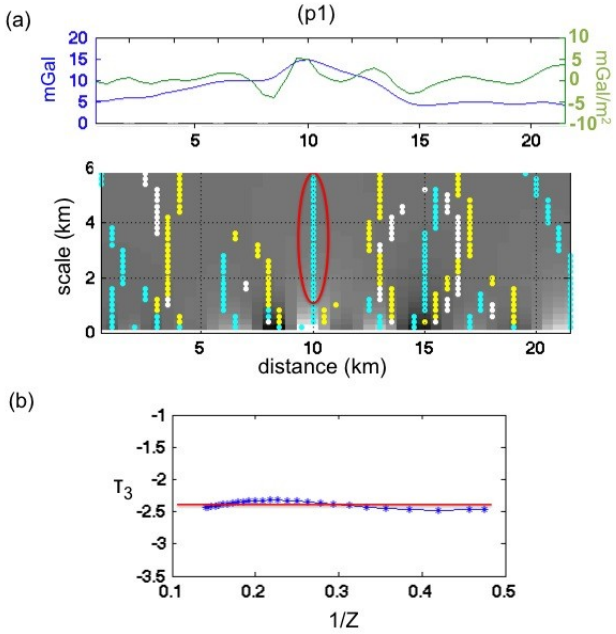

Figure 5.15. *Scaling function analysis applied on profile p1*

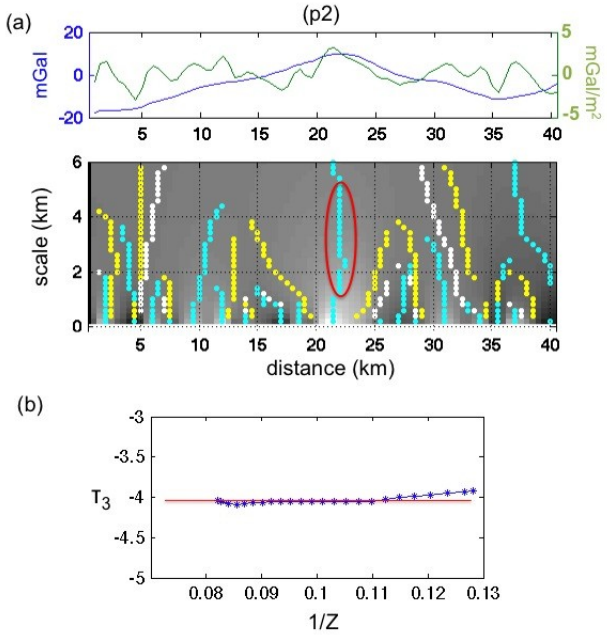

Figure 5.16. *Scaling function analysis applied on profile p2*

As described in the previous Sections, in this case the structural index varies in the analyzed area and consequently if we we use a unique value of β as the exponent of the weighting function we will not be successful in correctly identifying the depth for all the sources. Thus we adopt the approach described in Section 5.2.2 and perform two distinct inversions using different exponents for the depth weighting function, and precisely we use β=3 and β=1.4 corresponding to the values of *N* found by the scaling function analysis, increased by 1 to make them consistent with the corresponding values for the magnetic field, according to the invariance rules (Chapter 4).

We discretized the source domain with 125 x 82 x 70 cells of 500 m in the *x* and *y* direction and 250 m in the *z* direction.

In Fig5.17a we show the density model from inversion of T_{zz} component using β=3 (the isosurface is related to 0.12 g/cm^3). This value of β was estimated for the central compact structure (see Fig5.14) so should allow a correct estimate of depth

only for this region of the map. The depth estimated is about 6000 m for the source center. This estimate is in agreement with the model obtained by Martinez and Li (2011) for the same T_{zz} component. The structure can hence be interpreted as a crustal uplift, which is in agreement with the model by Henkel and Reimold (1996, 1998).

The depth of the structure in outer collar, instead, cannot be estimated accurately with β=3 (it is overestimated). In Fig. 5.17c we show the depths relative to maxima values of the density model as colored dots superimposed to the T_{zz} map. These depths should correspond to the center of the structure. To compare our results with those of Beiki and Pedersen (Fig. 5.11) we use the same depth ranges in this plot. It is possible to see that our model presents density sources at greater depths in the outer collar area, whereas is not possible compare precisely the two solutions for the central area because the representation of Beiki and Pedersen is too vague, indicating only solutions >1500 m . However our solutions in the central area are in the same range of depths.

In Fig. 5.18a we show the density model from inversion of T_{zz} component using β=1.4 (the isosurface is related to 0.05 g/cm^3). This value of β was estimated for the elongated structure of the outer collar (see Fig. 5.14) and should allow a correct estimation of depth for the elongated outer collar structures. For these structures we obtained a depth of about 1000 m. Comparing our model with that of Beiki and Pedersen for these structures we found a very good agreement (Fig. 5.18c). Consistently with the found structural index, indicating a dyke-like source with a finite thickness, this structure should represent a flank of the synclinal fold, made of metasediments and metavolcanics strata, in agreement with the geological model of Gibson et al. (2002).

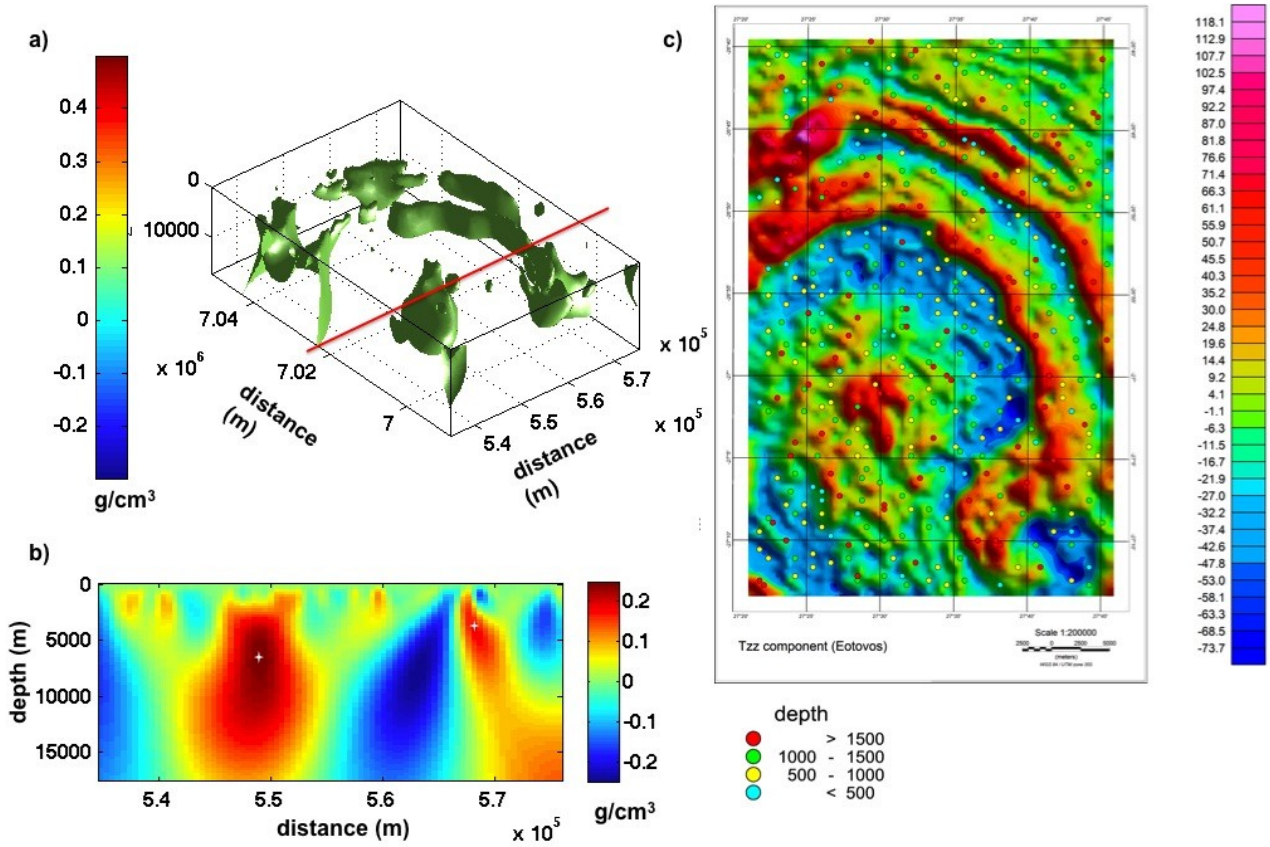

Figure 5.17. *a) Density model obtained from inversion of Tzz component and using β=3 (the isosurface is related to 0.12 g/cm^3); b) Cross section through the 3D model in correspondence of the red line shown in Fig. 5.17a; c) T_{zz} map with colored dots indicating the depths relative to maxima values of the density model.*

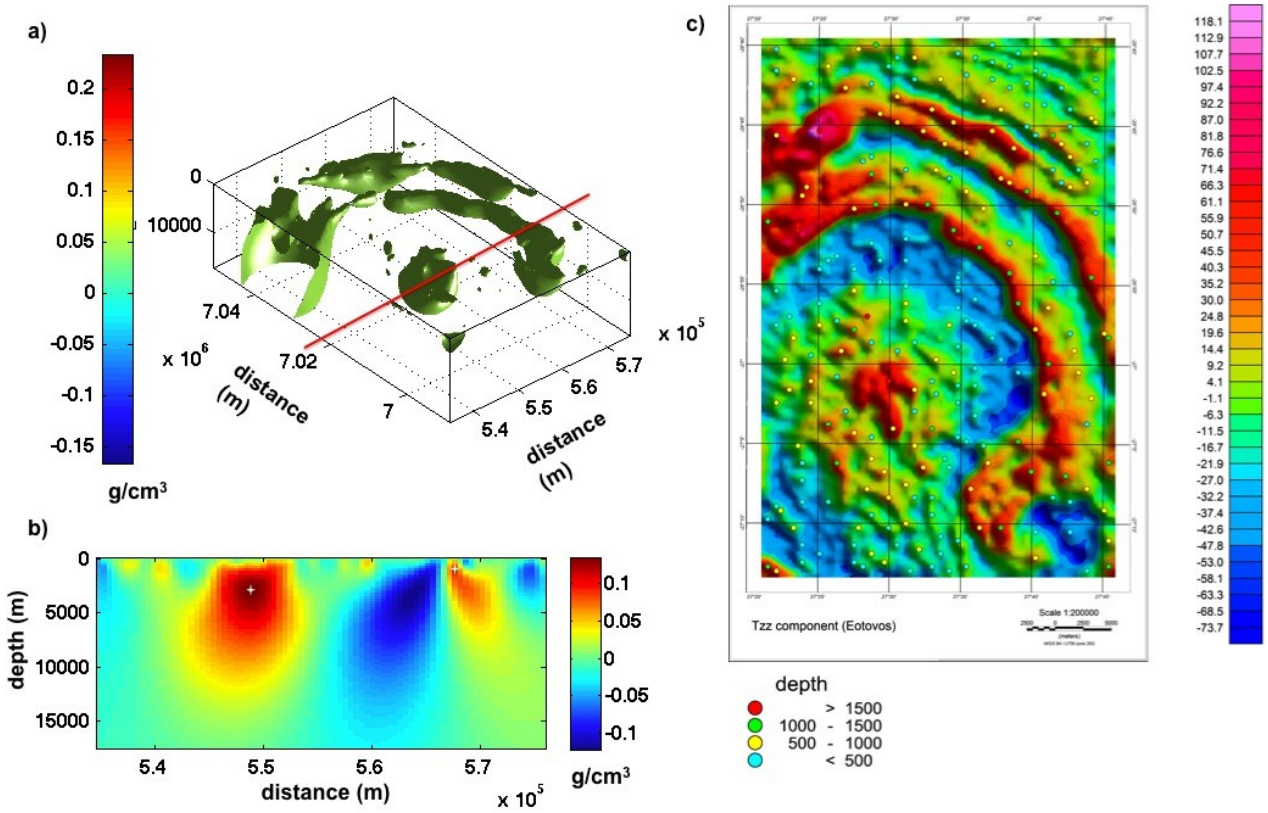

Figure 5.18. *a) Density model obtained from inversion of Tzz component and using β=1.4 (the isosurface is related to 0.05 g/cm^3); b) Cross section through the 3D model in correspondence of the red line shown in Fig. 5.18a; c) T_{zz} map with colored dots indicating the depths relative to maxima values of the density model..*

CHAPTER VI

Self constrained inversion

6.1. Introduction

In Chapter 3 we discussed about the importance to use a priori information to reduce the ambiguity and obtain a unique solution representing a realistic geological model of the subsurface.

In this Chapter we distinguish between external (deriving from wells, geological and geophysical information) and potential field-based constraints, such as the structural index and the position and dip of the source edges, and we present a "self-constrained" inversion procedure that uses as constraints objective information derived exclusively from the intrinsic properties of the potential field anomaly itself. This approach represents the natural following of the multiscale analysis employed by Cella et al. (2009), who integrated boundary analysis with the DEXP method (Fedi, 2007) to retrieve effective information about the field sources.

6.2. Self-Constrained Inversion

In this section we study how the solution changes by varying the constraints and we analyze the dependency of the solution on the depth weighting exponent β, using the Li and Oldenburg algorithm (2003), described in Chapter 3.

To do this, we utilize different types of constraints retrievable from potential field data analysis: *a)* the structural index *N*, which may be estimated through well-known methods such as *Euler Deconvolution* (e.g., Barbosa et al., 1999; Nabighian and Hansen, 2001) or through multiscale methods such as the *Multiridge Euler*

Deconvolution (e.g., Florio and Fedi, 2006; Fedi et al., 2009) and *Scaling Function Method* (e.g., Florio et al., 2009); *b)* the depth to the top or to the center of the source, as estimated by methods such as the *Multiridge Geometric Method* (Fedi et al., 2009), the *DEXP Method* (Fedi, 2007), and/or the above cited *Multiridge Euler Deconvolution* and *Scaling Function Method*; *c)* the position of the source edges, which may be estimated through the computation of the horizontal gradient (Cordell and Grauch, 1985) and/or by the *Enhanced Horizontal Derivative Method* (Fedi and Florio, 2001); *d)* the dip of the edges of the source, inferred by methods such as the cited *Multiridge Geometric Method* and the method proposed by McGrath (1991).

The well-known *Euler Deconvolution* is used to retrieve information about source positions and depths. This method can also be used as a multiscale technique by analyzing the data along potential field ridges, which are lines defined by the position of the extreme points of the field at different scales. Euler equations are notably simplified along any of these ridges. Since a given anomaly may generate one or more ridges, *Euler Deconvolution* may be used to jointly invert the data along all them, so performing a *Multiridge Euler Deconvolution*. Along with this method, the *Geometric Method* is built by joining extreme points of the analyzed field at different altitudes and uses a geometric criterion to find the structural index and vertical and horizontal source positions.

The *Scaling Function Method* is a multiscale method based on the study of the scaling function of potential fields and it also allows retrieving source parameters such as depth and structural index through an analysis along ridges (see paragraph 4.7 for more details). The *DEXP Method* leads to estimates of source depths and density/magnetization from the extreme points of a 3D field scaled following specific power laws of the altitude; depths to the sources are obtained from the

position of the extreme points of the scaled field, and the excess mass or dipole moment are obtained from the scaled field values.

The position of the maxima of the *Enhanced Horizontal Derivative* signal - obtained by the computation of the horizontal derivative of a weighted sum of vertical derivatives of increasing order - can effectively detect the location of the edges of sources of different extent and depth. The method proposed by McGrath (1991) allows a qualitative estimation of the dip of the source edges, by evaluating the location of the maxima position of the first horizontal derivative computed at different altitudes; as the horizontal position of the maximum at each altitude does not change only over vertical boundaries, the presence of dipping edges can be easily detected.

All the mentioned multiscale methods enjoy good stability thanks to the process of upward continuation. However the continuation implies a loss of resolution. For this reason these methods work always on data transformed through a smoothing-enhancing filter (e.g., Fedi et al., 2009), composed of an upward continuation and a vertical differentiation. This composite filter, when properly tuned, has a response similar to a band-pass filter, removing both high wavenumber noise and regional fields. Application of multiscale methods is therefore preceded by a search for the best continuation altitudes and differentiation orders by looking at the ridges' shape on a vertical section of the transformed field. The correct altitudes may be easily chosen by excluding the lowest altitudes, generally characterized by a low S/N ratio due to the differentiation process, at which numerous ridges extending only to a small number of scales are present. The optimum differentiation order may be chosen by considering that ridges of a homogeneous field generated by an isolated source should be linear (Fedi et al., 2009). Thus, the differentiation order should be increased until the interference is sufficiently low that the ridges tend to be linear.

As already said in the previous Chapter, the structural index *N* determines the exponent β of the depth-weighting function in the regularization matrix. The exponent of the depth-weighting function β is associated to the fall-off rate of field, which can be retrieved by a direct estimate of the structural index *N* (Cella and Fedi, 2012). This allows a good estimation of the depth to the source and gives substantial objectivity to the form of the depth-weighting function and to the consequent solutions. For simplicity we will express all the structural index values as in the magnetic case, with N_{MAG} varying from 0 to 3.

Introducing information about the position of the source edges, i.e., about the source depth-to-the-top, horizontal edges and dip, is important because the model objective function can incorporate prior information into the inversion via a reference model and 3D weighting functions that enhance or attenuate the structural complexity in different directions. Incorporating these horizontal weighting functions in the inversion algorithm (in the term $\mathbf{W}_m$ of eq. 3.12) will lead to solutions well constrained with respect to the depth-to-the-top and horizontal variations of the source-density distribution.

A further information about the magnetization/density upper bound, deriving from studies about the geology of the study area, from other geophysical investigations and from wells, may be possibly added.

6.3. Synthetic Examples

To illustrate and prove the utility of our inversion strategy we present here some gravity and magnetic examples of application to 2D and 3D synthetic sources. We used the same inversion framework as Li and Oldenburg (1996), involving depth-weighting and horizontal weighting functions and we set a positivity constraint for all the inversions.

6.3.1. Vertical Fault Test

The first test regards the analysis, along a profile, of the gravity field generated by a 2D vertical step located at x_0=6000 m, having its top at 300 m depth and a thickness of 2700 m (Fig. 6.1), and with a density contrast of 1 g/cm^3. The source volume is discretized by 200 x 50 cubic cells with 100 m side. Data spacing is 100 m.

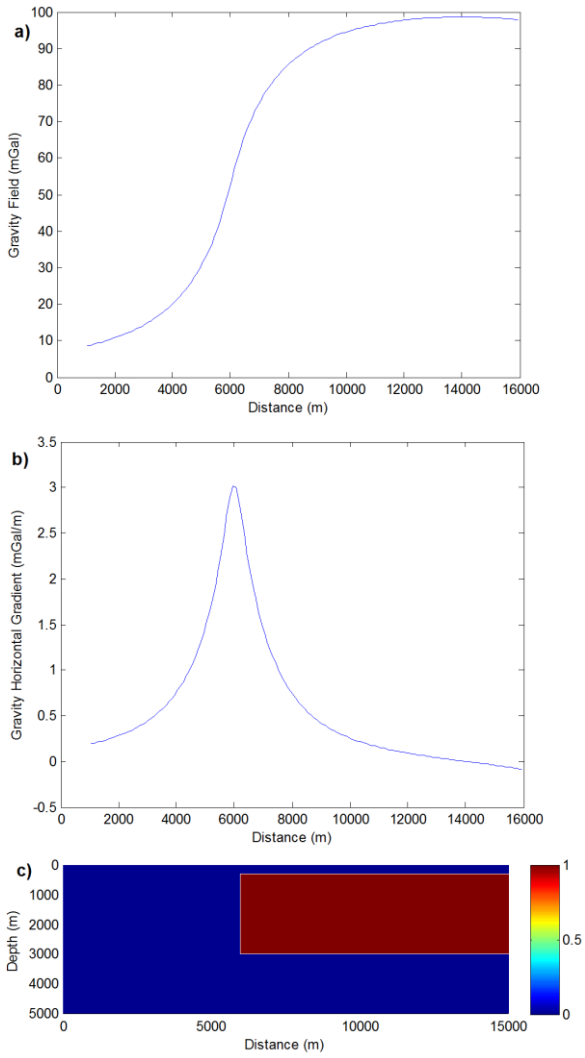

Figure 6.1. *a) Gravity anomaly generated by a vertical fault model with 1 g/cm^3 density, 300 m depth to the top and 2700 m thickness. b) Modulus of the horizontal gradient of the gravity anomaly computed from the field in plot 1a). c) Synthetic fault model. Density in g/cm^3.*

As a first step of our inversion strategy we evaluated the 2D source parameters from the analysis of its gravity field. The *Multiridge Euler Deconvolution* (Fedi et al., 2009) (Fig. 6.2a) allowed the estimation of the source *structural index N* and edge locations along the x and z directions (Fig. 6.2b-6.2c). The results of the analysis, obtained by a differentiation of the third order of the field computed to low continuation altitudes, showed average values of N_{MAG}=0.15, x_0=5943 m and z_0=340 m. The highlighted depth to the top was confirmed by the *DEXP Method* (Fedi, 2007) (Fig. 6.2e). Finally, the application of the method by McGrath (1991) to data clearly showed that the fault is vertical (Fig. 6.2d). We note that a first estimation of the x_0 location and of the edge dip could already be made by the horizontal derivative computed in Fig. 6.1b, which showed a x_0 value of 6000 m and the presence of a vertical contact. The analyses shown in Fig. 6.2c and 6.2d confirmed the actual x_0 position, with a negligible shift with respect to the actual x_0, and the verticality of the fault.

The found *N*=0.15, which will be used to correctly set up the exponent *b* of the depth-weighting function in the inversions tests (Cella and Fedi, 2012), is very low and characteristic of a contact. The corresponding depth will be relative to the top of the structure. However, at very high altitudes the structure could be seen as a sill, whose *N* is equal 1, and in this case the depth found by inversion will be relative to the centre of the structure.

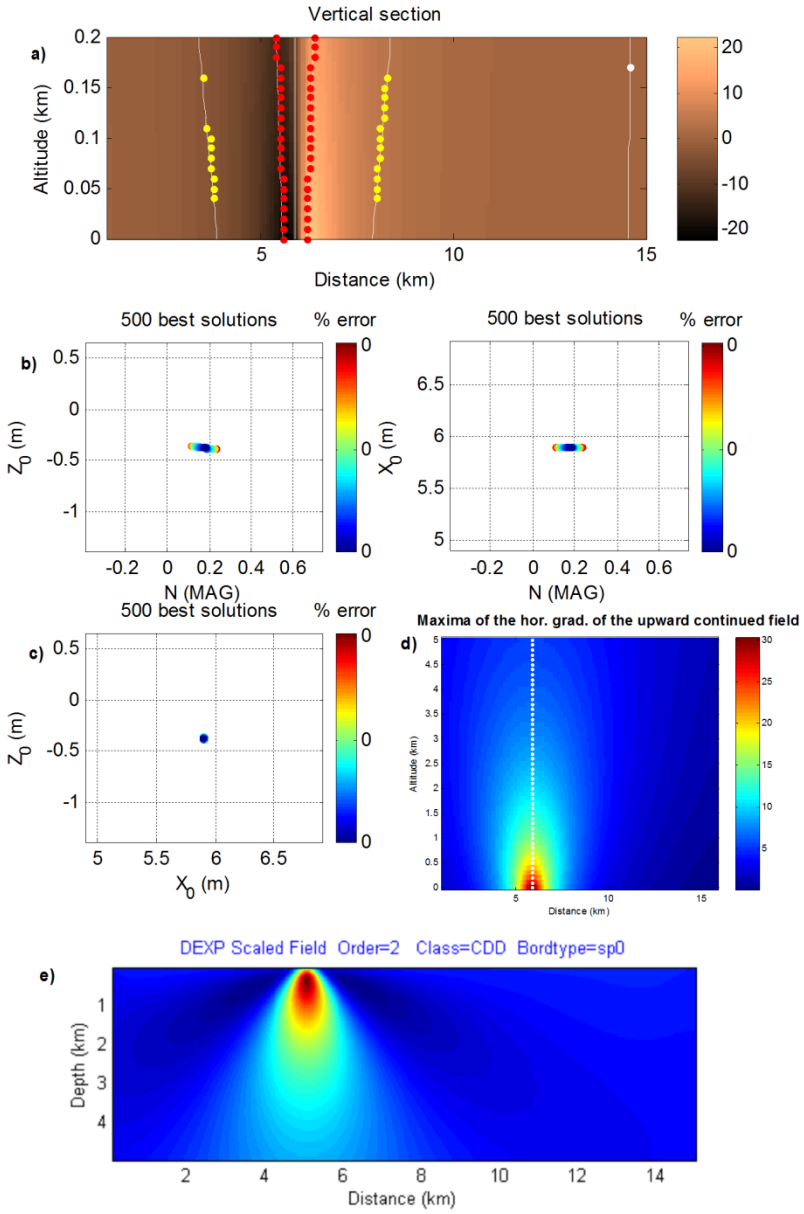

Figure 6.2. *Analysis of the data of the vertical fault shown in Fig. 1a). a)-b)-c) Results of the Multiridge Euler Deconvolution giving information about the source N, x_0 and z_0. d) Plot of maxima of the horizontal gradient of the upward continued field showing that the faults is vertical. e) DEXP analysis yielding information about the source z_0.*

Therefore in our inversion tests (Fig. 6.3) we used both β=N=0.15 to better image the top of the structure (see reconstructions in Fig. 6.3b-c-d), and β=N =1 to have an image of the density distribution more balanced around the structure midpoint (see reconstructions in Fig. 6.3e-f-g).

The reconstruction obtained without any of the cited constraints, i.e., the minimum length solution, lacks of any depth resolution and it is not useful (Fig. 6.3a). The solution model obtained by using as a constraint only the depth-weighting function with the exponent β=0.15 (Fig. 6.3b) shows a maximum density distribution located at the correct depth-to-the-top, thanks to the correct estimation of the depth-weighting function performed by the *Multiridge Euler Deconvolution* (Fig. 6.2a-b). We notice however that the recovered reconstruction is blurred and provides no clear information about the source top and horizontal boundaries. So, according to our procedure, we repeated the inversion by adding a further constraint about the horizontal position of the source edge and about the edge dip (Fig. 6.3c). This information was added by imposing a strong vertical density variation in correspondence with the x_0 found by the above mentioned analysis methods (Figure 6.2d and 6.2e). The results of the analyses shown in Fig. 6.1b and 6.2b and 6.2d let us set up the constrained inversion so that an abrupt-vertical density change was favored to occur at x_0=6000 m, and at any depth. So at this stage we did not input information about the source depth yet, other than that based on *N*. A last constraint about the depth-to-the-top was finally added in the reconstruction shown in Fig. 3d: the solution is now more focused, and both the top and horizontal edge are clearly detected. The density distribution is still not uniform, but close to the real value (1 g/cm^3).

Similar conclusions may be drawn when using β=*N*=1, which allows obtaining a density distribution more balanced around the structure midpoint (see reconstructions in Fig. 6.3e-f-g). The edge and dip-constrained solutions obtained using β= 0.15 and β=1 are actually rather similar, with a better reconstruction in the deeper part of the source when using β=1, as it should be expected. This allowed us to conclude that when adding constraints other than the only depth-weighting (such

as edge position, depth-to-the-top and dip), the choice of the value of depth-weighting is no more so decisive in correctly shaping the source distribution.

A further improvement to our reconstruction could be achieved by including also an upper bound for the density. This information is not always available, but geological considerations or well-logs may allow establishing a reasonable value.

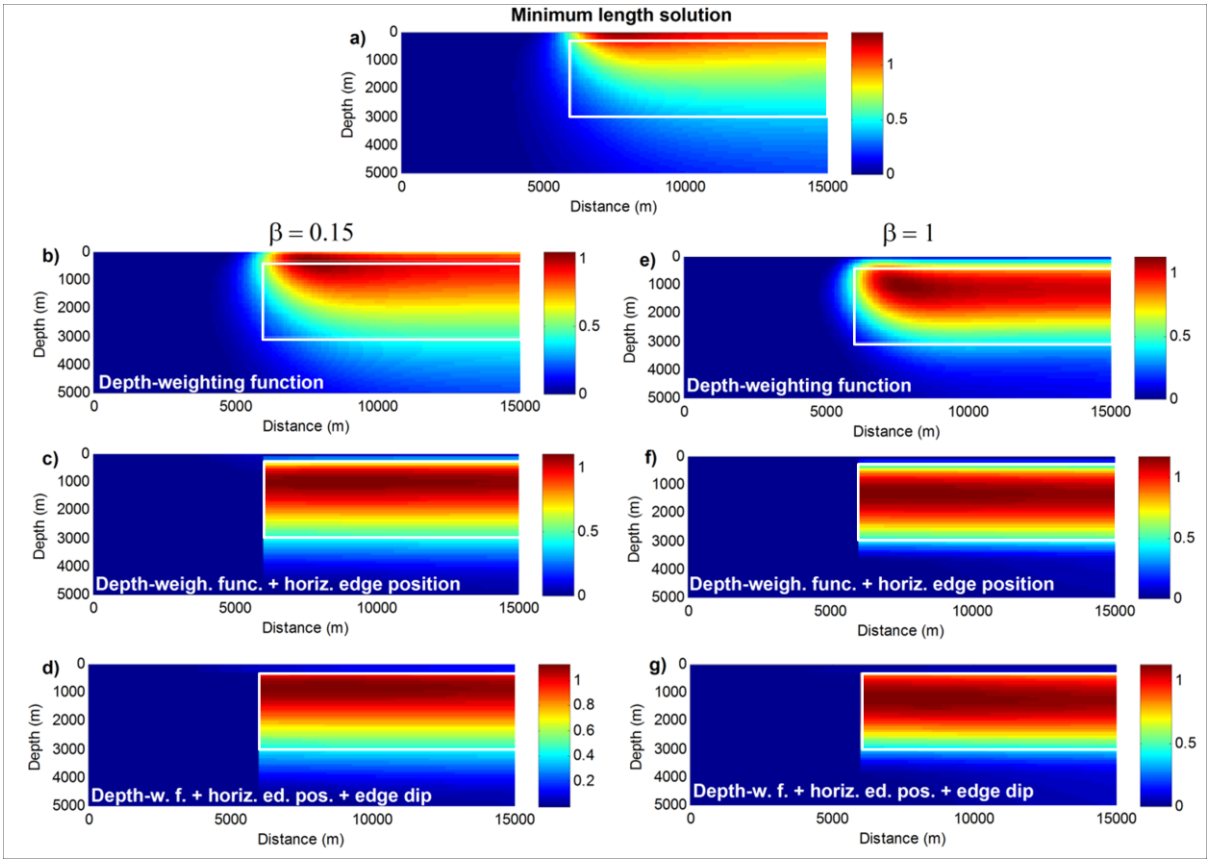

Figure 6.3. *Density models (in g/cm^3) obtained from the inversion of the vertical fault data in Fig. 6.1a) by resorting to different self-constraints: a) reconstruction obtained without any self-constraint. This solution lacks any depth resolution and is not useful. b) Density solution constrained by using a depth-weighting function with β=N=0.15 retrieved from the data analysis (see Fig. 6.2b). The source top is reconstructed at its correct depth, but the recovered density distribution is blurred. c) Solution with the additional constraint coming from the edge horizontal location and from the dip evaluation (see Fig. 6.2c and 6.2d, respectively): the reconstruction is well constrained with respect to the source edge and dip and shows information about the density distribution. d) Solution with a further constraint on the location of the source depth-to-the-top (see Fig. 6.2c and 6.2e): the solution is now more focused, with both the top and horizontal edge clearly detected. e)-f)-g) Same as plots 6.3b)-c)-d) but using β=N=1, which allows obtaining a density distribution*

more balanced around the structure midpoint. In all the panels the white lines outline the actual source position.

6.3.2. Dipping Fault Test

The second test regards the analysis, along a profile, of the gravity field generated by a 2D dipping fault with an inclination of 45°, whose upper edge is located at x_0=6000 m. The step has its top at 300 m depth, a thickness of 2700 m (Fig. 6.4) and a density contrast of 1 g/cm^3. The source volume discretization and data spacing are the same as for the vertical fault test.

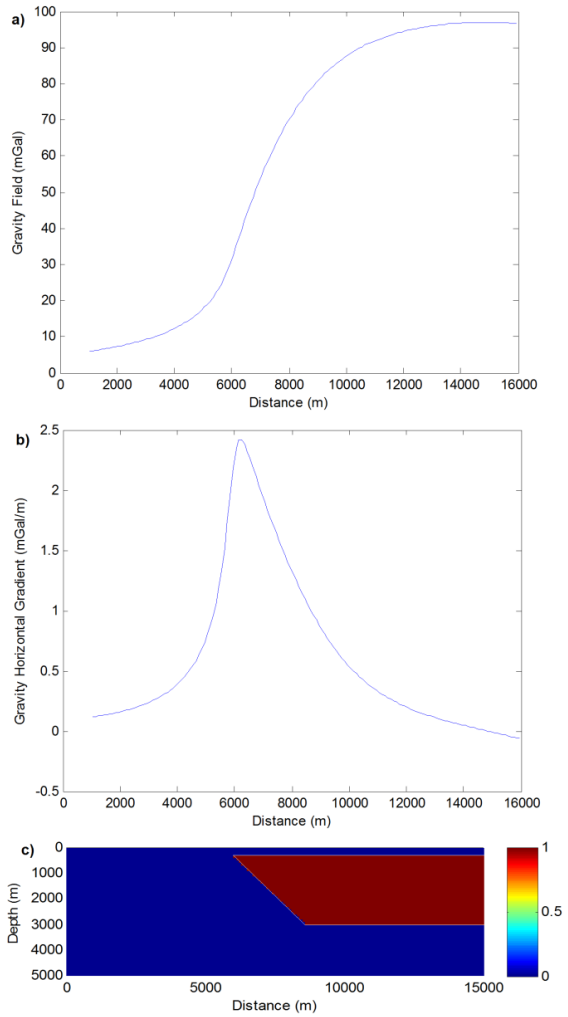

Figure 6.4. *a) Gravity anomaly generated by a dipping fault (45°) model with 1 g/cm^3 density, 300 m depth to the top at x_0 = 6000 m and 2700 m thickness. b) Modulus of the horizontal gradient of the gravity anomaly computed from the field in a). c) Synthetic fault model. Density in g/cm^3.*

We followed the same strategy carried out for the previous test and therefore we firstly evaluated the 2D source parameters from the analysis of its gravity field. Use of *Multiridge Euler Deconvolution* (Fedi et al., 2009) (Fig. 6.5a) allowed the estimation of the source *structural index N* and of the edges' locations along the x and z directions (Fig. 6.5b-6.5c). The results of the analysis, obtained by a mixed differentiation of the 3rd order of the field $\left(\partial^3 f / \partial x^2 z\right)$ computed at low altitudes, showed average values of N_{MAG}=0.15 and z_0=345 m. The highlighted depth to the top was confirmed by the *DEXP Method* (Fig. 6f; Fedi, 2007). The DEXP section shows also an asymmetry of the scaled field with respect to a vertical line, consistent with the source dip and interpretable as a qualitative estimate of the source dip. The application of the method by McGrath (1991) clearly showed that the fault is dipping towards the East (Fig. 6.5d). The *Multiridge Geometric Method* (Fedi et al., 2009) was applied to the 3rd and 1st order vertical derivatives to obtain 2 estimates of the source position, relative to different points along the sloping boundary. These estimates were used to calculate the dip of the sloping boundary. The dip turned out to be 46°, which is in agreement with the true dip of 45°.

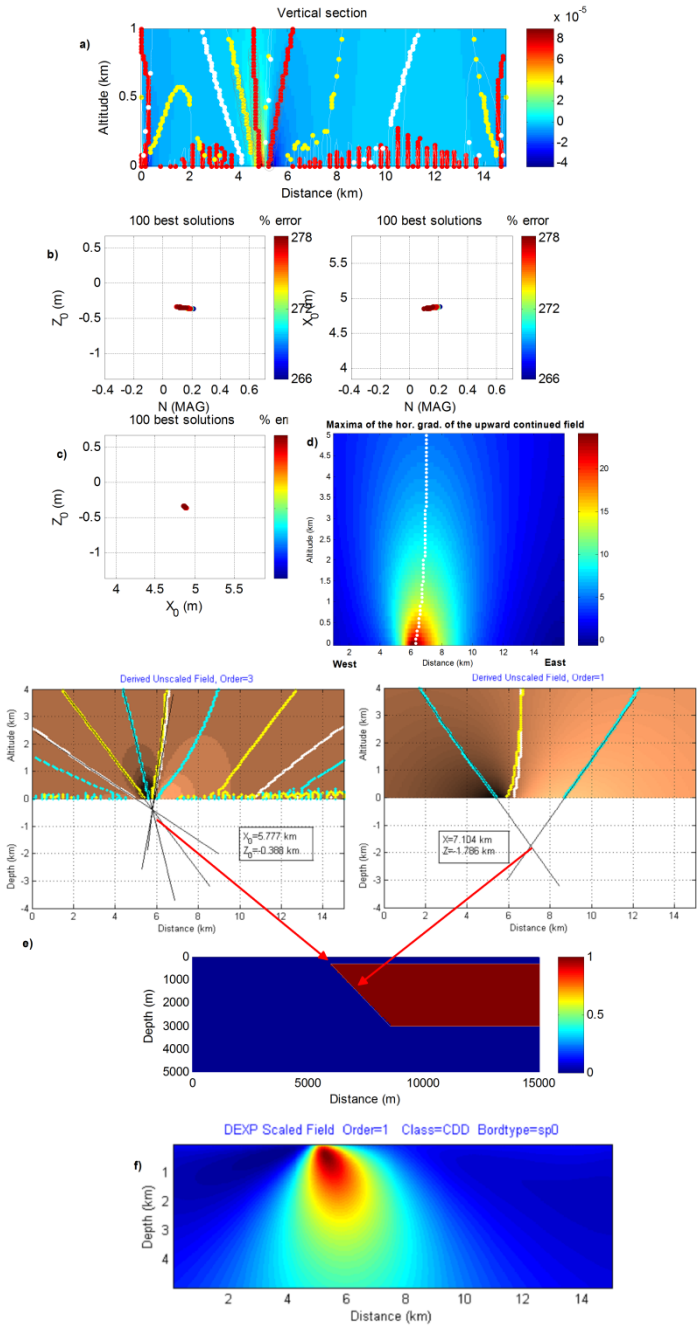

Figure 6.5. *Analysis of the data of the dipping fault shown in Fig. 6.4a). a)-b)-c) Results of the Multiridge Euler Deconvolution giving information about the source N, x_0 and z_0. d) Plot of maxima of the horizontal gradient of the upward continued field showing that the faults is dipping towards East. e) Multiridge Geometric method applied to the third and first order vertical derivatives to obtain position estimates of the upper and lower part of the dipping fault edge. f) DEXP analysis yielding information about the source dip and z_0.*

Similarly to what was done for the vertical fault, the parameters estimated from the analysis of the gravity field of the dipping fault were used to constrain the inversion tests (Fig. 6.6). The constraint about the horizontal position of the source edge was added by imposing a strong density variation along the dipping surface found by the *Multiridge Geometric method* (Figure 6.5f and 6.5g). We used again both the indices *N*=0.15 and *N*=1 to better image the top of the structure (see reconstructions in Fig. 6.6b-c-d), and the midpoint of the fault, respectively (see reconstructions in Fig. 6.6e-f-g). The outcome of the inversions are similar to that obtained for the vertical fault, with a better uniformity of the density distribution for the reconstructions of the dipping fault constrained with respect to the edges and dip of the source. We note that the solutions obtained by using β = 0.15 and β =1 and adding the edge and dip constraints are very similar and this leads us to conclude again that the introduction of other constraints makes the information relative to depth-weighting not so crucial for correctly reconstructing the source features.

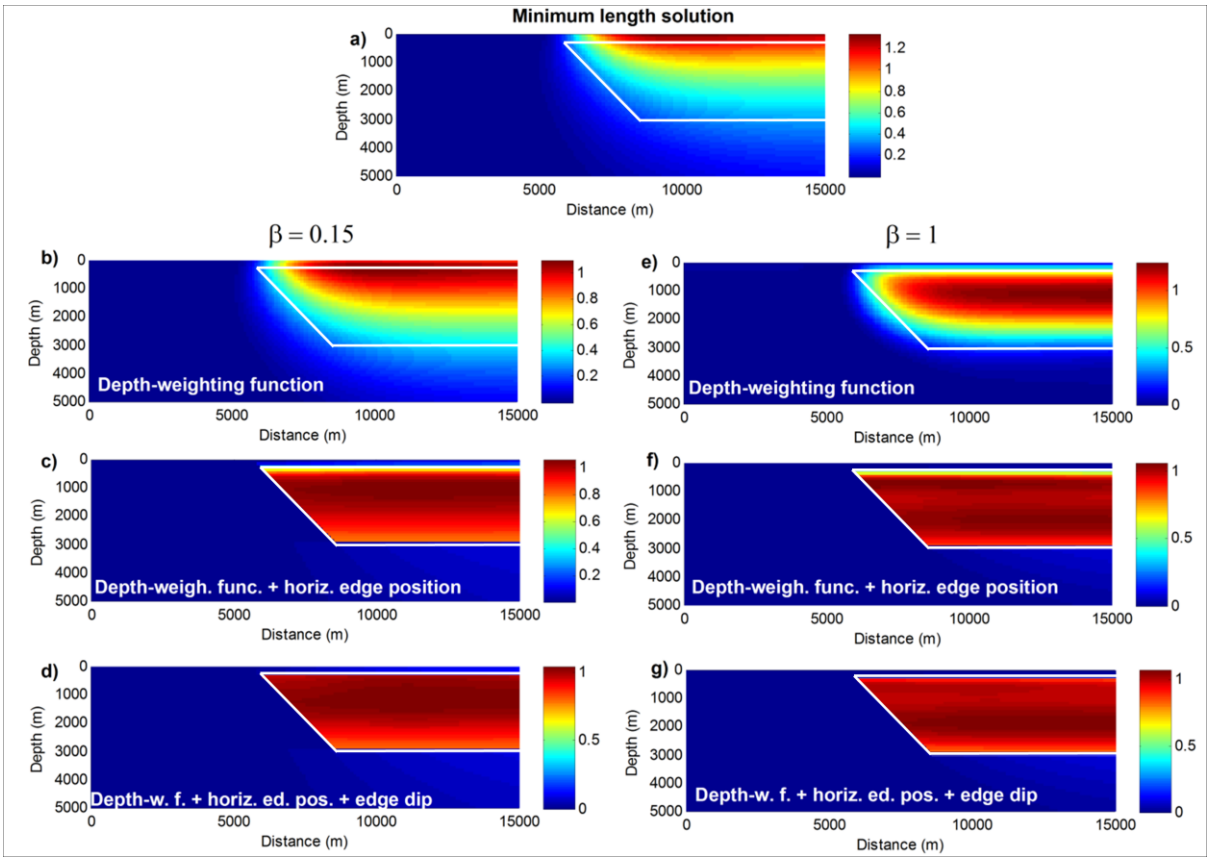

Figure 6.6. *Density models (in g/cm^3) obtained from the inversion of the dipping fault data in Fig. 6.4a) by resorting to different self-constraints: a) reconstruction obtained without any self-constraint. b) Density solution constrained by using a depth-weighting function with β=N=0.15 retrieved from the data analysis (see Fig. 6.5b). c) Solution with the additional constraint coming from the edge horizontal location and from the dip evaluation (see Fig. 6.5c and 6.5d, respectively). d) Solution with a further constraint on the location of the source depth-to-the-top (see Fig. 6.5c and 6.5e). e)-f)-g) Same as plots 6.6b)-c)-d) but with β =N=1, which allows obtaining a density distribution more balanced around the structure midpoint. In all the panels the white lines outline the actual source position.*

6.3.3. Two Body Source

The third test involves the magnetic field (Fig. 6.7a) generated by two 3D prismatic sources, which are located rather close to each other, with a location for the shallow source at x: 2200-2700 m, y: 1400-2000 m, z: 150-450 m and for the deep source at x: 2100-2800 m, y: 2500-3300 m, z: 450-850 m (Fig. 6.7c). The source volume is discretized by 50 by 50 by 25 cells, with a 100 m by 100 m by 50 m side. Data

spacing is 100 m and the directions of the inducing field and of the source magnetization vector are both vertical.

The location of the source edges was inferred by the computation of the *Enhanced Horizontal Derivative* signal (Fedi and Florio, 2001) (Fig. 6.7b). The EHD signal was composed by using the field, the first and the second vertical derivatives, and unit weights. The maxima of the EHD signal picked out the actual position of the edges of the two sources, except for a slight shift, due to interference of the signals of the two sources, in correspondence with one edge of the deeper source along the y axis.

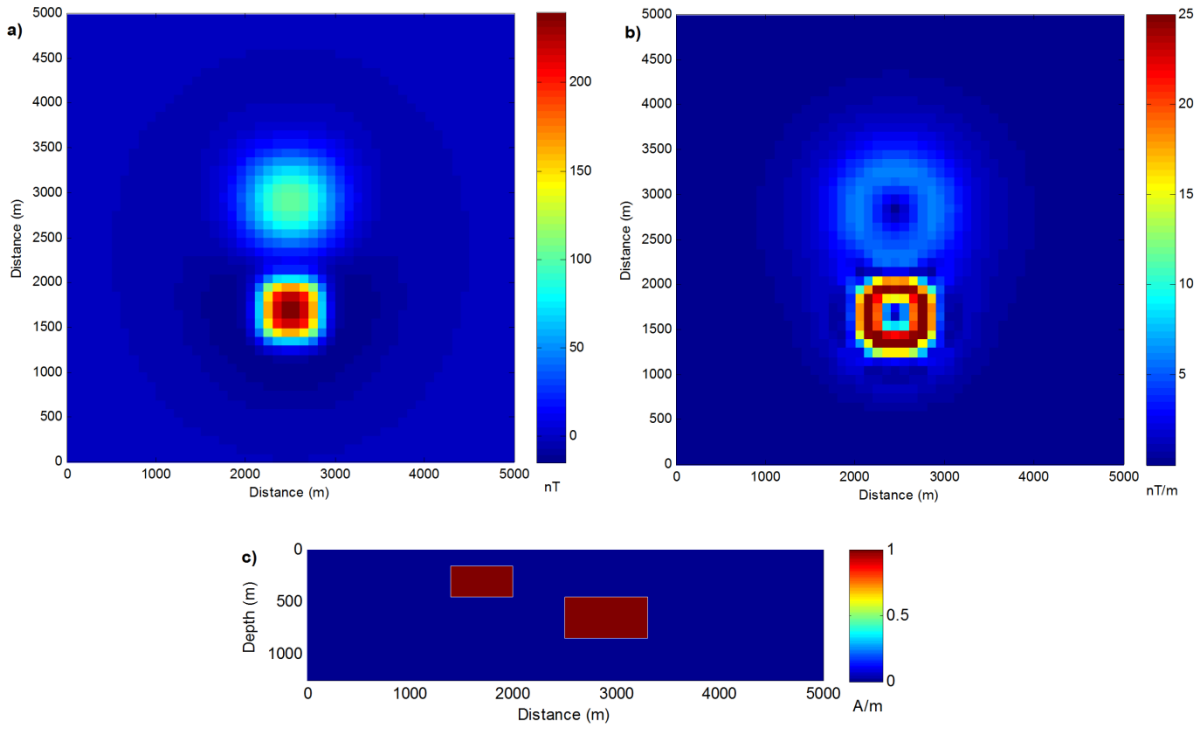

Figure 6.7. *a) Total field generated by two 3D magnetized prismatic sources with contrast of 1 A/m. See text for details about the sources' location. b) Enhanced Horizontal Derivative signal, whose maxima outline the source edge position. c) S-N vertical section of the synthetic model at x=2500 m.*

The *Scaling Function* analysis (Florio et al., 2009), carried out for both sources (Fig. 6.8a-b) through the computation of the third order vertical derivative of the total field, yielded information about the sources' depth and structural index *N*. For the shallow source we retrieved z_0: 250 m and N_{MAG}=2.2, while for the deep source we found z_0: 690 m and N_{MAG}=2.7. With the values of N not being an integer, these depths are expected to determine an intermediate point between the top and the center.

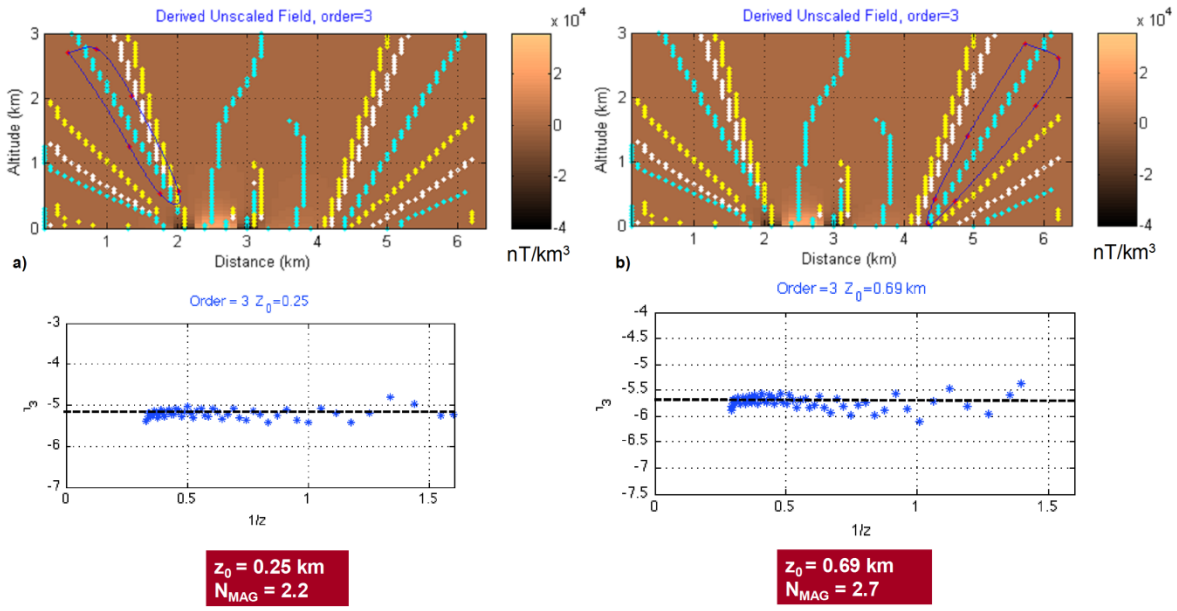

Figure 6.8. *Scaling Function analysis carried out on the magnetic data in Fig. 6.7a). A ridge for each anomaly was selected from the vertical section of the third order vertical derivative of the field (a and b); The plots of the rescaled scaling function by using the depths of 0.25km (shallow source) and 0.69 km (deep source) vs. the inverse of altitude are linear and the intercept represents the value of* N_{MAG} *+ the differentiation order (3 in this case).*

The inversions (Fig. 6.9) were thus carried out by employing the horizontal constraints located by the boundary analysis and an average *structural index* $N_{av.}$=2.5.

Whereas the reconstruction obtained without any of the retrieved constraints, i.e., the minimum length solution, lacks of any depth resolution (Fig. 6.9a), the solution obtained by using as a constraint only the depth-weighting function with the exponent $\beta = N_{av.}$=2.5 (Fig. 6.9b) shows a magnetization distribution located at the correct depth for the shallower source. However the reconstructed position and magnetization of the deeper source result underestimated and both sources look blurred. The introduction of a further constraint about the horizontal position of the source edges as inferred by the EHD analysis improved significantly the reconstruction in terms of magnetization distribution for both sources (Fig. 6.9c). A further improvement to the reconstruction of the deeper source may be achieved by using as exponent of the depth-weighting function the exact structural index found by the data analysis for this source, i.e., N=2.7 (see Fig. 6.9d).

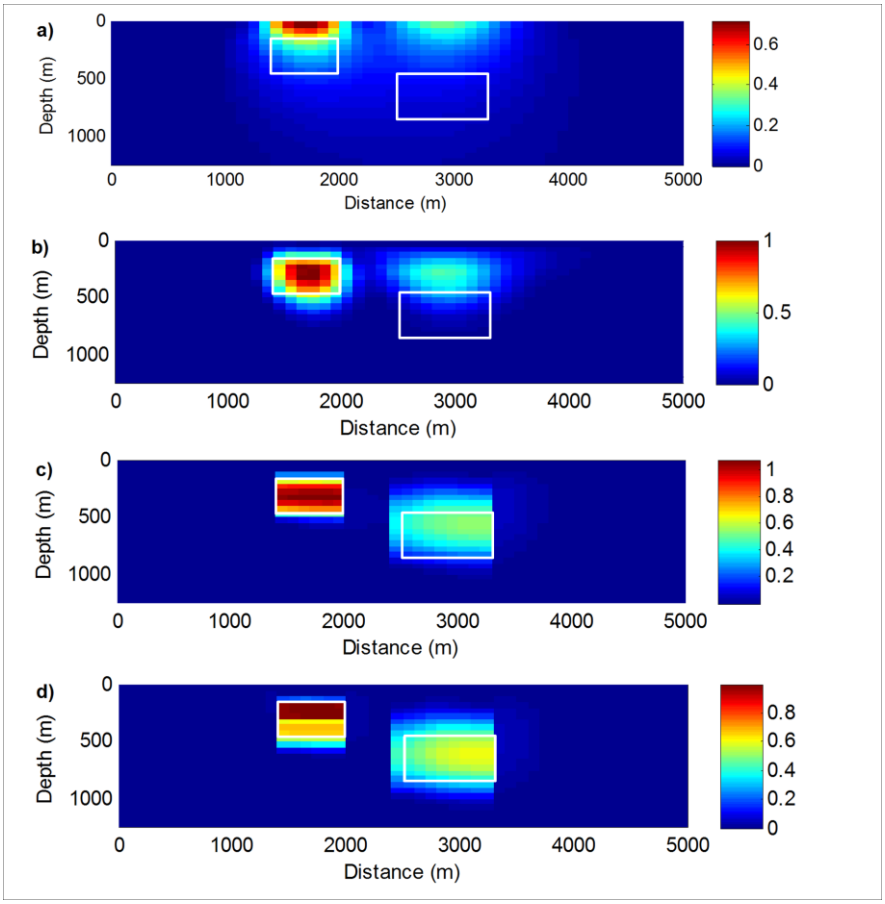

Figure 6.9. *Vertical sections of the magnetization models (in A/m) obtained inverting the data in Fig. 6.8a). a) Minimum-length solution. b) Reconstruction obtained by using a depth-weighting function with an average exponent* $\beta = N_{av.} = 2.5$*. The reconstructed position and magnetization of the deeper source result underestimated and both sources look blurred. c) Solution obtained with the additional constraint deriving from the EHD analysis: the magnetization distribution clearly shows information about the shallower source depth, edges and magnetization contrast. The deeper source position is well detected but its magnetization is underestimated. d) The use of the exact structural index found for the deeper source, i.e., N=2.7, as exponent of the depth-weighting function allows an improvement in the reconstruction of the magnetization distribution for the deeper source. The actual sources' position is shown by white boxes.*

6.4. Real Data Example

As an application of our inversion procedure to a real case, we carefully digitized the gravity data reported in Stavrev and Reid (2010) collected along a profile over the Venelin-Aksakov fault, which is located in the western bound of the Dolna Kamchia west-east trending depression, Eastern Bulgaria (Fig. 6.10a-b). Geologic and gravity data suggest the existence of a steep contact structure trending north-south between low-density Tertiary/Upper Cretaceous layers and the denser lower Cretaceous and deeper sediment layers. Core samples show a density contrast between the two complexes of 0.23 g/cm^3. The depth to the lower Cretaceous surface was found to be about 100 m in western part of the analyzed profile (drillholes W-3 and W-4, Fig. 6.10a) and greater than 1250–2000 m in south-eastern areas (drillholes W-66 and W-27). The interpretative results from the analysis by Stavrev and Reid (2010), selected by the authors on the basis of the geologic information, showed: *i)* a depth of 195 m for the upper edge point of the fault structure at a location x_0 = 5875 m; *ii)* a depth to the lower edge point of the contact of 2690 m.

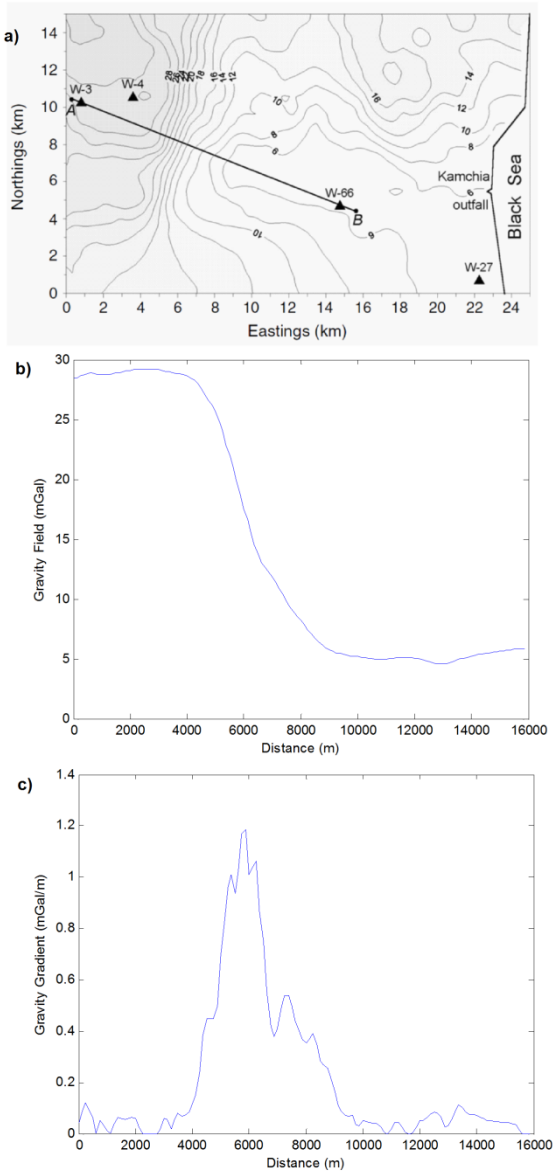

Figure 6.10. *The real case of the Venelin-Aksakov fault, Bulgaria. a) Gravity map collected in the study area (from Stavrev and Reid, 2010). b) Gravity data along the profile shown in plot a); c) Modulus of the horizontal gradient of the gravity anomaly computed from the field in plot b).*

Following our inversion strategy, we firstly evaluated the fault parameters to be used as constraints from the analysis of its gravity field. The *Multiridge Geometric Method* (Fedi et al., 2009) was applied to the first order vertical derivative of the gravity field at low altitudes and then to the gravity field at high altitudes to obtain estimates, respectively, of the position of the upper (Fig. 11a) and lower part (Fig. 11b) of the dipping contact. This resulted in a contact depth-to-the-top of 300 m and

in a dip of 77°. The sub-vertical characteristics of the fault were confirmed by the application of the McGrath method (1991), which showed that the contact is slightly dipping towards the SE (Fig. 11d). We estimated the structural index of the structure by an indirect method, that is selecting the scaling exponent of the *DEXP transformation* (Fedi, 2007) such as the DEXP section gives a depth of 300 m for the upper part of the dipping contact, consistently with the *Geometric Method*. The structural index so resulting was $N_{MAG} = 0.1$ (Fig. 6.11c) and this value, very similar to the theoretical structural index of a contact, implies that the depth of 300 m is relative to the top of the dipping fault.

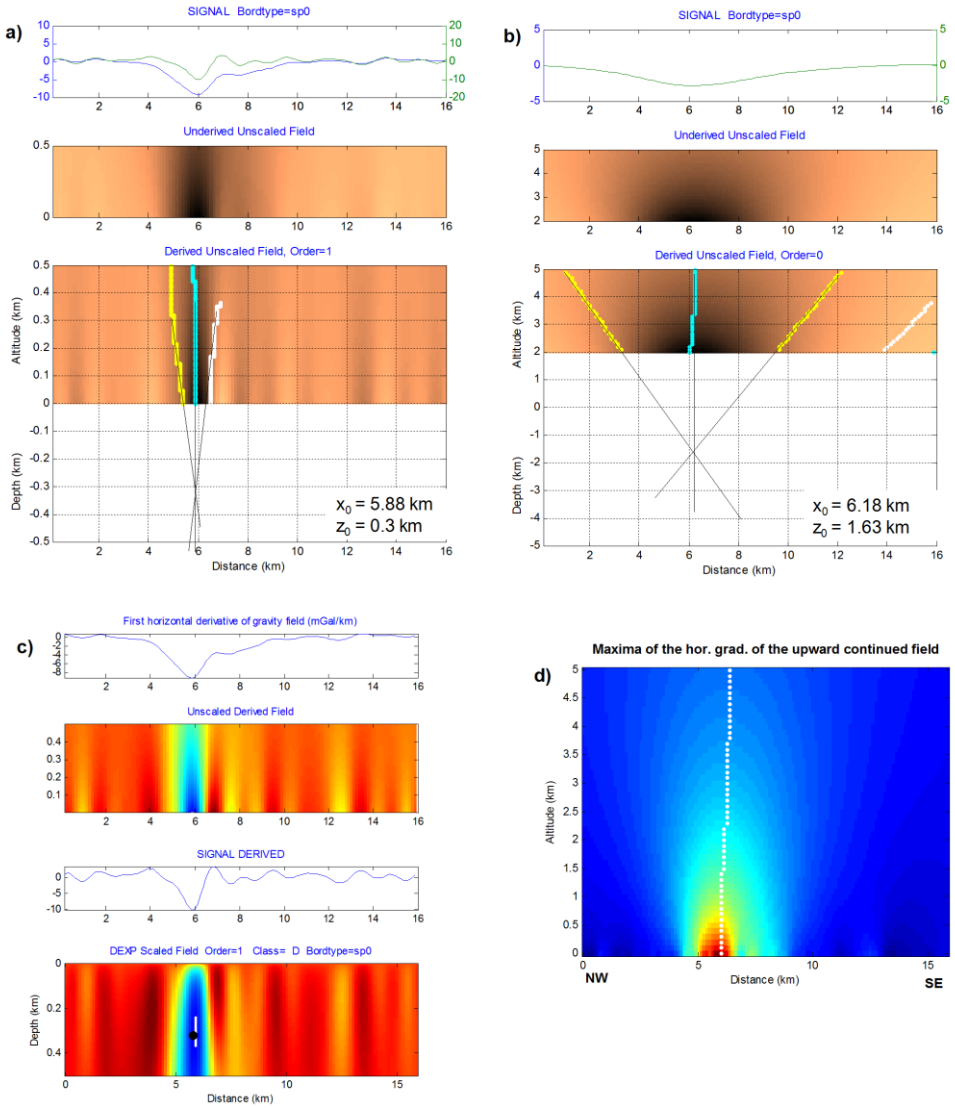

Figure 6.11. *Analysis of the data shown in Fig. 6.10b). a)-b) Results of the Multiridge Geometric method applied to the first order vertical derivative of the gravity field at low altitudes and to the gravity field at high altitudes to obtain estimates of the position of the upper and lower part of the contact and of its dip. c) DEXP analysis yielding information about the source structural index N. d) Plot of maxima of the horizontal gradient of the upward continued field showing that the faults is slightly dipping towards SE.*

Finally, the McGrath analysis confirmed that the fault is dipping toward SE (Fig. 6.11d).

For the 2D data inversion we used a data spacing of 125 m and discretized the source volume by 128 x 60 cubic cells, with 125 m sides. A positivity constraint was set for the inversions. The reconstructions obtained by resorting to the information derived from the data analysis of Fig. 6.11 as inversion constraints are shown in Fig. 12. The solution obtained by using only the structural index N_{MAG} = 0.1 as depth-weighting function is characterized by a density maximum located at about 250 m depth (Fig. 6.12a), which is close to the depth-to-the-top resulting by *Multiridge Geometric Method* (300 m), but the reconstruction does not image the shape of the dipping contact. The inclusion of constraints about the depth-to-the-top (250 m) and dip of the structure (80°) as inferred by the *Multiridge Geometric Method* (Fig. 6.11a-b), and about the horizontal position of the of the fault (x_0=5875 m) as shown by the horizontal gradient (Fig. 6.10c) lead to a solution that images the fault pattern rather well (Fig. 6.12b) and that is characterized by a density distribution in agreement with the geological information and the results of the analysis by Stavrev and Reid (2010).

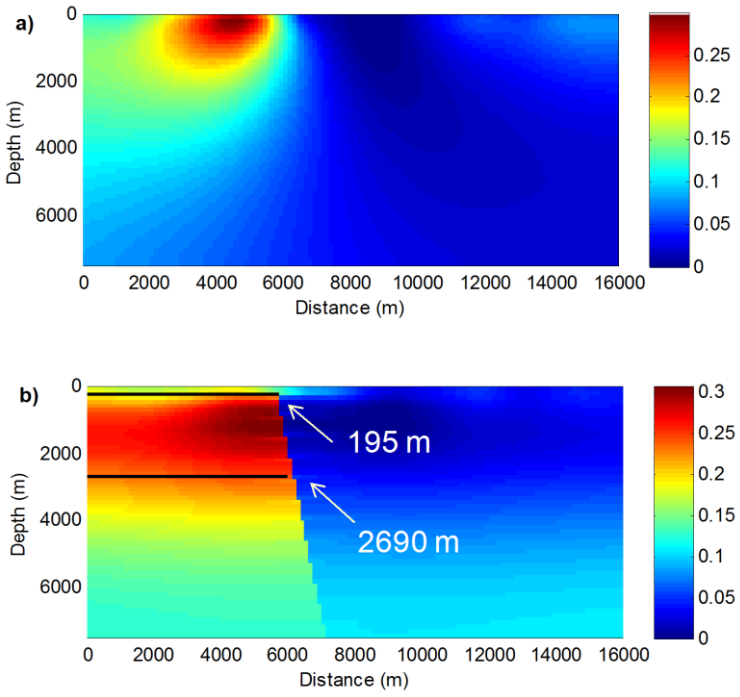

Figure 6.12. *Density models (in g/cm^3) obtained from the inversion of the real gravity data shown in Fig. 6.10b. a) Reconstruction constrained only by a depth-weighting function with □=N=0.1, as suggested by the previous data analysis (see Fig. 6.11). The source top is reconstructed at its correct depth, but the shape of the dipping contact is not well imaged. b) Solution obtained with the additional constraints about the fault depth-to-the-top, horizontal position and dip. The reconstructed density distribution is in agreement with the results of the analysis by Stavrev and Reid (2010); the horizontal black lines in b) represent the estimates of the depths to the fault's top and bottom as found by Stavrev and Reid (2010) .*

CHAPTER VII

Dependency of the solution on the depth weighting function

7.1 Introduction

In the Chapter 6 we studied the dependency of the model obtained by smoothing inversion (Li and Oldenburg 2003 algorithm) on the depth weighting function and we concluded that introducing constraints of different type, (gradients, upper and lower boundary of model parameter values), the influence of the value of exponent β assigned at depth weighting function on the solution is not so strong.

Now we study again the dependency on the depth weighting function of models obtained by the focusing inversion algorithm (Zhdanov, 2002) and data space inversion algorithm (Pilkington, 2009).

7.2 Focusing inversion VS depth weighting

In chapter 3 (paragraph 3.7) we described the focusing inversion algorithm and we said that, similarly to the Li and Oldenburg algorithm, also this algorithm uses a depth weighting function, called *sensitivity* (Zhdanov, 2002) defined as (eq. 3.26):

$$W_z^2 = \sqrt{\sum_i \left(A_{ik}\right)^2} \qquad (7.1)$$

We know (paragraph 3.7.3) that the solution at the first iteration of focusing inversion provides the smoothest solution, that is the same obtained with Li and Oldenburg algorithm (we remember that with focusing inversion all models obtained at the various iterations are solutions to the inverse problem with the same accuracy). Considering the same magnetic synthetic field generated by two

sources, as shown in Chapter 3 (Fig7.1), with the same 3D model discretization. In Fig. 7.2 we compare the solution obtained at the first iteration of focusing inversion (*a*) with the solution obtained using smoothing inversion algorithm (Li and Oldenburg, 2003) (*b*), without imposing any constraints and using for β a value of 3, because this is the correct exponent to use as demonstrated in Chapter.4. Observing the model obtained by focusing inversion, it is evident that the depth to both sources is underestimated, whereas it is correctly estimated by the smoothing inversion algorithm.

In Fig. 7.2c we show the model obtained by using smoothing inversion algorithm, using, this time, β= 2. Comparing the model in (a) and the model in (c) it is evident that they are identical.

This means that the sensitivity weighting function (eq. 7.1) used in focusing inversion is theoretically not suitable for all cases, but corresponds, in the magnetic case, to the depth weighting used by Li and Oldenburg (1996) with β=2. This means, as shown in Chapter 4, that the sensitivity is a correct weight only when the source has a structural index of 2.

Similarly, it is possible to demonstrate that in the gravity case the sensitivity weight (eq.7.1) corresponds to the depth weighting used by Li and Oldenburg (1996) with β=1.

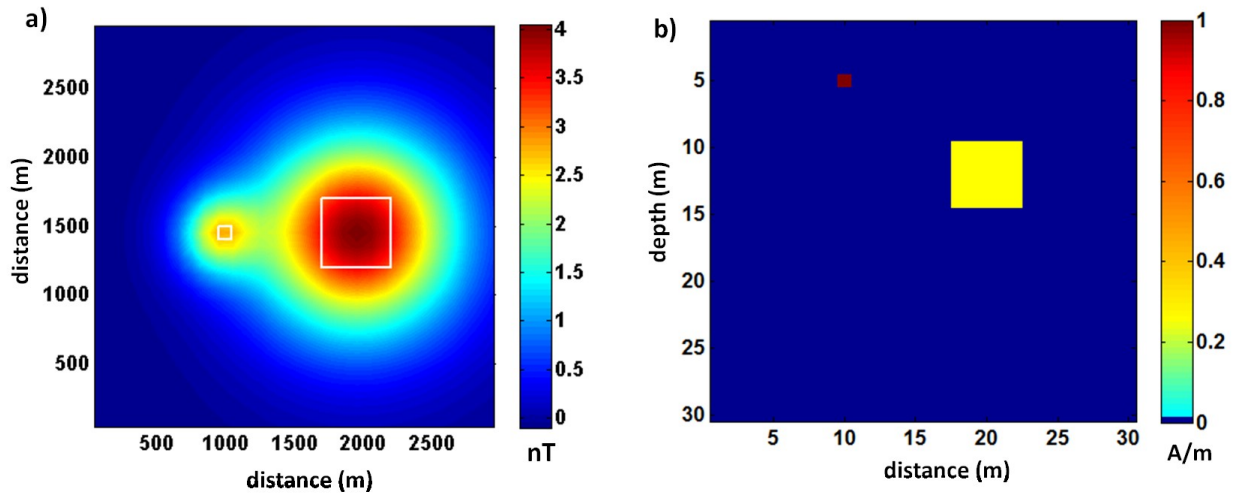

Figure 7.1. *a) Magnetic field of the synthetic model shown in b; b) Cross section at y= 1500 m of the synthetic model: the shallow source is a 100 m^3 block with a 1 A/m magnetization; the deepest source is a cubic prism of 500 m^3 with a 0.25 A/m. magnetization. We assumed a vertical direction for both the inducing field and the magnetization vector.*

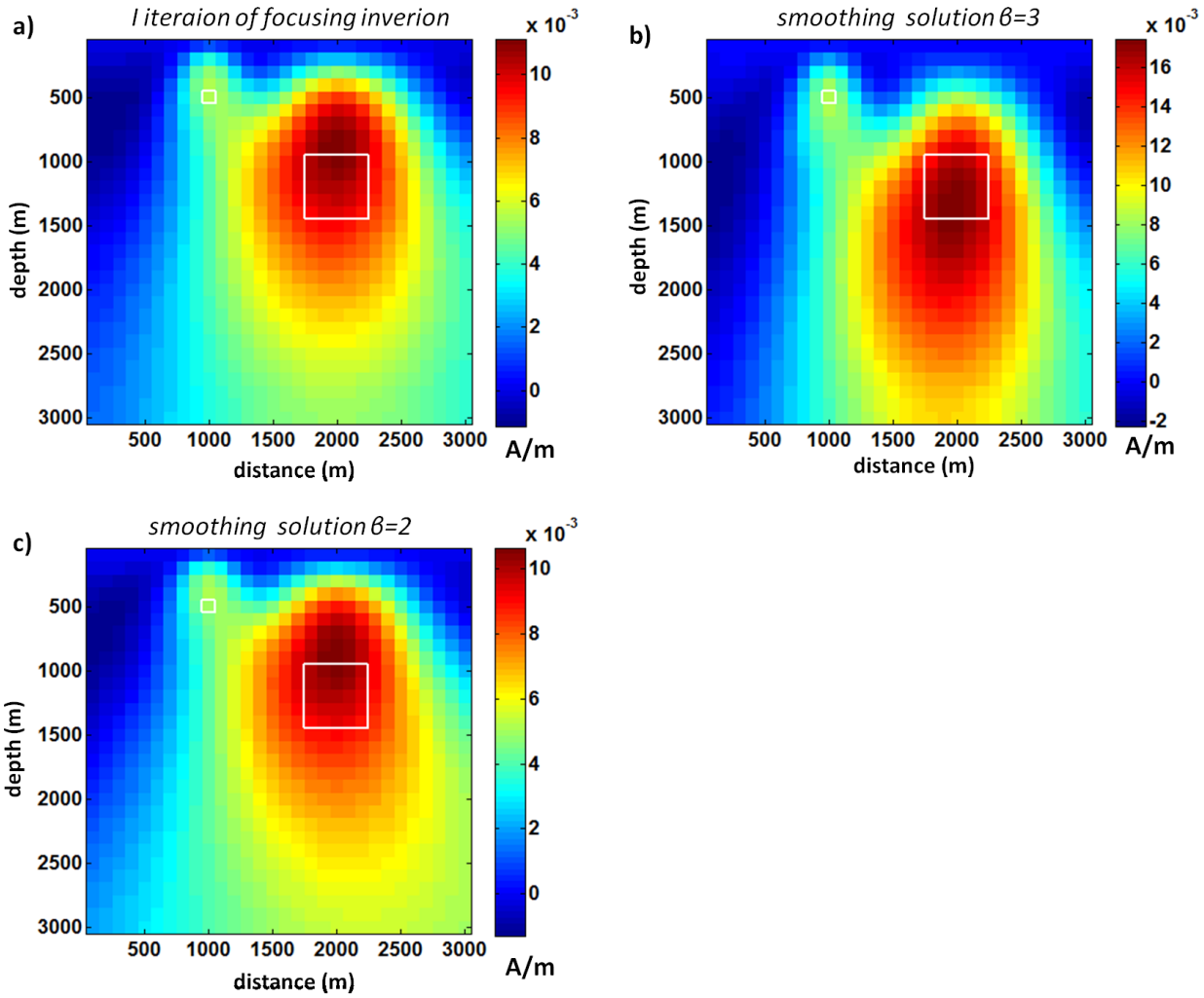

Figure 7.2. *a) solution obtained after the first iteration of focusing inversion algorithm: the depth of both sources is underestimated; b) solution obtained using smoothing inversion algorithm without any constraints with β=3: the depth is correctly estimated; c) solution obtained using smoothing inversion algorithm without any constraints with β=2: the depth to both source is underestimated and the model is identical to that presented in a).*

However, the purpose of a focusing inversion algorithm should not be to provide smoothed solutions, but focused. In Fig. 7.3 we show some models obtained after a

different number of iterations of focusing inversion using boundary values differentiated of 1 A/m and 0.25 A/m (see Section 3.7.3). The compactness increases with the iterations, and because we use the strong constraint of focusing, already at the third iteration the depth is correctly estimated in spite of using a depth weighting not appropriate.

Therefore also for focusing inversion we can conclude that the inversion with constraints is less dependent on the depth weighting function.

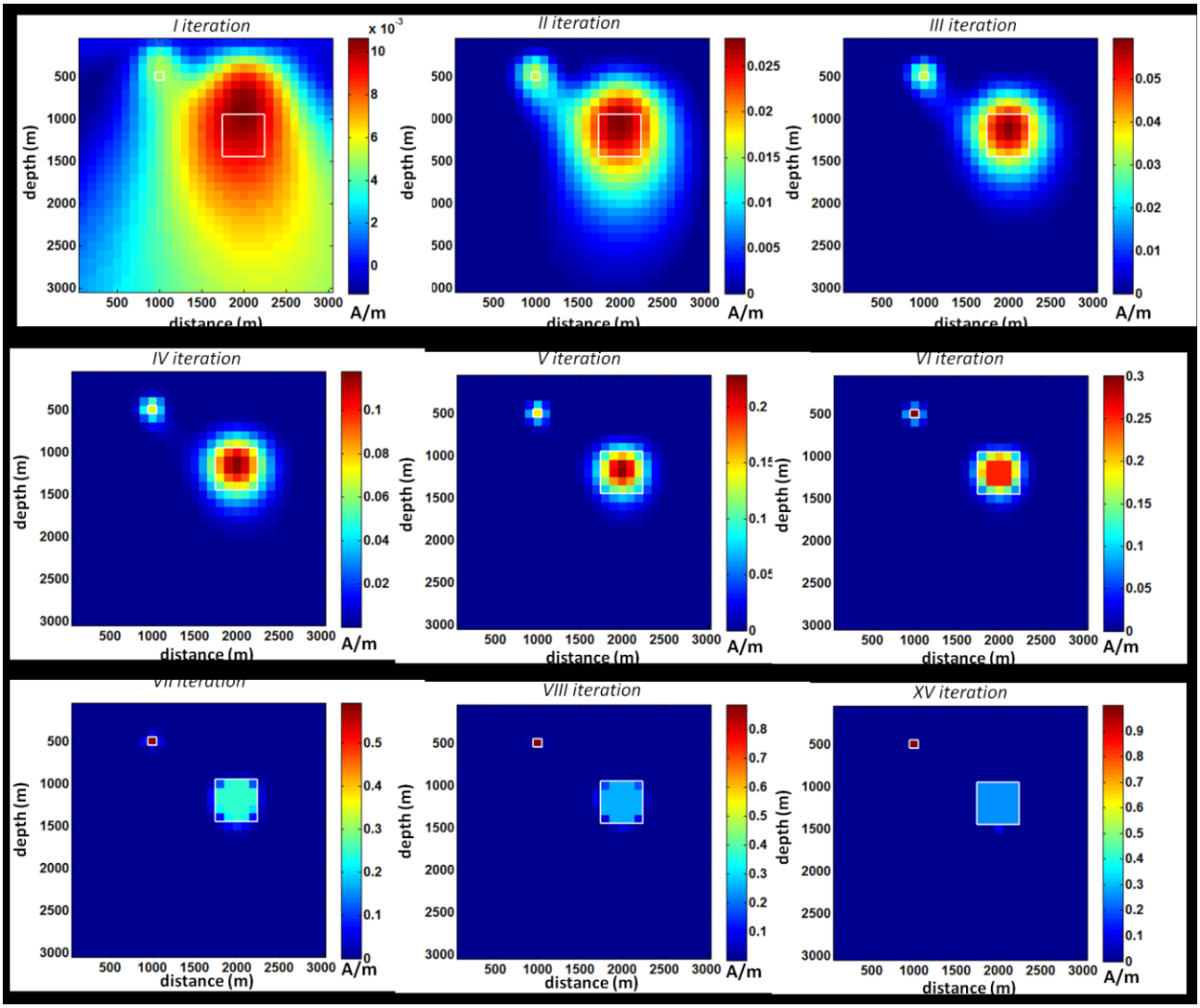

Figure 7.3. *Some models obtained after a different number of iterations by using the focusing algorithm in the magnetic case; focusing increases with the iteration number.*

In Fig. 7.4 we show the focused inversion results for the gravity field generated by the same geometrical model. At the first iteration, the solution is shallower than the first iteration of magnetic case, and just at the sixth iteration the depth is correctly estimated. This happens because, as said above, the sensitivity matrix used as depth weighting correspond, for gravity case, to use the depth weighting function of Li and Oldenburg (eq. 3.1) with β=1, but the correct value according to the invariance rules (chapter 4) is still 3. Once again, similarly to the magnetic case, the use of boundary values for the density guarantees that increasing the iteration number the model is correctly reconstructed.

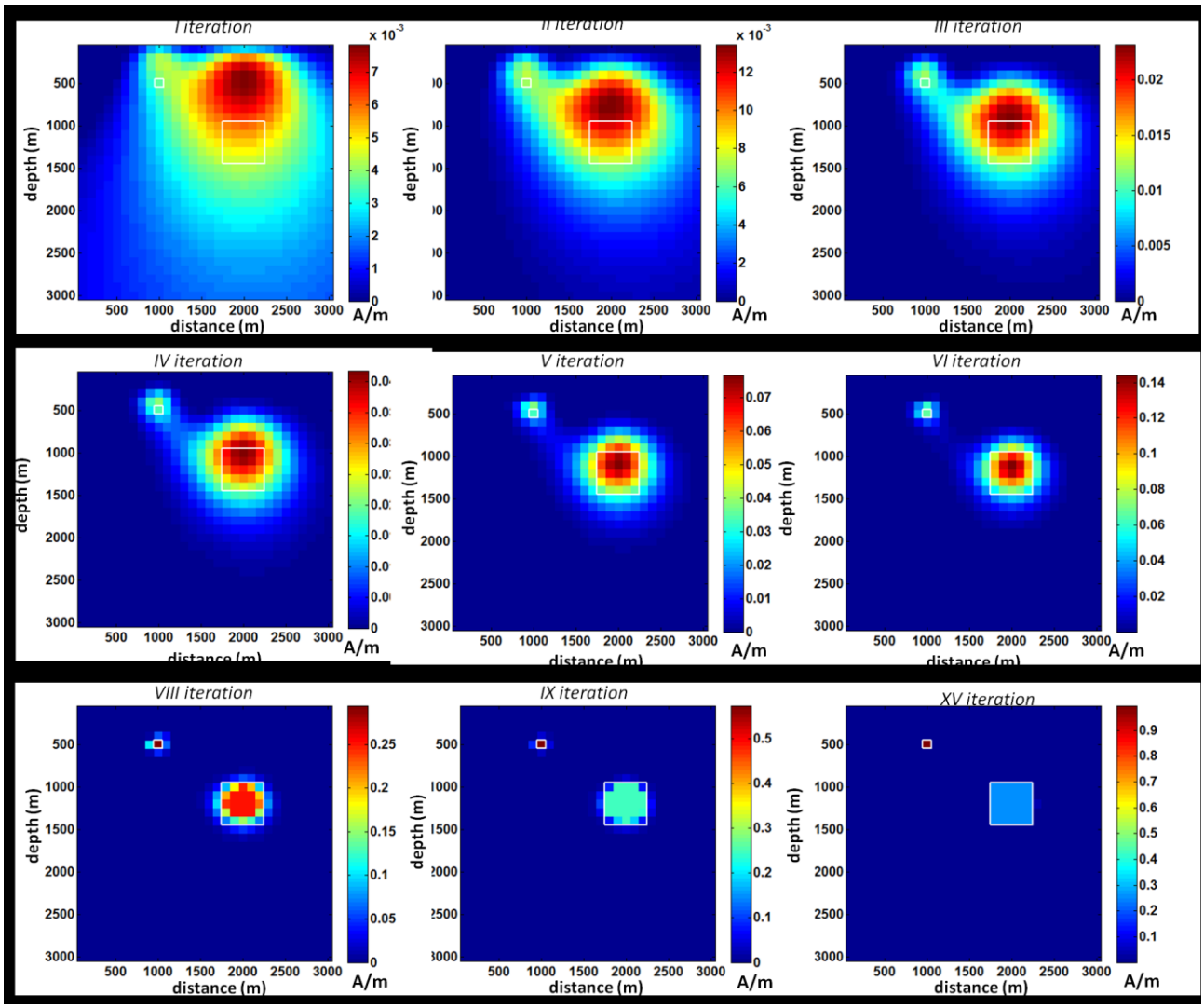

Figure 7.4. *Some models obtained after a different number of iterations by using the focusing algorithm in the gravity case; focusing increases with the iteration number.*

7.3 Data space inversion VS depth weighting

In the Chapter 3 (paragraph 3.8) we described the data space inversion algorithm. The depth weighting used in this algorithm is defined similarly to that introduced by Li and Oldenburg (1996, 1998), eq. 3.44:

$$Z = \frac{1}{(z)^{\beta}}$$

Pilkington (2009), uses β=3 for magnetic case independently on source type. We know from the invariance rules (Chapter 4) that the value of β does not change with the order of derivation of field (e.g, gravity, magnetic or other order derivatives), but changes according to structural index of the source (Cella and Fedi, 2012). Then, also in this case, like Li and Oldenburg algorithm, we need to estimate the structural index value to obtain a correct estimate of source depth. In this section we will illustrate how the solution changes if we estimate erroneously the structural index of the source.

To do this we consider once again the synthetic case with two sources at different depth (Fig 7.1). In Chapter 4 we have estimated the structural index for these two sources obtaining a value of 3 for both sources.

In Chapter 3, paragraph 3.8, Fig. 3.7 we have already seen that in the magnetic case using β=3 it is possible to correctly estimate the depth to the center of these sources for any value of σ parameter.

In Fig. 7.5 we show the solutions obtained using β=2 and σ=1 (a), σ=0.12 (b), σ=0.1 (c), σ=0.001 (d). The depth to center in maximum smoothing solution (σ=1) is slightly underestimated, this error decreases increasing the level of sparseness and for σ very low (eg. 0.001) a compact solution with unrealistic susceptibility value is produced. The sources' center is correctly estimated similarly to focusing inversion at large number of iterations without upper bound on density (Fig. 3.6).

Finally, in Fig. 7.6 we show the solutions obtained using β=1 and σ=1 (a), σ=0.05 (b), σ=0.02 (c), σ=0.0001 (d). The depth is underestimated in all cases, and neither the maximum compact solution provides the perfect depth to center of deepest source. Thus, also in the case of data space inversion, imposing constraints (i.e. sparseness constrains) tends to decrease the importance of the depth weighting function. However, if the value of β is too different from the correct one, the depth weighting function can still evidently influence the depth to the source distribution.

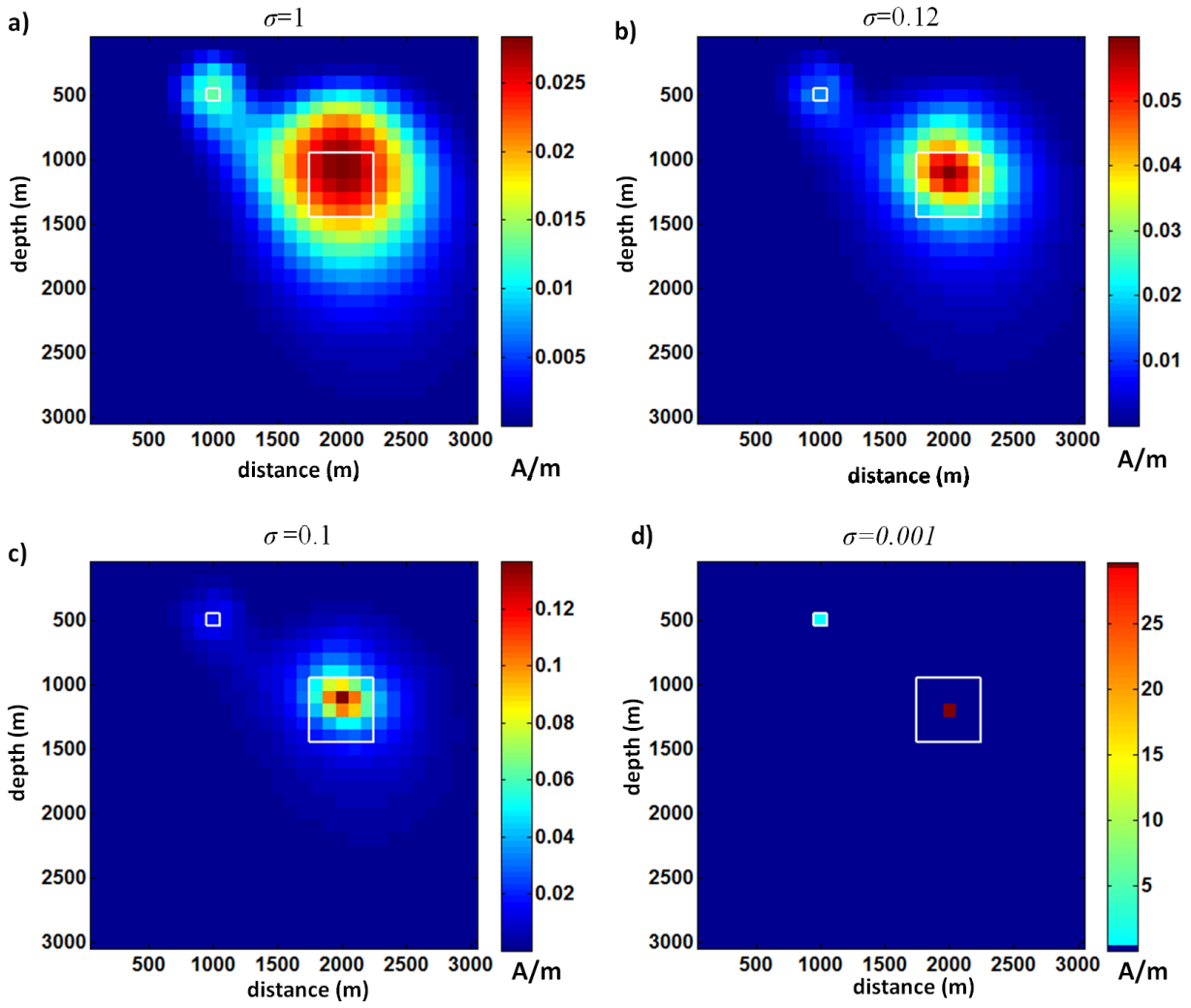

Figure 7.5. *Data space inversion solutions with sparseness constraints using: a) σ=1, b) σ=0.12, d) σ=0.1, d) σ=0.001 and using for β = 2.*

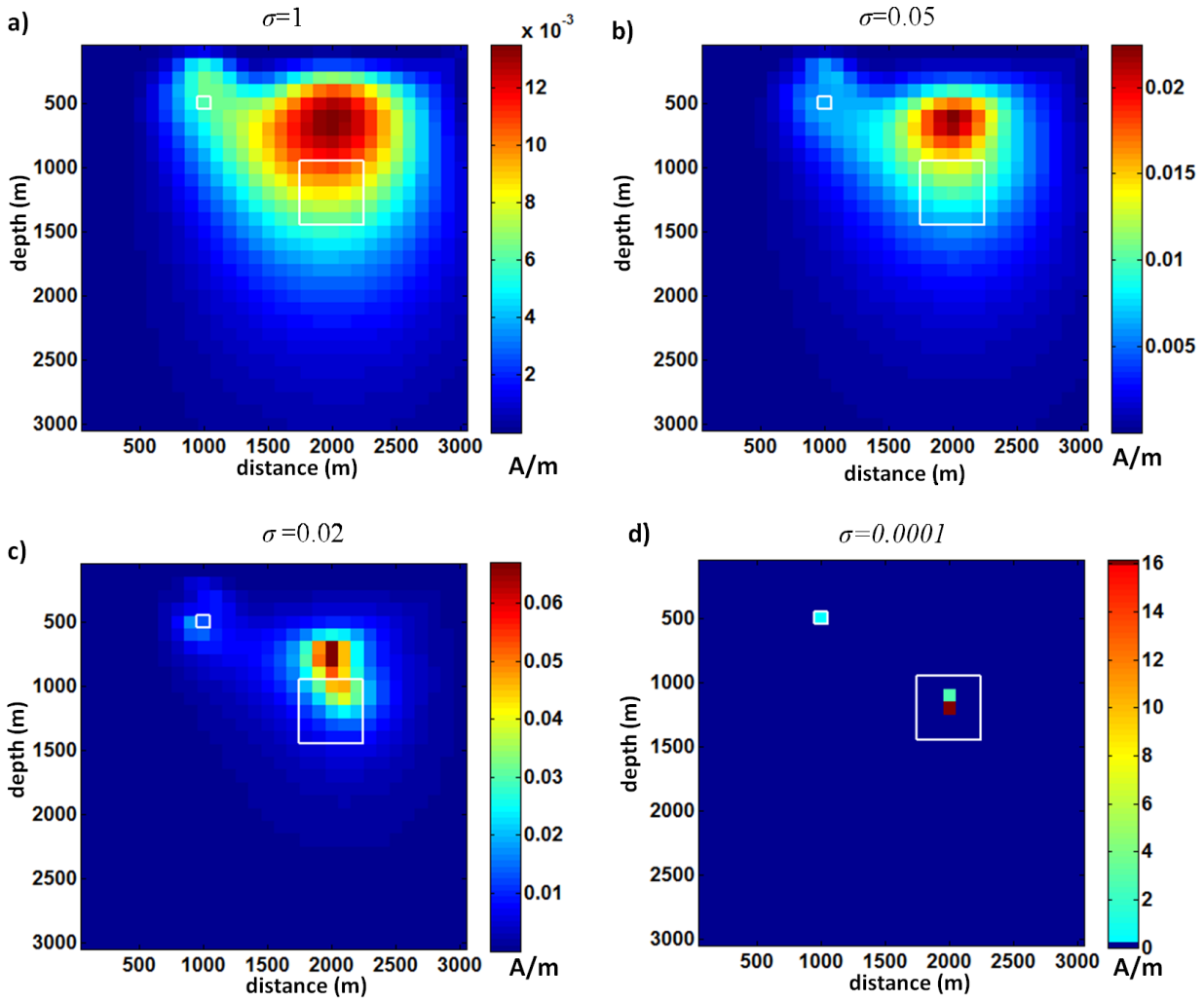

Figure 7.6. *Data space inversion solutions with sparseness constraints using: a) σ=1, b) σ=0.12, d) σ=0.1, d) σ=0.001 and using for β a value of 1.*

CHAPTER VIII

The problem of zero level

In Section 1.2 we have seen that the observed gravity is the sum of the following components (Blakely, 1996):

-attraction of the reference ellipsoid (theoretical gravity)
-effect of elevation above sea level (free air effect)
-effect of “normal” mass above sea level (Bouguer slab and terrain effects)
-time-dependent variations (tidal and instrumental drift effects)
-effect of moving platform (Eötvös effect)
-effect of masses that support topographic loads (isostatic effects)
-effect of crust and upper mantle density variations ("geology").

Our goal is to isolate the last quantity, the effect of crustal and upper mantle density variations, from all other terms. This process is referred to as gravity reduction.
After the gravity reduction, the anomaly may have an arbitrary zero level that can be positive or negative. This constant effect must be removed prior to perform the inversion, because the model is finite and cannot generate the constant field necessary to fit the anomaly.
We can remove this constant level manually, arbitrarily scaling the field, but it is very hard to choose the correct zero level of an anomaly. Alternatively, we propose an automatic procedure to calculate this constant, that allow to fit the data.

The idea is to introduce a new unknown in the system able to generate a constant field. This is obtained by including another cell with a thickness equal to that of model extending to infinity in *x* and *y* direction. To calculate this effect we use the classic equation of Bouguer slab with unit density:

s=0.0418*Z (8.1)

where Z is the thickness of slab.

Therefore we add this new unknown m_s to the system **d=Am** :

$$\begin{pmatrix} d_1 \\ \vdots \\ d_i \\ \vdots \\ d_n \end{pmatrix} = \begin{pmatrix} a_{1,1} & \cdots & a_{1,m} & s \\ \vdots & a_{ij} & \vdots & \vdots \\ a_{n,1} & & a_{n,m} & s \end{pmatrix} \begin{pmatrix} m_1 \\ \vdots \\ m_j \\ \vdots \\ m_m \\ m_s \end{pmatrix} \qquad (8.2)$$

where *s* is given by eq. 8.1 and m_s represent the density of the slab generating the constant field necessary to correctly fit the data.

In Fig. 8.1a we show the gravity anomaly generated by the two sources at different depths already studied in previous Sections (Fig 8.1b).). The shallow source is sized 100 x 100 x 100 m^3 and depth to center z=450 m, with a 100 m^3 volume and 1 g/cm^3 density; the deepest source is sized 500 x 500 x 500 m^3 and extend from z=900 m to z= 1400 m with a 0.25 A/m density. The 3D source domain was discredited as 30x30x30 cubic cells, each sized 100x100x100 m^3. Furthermore we added a constant

effect generated by a background density of 0.8 g/cm^3. As said before, this anomaly cannot be inverted with the usual approach; therefore we adopt our strategy and invert the system in 8.2, using the new unknown (slab) and a reference model m_0 = 0.

The model obtained is showed in Fig. 8.1c. This model is characterized by a zero background density and the recovered value for m_s is 0.7999 g/cm^3, very close to the density that we used to generate the field in Fig. 8.1a

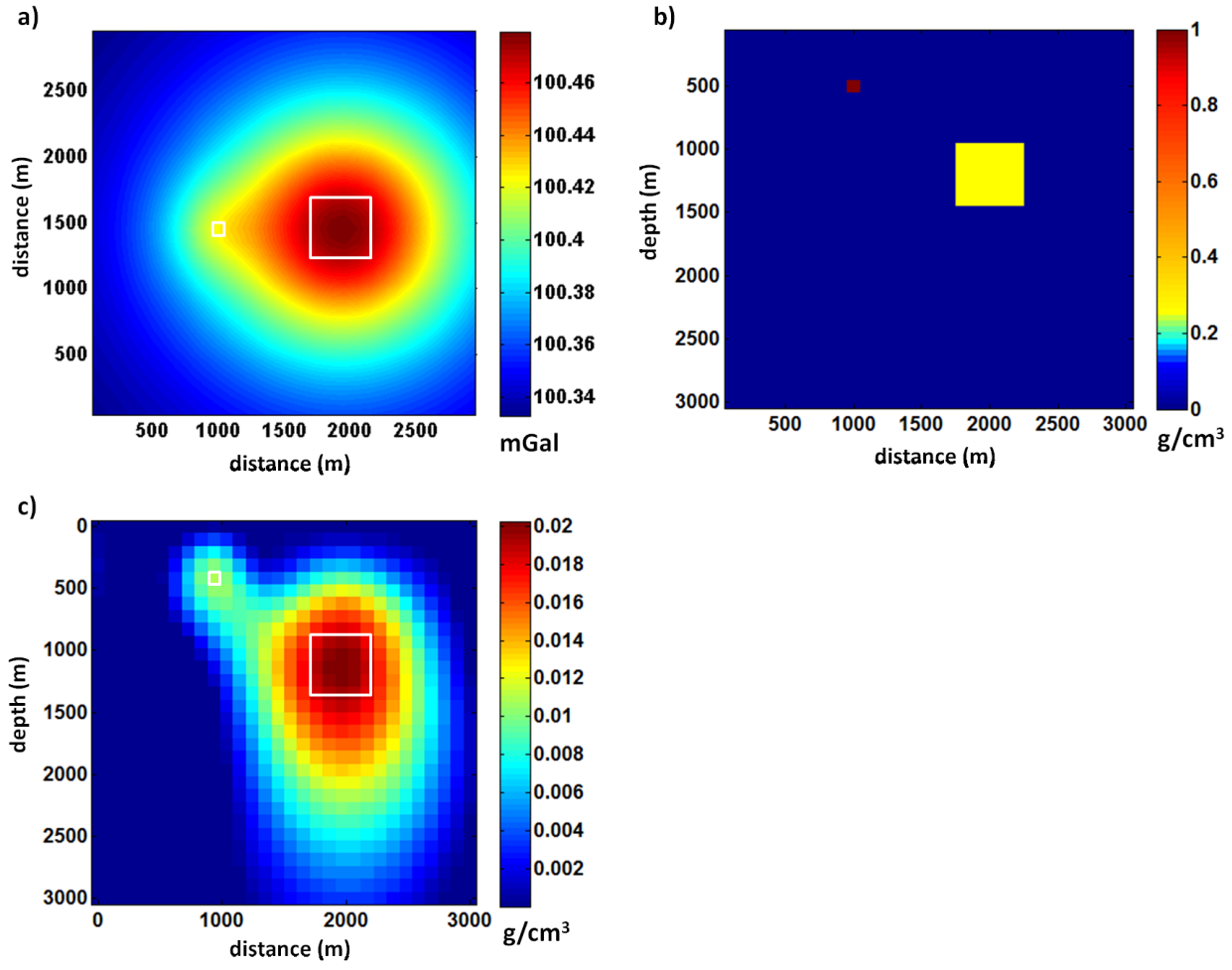

Figure 8.1. *a) gravity field of the synthetic model shown in b), plus a constant given by a background of 0.8 g/cm^3; b) Cross section at y= 1500 m of the synthetic model with 2 sources: the shallow source is a 100 m^3 block with density of 1 g/cm^3; the deepest source is a cubic prism of 500 m^3 with density of 0.25 g/cm^3;*

c) Cross section at y=1500m of density model obtained inverting the anomaly in a) using the new unknown (slab).

In Fig. 8.2a we show the case in which the base level is negative. This case is even more difficult to solve than the previous one, because now we cannot use the positivity constraint (a solution without negative value cannot fit the negative value of the field). However, using the slab makes it possible to use this constraint, because the slab density will assume negative values. In Fig. 8.2b the solution obtained without positivity constraint is shown. The model includes cells with negative densities. In Fig. 8.3c the solution without positivity constraint, but using the slab is shown. The model obtained is very similar to the one that would be computed starting from a field without constant levels and without using the positivity constraint (Fig. 3.4). Finally, in Fig. 8.3d, we show the solution obtained using positivity constraint and using the slab. The result is very similar to that recovered when the constant level was positive (Fig. 8.1c), but this time the slab assume a negative value (-6.6e-004 g/cm^3).

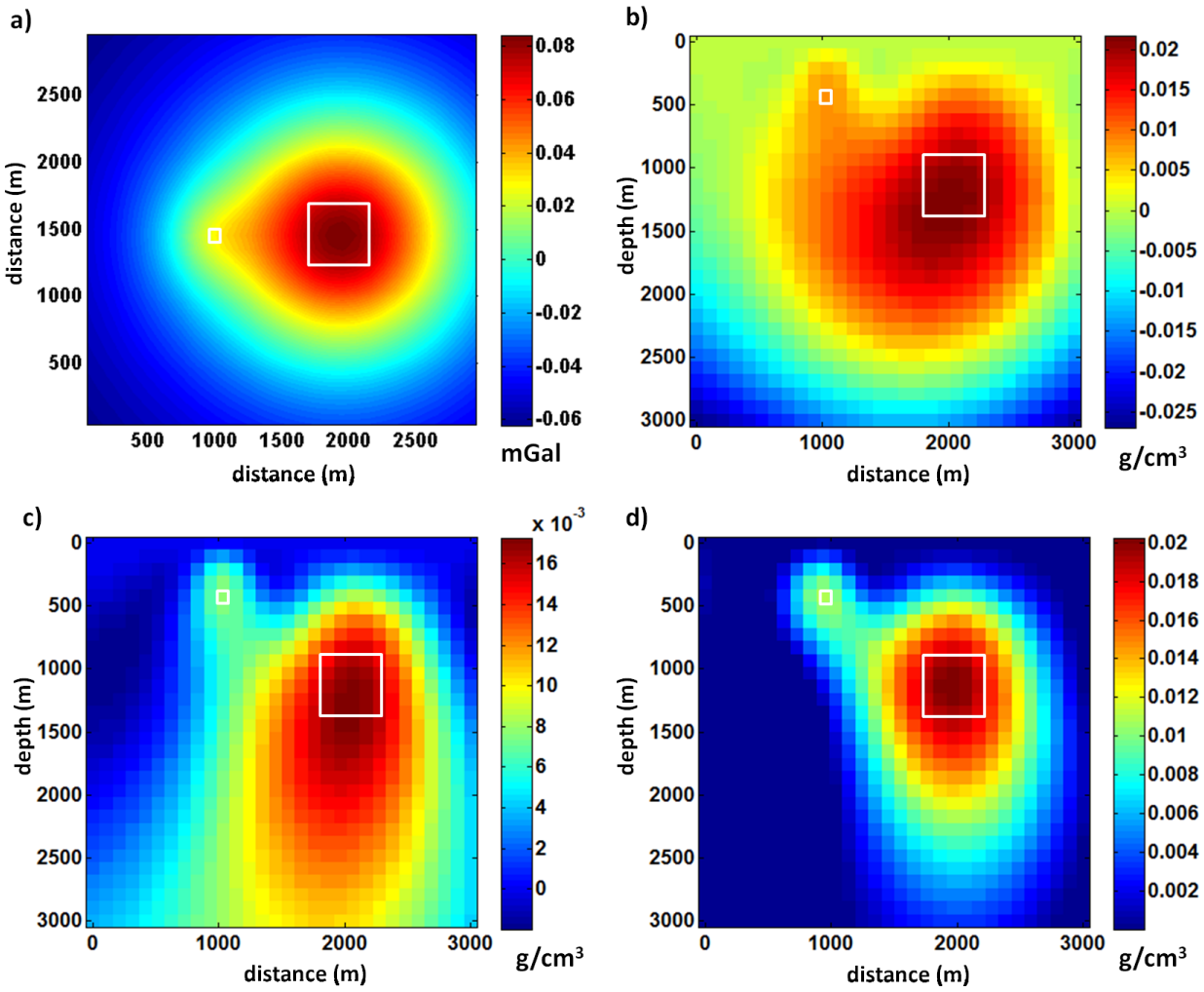

Figure 8.2. *a) gravity field of the synthetic model shown in 8.1b, scaled to have some negative values; b) Cross section of the density model (at y=1500m) obtained inverting the anomaly in a) without slab and without positivity constraint; c) Cross section of the density model (at y=1500m) obtained inverting the anomaly in a) using slab and without positivity constraint; d) Cross section of the density model (at y=1500m) obtained inverting the anomaly in a) using slab and positivity constraint.*

The slab is useful also in the case when we use a reference model m_0 different by zero to invert data with arbitrary zero level. In fact, if we know, by a priori information, the background density, we can introduce this information in the inversion algorithm as a constant reference model. In this case it is crucial use the slab, because the rock density distribution included in the reference model will not fit the data.

We consider the same anomaly in Fig. 8.1a and perform three different inversions using three different values for the reference model (m_0 = 0.8 g/cm^3, 0.4 g/cm^3 and 1.2 g/cm^3) and using the slab. Furthermore, it is important to say that for this inversion with $m_0 \neq 0$ it is necessary to add an external padding extending outside the area covered by data to assure the generation of a constant field value. To this aim, we add one cell of 50000 m, for each of the four sides of the model.

The results are shown in Fig. 8.3 a,b,c in the cases when m_0 = 0.8 g/cm^3, 0.4 g/cm^3 and 1.2 g/cm^3 respectively. It is possible to note the background density is equal to m_0 in all cases. The slab assumes the values of 0.0189 g/cm^3, 0.4094g/cm^3 and -0.3716g/cm^3 respectively for the three cases and these values approximately correspond to the difference between the density producing the constant level in data (0.8 g/cm^3) and the density of m_0. Thus the role of the inclusion of the slab, in these cases is to guarantee the data fitting, difficult to obtain if the reference model does not have the correct density value.

If a not constant reference model is used, the inclusion of the slab is fundamental to fit the data.

A similar strategy could be devised to handle the magnetic case.

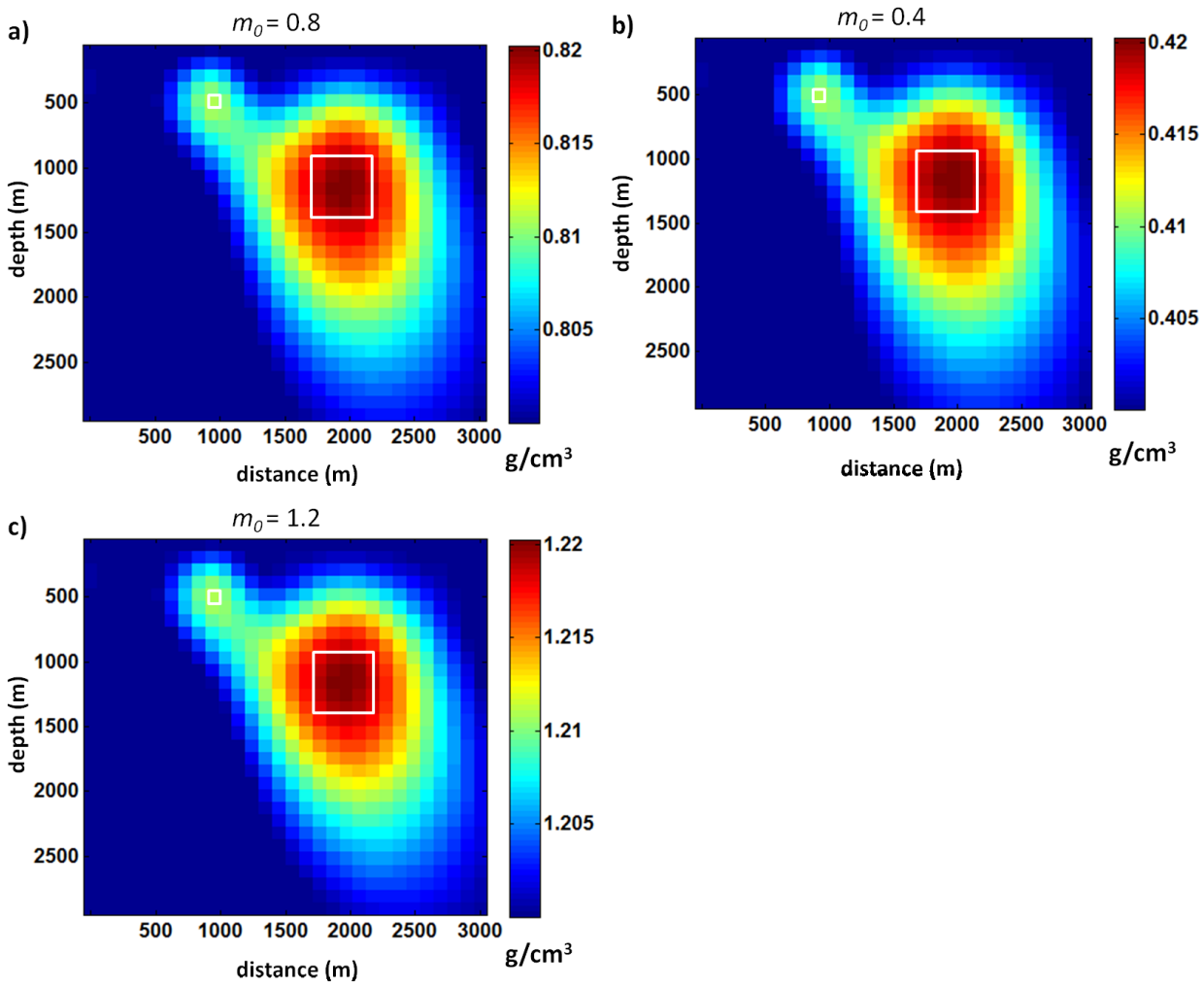

Figure 8.3. *Cross section at y=1500m of density model obtained inverting the anomaly in 8.1a using slab and a) m_0= 0.8 g/cm^3, b) m_0=0.4 g/cm^3, c) m_0= 1.2 g/cm^3.*

Conclusions

In this thesis we have implemented and studied on detail three different potential field inversion algorithms proposed by Li and Oldenburg (2003), Portniaguine and Zhdanov (2002) and Pilkington (2009). We focused our attention on the dependency of the solution with respect to external constraints and particularly with respect to the depth weighting function. This function is necessary to counteract the natural decay of the data kernels with depth, so providing depth resolution to the inverse solution.

We derived invariance rules for either the minimum-length solution and for the regularized inversion with depth weighting and positivity constraints. For a given source class, the invariance rule assures that the same solution is obtained inverting the magnetic (or gravity) field or any of its k^{th} order vertical derivatives. We demonstrate mathematically this invariance rule for the minimum-length solution both in frequency and in space domain and in space domain for the regularized inversion with depth weighting function. A further invariance rule regards the inversion of homogeneous fields: the homogeneity degree of the magnetization distribution obtained inverting any of the *k*-order vertical derivatives of the magnetic field is the same as that of the magnetic field, and does not depend on *k*. Similarly, the homogeneity degree of the density distribution obtained inverting any of the *k*-order vertical derivatives of the gravity field is the same as that of the 1^{st} order vertical derivative of the gravity field, and does not depend on *k*. This last invariance rule allowed us using the exponent β of the depth weighting function corresponding to the structural index of the magnetic case, no matter the order of differentiation of the magnetic field. This important rule was tested on real gravity data from Noranda (Quebec) and as expected the solution is invariant with respect

to the differentiation order. We also illustrated how the combined effect of regularization and depth weighting could influence the estimated source model depth, in the regularized inversion with depth weighting and positivity constraints. We found that too high regularization parameter will deepen the inverted source-density distribution, so that a lower value for the exponent of the depth weighting function should be used, with respect to the structural index *N* of the magnetic field (or of the 1st vertical derivative of the gravity field). In the attempt to keep the regularization parameter as low as possible, the GCV method yielded better results than the χ^2 criterion.

Furthermore we introduced a new approach to improve the resolution of the model, based on inversion of data with a differentiation order greater than that of the kernel. We are just at the beginning of the study of these type of inversion and what is presented here is only the basis for further study.

We analyzed also the case of a field generated by sources with different structural indices. This is a very important case, because it is the most common situation in real data. In this case, there isn't a unique value for β allowing to obtain accurate estimations of depth to all the sources. Thus the depth weighting exponent β must be varied according to the structural index estimated for each source and according to the invariance rules. Following instead the Li and Oldenburg approach (1998) just one value for the depth weighting should be adopted (β=2 for gravity). But we show that this choice may produce under- or overestimated depths. We test this approach in the inversion of the gravity anomaly of Vredefort Dome impact structure. With our approach, the depth to the structures in Vredefort Dome area are consistent with the available geological information: for the flank of the fold structures of the outer collar we obtained a depth of about 1000 m and a depth of about 6000 m is found for the center of the crustal uplift structure related to the gravity anomaly high.

Furthermore we studied the dependency of the model obtained by inversion on the depth weighting function when a priori information is included in the inversion. We distinguished between external (wells, geological/geophysical information) and field-based constraints, such as the depth to the top, structural index, horizontal position and dip of the source. We presented a self-constrained inversion procedure based only on the constraints retrieved by previous potential field anomaly interpretation steps. We showed that adding, as inversion constraints, information retrieved by a previous analysis of the data has a great potential to lead to well-constrained solutions with respect to the source depth and to the horizontal variations of the source-density distribution. The used constraints can be successfully retrieved by the many methods available in the toolbox of the potential field interpreter. We concentrated our research on the use of multiscale methods that are particularly suitable for a detailed analysis of potential fields. Our analysis on both synthetic and real data demonstrated that the more self-constraints are included in the inversion, the less important is the role of the tuning of the depth-weighting function through the actual value of the source structural index.

Another type of a priori information regards the compactness of solution. This constraint can be imposed using the focusing inversion algorithm (Portniaguine and Zhadanov, 2002) or using sparseness constraints (Pilkington, 2009). In this case, imposing this type of constraint tends to decrease the importance of the depth weighting function.

APPENDIX A

Conjugate gradient

Let's consider the general problem:

d=Am,

where **d** is the data vector, **A** is the kernel matrix and **m** is the unknown model vector. It is possible to solve this problem by conjugate gradient iterative method.

Given the inputs: kernel matrix **A**, data vector **d**, a starting value **x**, a maximum number of iterations i_{max} and an error tolerance $\varepsilon<1$:

{

$i=0$

$\mathbf{r}=\mathbf{A}^T(\mathbf{d}-\mathbf{A}\mathbf{x})$

$\mathbf{p}=\mathbf{r}$

$\delta_{new}=\mathbf{r}^T\mathbf{r}$

$\delta_0=\delta_{new}$

while$(i<i_{max}\&\delta_{new}>\varepsilon^2\delta_0)$

{

$\mathbf{q}=\mathbf{A}\mathbf{p}$

$\alpha \Leftarrow \frac{\delta_{new}}{\mathbf{q}^T\mathbf{q}}$

$\mathbf{x}=\mathbf{x}+\alpha\mathbf{p}$

$\mathbf{r}=\mathbf{A}^T(\mathbf{d}-\mathbf{A}\mathbf{x})$

$\delta_{old}=\delta_{new}$

$\delta_{new}=\mathbf{r}^T\mathbf{r}$

$\beta \Leftarrow \frac{\delta_{new}}{\delta_{old}}$

$\mathbf{p}=\mathbf{r}+\beta\mathbf{p}$

$i=i+1$

}

}

If **A** is overdetermined ($N>M$) the CG converge to least square solution (eq. 2.4).

If **A** is underdetermined ($N<M$) the CG converge to minimum length solution (eq. 2.6).

APPENDIX B

Algebraic demonstration of invariance rules

In this appendix we demonstrate the invariance rules in space domain using few algebraic steps.

B.1 Minimum length case

Give the problem:

$$\mathbf{Am} = \mathbf{d} \qquad \text{(B.1)}$$

and the *minimum length solution*:

$$\mathbf{m} = \mathbf{A}^{\mathrm{T}}\left[\mathbf{A}\mathbf{A}^{\mathrm{T}}\right]^{-1}\mathbf{d} \qquad \text{(B.2)}$$

The problem in (B.1) can be rewritten in the equivalent form:

$$\mathbf{DAm} = \mathbf{Dd} \qquad \text{(B.3)}$$

where **D** is any invertible linear operator matrix.

Note that the linear operator of directional derivative is invertible in the vectorial quotient space, that is whenever we consider equivalent two functions differing for just a constant level.

The corresponding *minimum length solution* is:

$$\mathbf{m} = \left(\mathbf{DA}\right)^{\mathrm{T}}\left[\left(\mathbf{DA}\right)\left(\mathbf{DA}\right)^{\mathrm{T}}\right]^{-1}\mathbf{Dd} \qquad \text{(B.4)}$$

As:

$$\left(\mathbf{DA}\right)^{\mathbf{T}} = \mathbf{A}^{\mathbf{T}}\mathbf{D}^{\mathbf{T}} \qquad \text{(B.5)}$$

The eq. B.4 becomes:

$$\begin{aligned}&\mathbf{m} = \mathbf{A}^{\mathbf{T}}\mathbf{D}^{\mathbf{T}}\left[\left(\mathbf{DA}\right)\mathbf{A}^{\mathbf{T}}\mathbf{D}^{\mathbf{T}}\right]^{-1}\mathbf{Dd} = \\ &= \mathbf{A}^{\mathbf{T}}\mathbf{D}^{\mathbf{T}}\left[\mathbf{D}\left(\mathbf{AA}^{\mathbf{T}}\right)\mathbf{D}^{\mathbf{T}}\right]^{-1}\mathbf{Dd}\end{aligned} \qquad \text{(B.6)}$$

Considering the matrix property:

$$\left(\mathbf{XY}\right)^{-1} = \mathbf{Y}^{-1}\mathbf{X}^{-1} \qquad \text{(B.7)}$$

where **X** and **Y** are any matrices, the eq. B.6 becomes:

$$\begin{aligned}&\mathbf{m} = \mathbf{A}^{\mathbf{T}}\mathbf{D}^{\mathbf{T}}\left[\left(\mathbf{D}^{T}\right)^{-1}\left(\mathbf{AA}^{\mathbf{T}}\right)^{-1}\mathbf{D}^{-1}\right]\mathbf{Dd} = \\ &= \mathbf{A}^{\mathbf{T}}\left[\mathbf{D}^{\mathbf{T}}\left(\mathbf{D}^{T}\right)^{-1}\right]\left(\mathbf{AA}^{\mathbf{T}}\right)^{-1}\left(\mathbf{D}^{-1}\mathbf{D}\right)\mathbf{d} = \\ &= \mathbf{A}^{\mathbf{T}}\left[\mathbf{AA}^{\mathbf{T}}\right]^{-1}\mathbf{d}\end{aligned} \qquad \text{(B.8)}$$

B.2 Regularized case

Give the problem:

$$\mathbf{Am} = \mathbf{d} \qquad \text{(B.9)}$$

and the *weighted minimum length solution*:

$$\mathbf{m} = \mathbf{W}_{\mathbf{m}}\mathbf{A}^{\mathbf{T}}\left[\mathbf{AW}_{\mathbf{m}}\mathbf{A}^{\mathbf{T}}\right]^{-1}\mathbf{d} \qquad \text{(B.10)}$$

The problem in (B.9) can be rewrite in the equivalent form:

$$\mathbf{DAm} = \mathbf{Dd} \qquad \text{(B.11)}$$

Where **D** is any linear operator matrix like derivative, continuation, etc.

The corresponding *weighted minimum length solution* is:

$$\mathbf{m} = \mathbf{W_m}(\mathbf{DA})^{\mathbf{T}}\left[(\mathbf{DA})\mathbf{W_m}(\mathbf{DA})^{\mathbf{T}}\right]^{-1}\mathbf{Dd} \qquad \text{(B.12)}$$

As:

$$(\mathbf{DA})^{\mathbf{T}} = \mathbf{A}^{\mathbf{T}}\mathbf{D}^{\mathbf{T}} \qquad \text{(B.13)}$$

The eq. B.12 becomes:

$$\begin{aligned}\mathbf{m} &= \mathbf{W_m}\mathbf{A}^{\mathbf{T}}\mathbf{D}^{\mathbf{T}}\left[(\mathbf{DA})\mathbf{W_m}\mathbf{A}^{\mathbf{T}}\mathbf{D}^{\mathbf{T}}\right]^{-1}\mathbf{Dd} = \\ &= \mathbf{W_m}\mathbf{A}^{\mathbf{T}}\mathbf{D}^{\mathbf{T}}\left[\mathbf{D}\left(\mathbf{AW_m}\mathbf{A}^{\mathbf{T}}\right)\mathbf{D}^{\mathbf{T}}\right]^{-1}\mathbf{Dd}\end{aligned} \qquad \text{(B.14)}$$

Considering the matrix property in B.7, the eq. B.14 becomes:

$$\begin{aligned}\mathbf{m} &= \mathbf{W_m}\mathbf{A}^{\mathbf{T}}\mathbf{D}^{\mathbf{T}}\left[\left(\mathbf{D}^{T}\right)^{-1}\left(\mathbf{AW_m}\mathbf{A}^{\mathbf{T}}\right)^{-1}\mathbf{D}^{-1}\right]\mathbf{Dd} = \\ &= \mathbf{W_m}\mathbf{A}^{\mathbf{T}}\left[\mathbf{D}^{\mathbf{T}}\left(\mathbf{D}^{T}\right)^{-1}\right]\left(\mathbf{AW_m}\mathbf{A}^{\mathbf{T}}\right)^{-1}\left[\mathbf{D}^{-1}\mathbf{D}\right]\mathbf{d} = \\ &= \mathbf{W_m}\mathbf{A}^{\mathbf{T}}\left[\mathbf{AW_m}\mathbf{A}^{\mathbf{T}}\right]^{-1}\mathbf{d}\end{aligned} \qquad \text{(B.15)}$$

Acknowledgments

I would like to give my sincere thanks to my supervisor, Prof. Giovanni Florio, who accepted me as PhD student without any hesitation. Thereafter, he offered me so much advice, patiently supervised me, and always guided me in the right direction.
I would like thanks also Prof. Maurizio Fedi, who offered me his time to help me in my work and for his valuable advice and Prof. Laura Bader for useful advice on some mathematical demonstrations. I thanks also my referee Mark Pilkington for the care and precision proved on review of my thesis.
Special thanks are also given to all my friends and colleague: Gabriella, with which I shared my office and that everyday brought jolliness in our room, Davide, Daniela, Luca, Mahmoud, Mauro, Valeria and all other people wherewith I spent this three years.

Thank you to Mark Dransfield and Fugro Airbone Surveys for the Vredefort Dome data and for the permission to publish our interpretative results.

Finally I would like thanks also eni e&p and CINECA for their cooperation in my work.

References

Barbosa, V. C. F., and Silva, J. B. C., 1994, Generalized compact gravity inversion: *Geophysics*, 59, 57-68.

Barbosa V.C.F., Silva J.B.C., and Medeiros W.E., 1999, Stability analysis and improvement of structural index estimation in Euler deconvolution: *Geophysics*, 64, 1, 48–60.

Bhattacharyya, B.K., 1964, Magnetic anomalies due to prism-shaped bodies with arbitrary polarization: *Geophysics* 29, 517-31.

Blakely R.J. and Simpson R.W., 1986, Approximating edges of source bodies from magnetic or gravity anomalies: *Geophysics*, 51, 1494–1498.

Blakely, R. J., 1996, Potential theory in gravity and magnetic applications: Cambridge University Press, Cambridge.

Boon, J. D., and C. C. Albritton, 1937, Meteorite scars in ancient rocks. *Field lab*, 5-53.

Bott, M. H. P., 1967, Solution of the linear inverse problem in magnetic inter-pretation with application to oceanic magnetic anomalies: *Geophys. J. R.Astron. Soc*., 13, 313 – 323.

Boulanger O., and Chouteau M., 2001, Constraints in 3D gravity inversion: *Geophysical Prospecting*, 49, 265–280.

Cella F., Fedi M. and Florio G., 2009, Toward a full multiscale approach to interpret potential fields: *Geophysical Prospecting* 57, 543–557.

Cella, F., and Fedi, M., 2012, Inversion of potential field data using the structural index as weighting function rate decay: *Geophysical Prospecting*, 60, 313–336.

Cerovský I., 1994, Reweighted Focusing Inversion of Potential Field Data, PhD thesis. Comenius University, Bratislava, Slovakia.

Cordell L.E. and Grauch V.J.S., 1985, Mapping basement magnetization zones from aeromagnetic data in the San Juan Basin, New Mexico. In: The utility of regional gravity and magnetic anomaly maps. Edited by W.J. Hinze: *Society of Exploration Geophysicists*, Tulsa, 181–197.

Corner, B., Durrheim, R. J., and Nicolaysen, L. O., 1990, Relationships between the Vredefort structure and the Witwatersrand basin within the tectonic framework of the Kaapvaal craton as interpreted from regional gravity and aeromagnetic data: *Tectonophysics*, v. 171, p. 49–61.

Cribb, J., 1976, Application of the generalized linear inverse to the inversion of static potential data: *Geophysics*, 41, 1365-1369.

Cuma M., Wilson G. A., and Zhdanov M. S., 2012, Large-scale 3D inversion of potential field data: *Geophysical Prospecting*, 60, 1186-1199.

Dietz RS., 1961, Vredefort ring structure: meteorite impact scar? *J. Geol.* 69:499–516

Dransfield, M. H., 2010, Conforming Falcon gravity and the global gravity anomaly. *Geophysical Prospecting*, 58, 469-483.

Dransfield, M. H., and J. B. Lee, 2004, The Falcon airborne gravity gradiometer survey systems. *In* R. Lane, ed., *Airborne Gravity 2004, the ASEG-PESA Airborne gravity workshop, Australia*, Extended Abstracts, 15-19.

Fedi M. and Florio G., 2001, Detection of potential fields source boundaries by enhanced horizontal derivative method: *Geophysical Prospecting*, **49**, 40–58.

Fedi M., Hansen P.C. and Paoletti V., 2005, Tutorial: Analysis of depth resolution in potential-field inversion: *Geophysics,* 70, A1–A11.

Fedi M., and Florio G., 2006, SCALFUN: 3D analysis of potential field scaling function to determine independently or simultaneously Structural Index and depth to source: *76th Annual Meeting, SEG Expanded Abstracts*, 963-967.

Fedi M., 2007, DEXP: A fast method to determine the depth and the structural index of potential fields sources: *Geophysics*, 72, I1–I11.

Fedi M., Florio G. and Quarta T., 2009, Multiridge analysis of potential fields: geometrical method and reduced Euler deconvolution: *Geophysics*, 74, L53–L65.

Fisher, N. J., and Howard, L. E., 1980, Gravity interpretation with the aid of quadratic programming: *Geophysics*, 45, 403-419.

Florio G. and Fedi M., 2006. Euler deconvolution of vertical profiles of potential field data. 76° SEG Annual Meeting, New Orleans, 1-6 october, 2006, pp. 958-962

Florio G., Fedi M. and Rapolla A., 2009, Interpretation of regional aeromagnetic data by the scaling function method: the case of Southern Apennines (Italy): *Geophysical Prospecting*, 57, 4, 479–489.

Gibson, R.L., and Reimold, W.U., 2000, Deeply exhumed impact structures: a case study of the Vredefort Structure, South Africa. In: Gilmour, I., Koeberl, C. (Eds.),

Impacts and the Early Earth, *Lect. Notes Earth Sci.*, vol. 91. Springer-Verlag, Heidelberg, pp. 249–277.

Gibson, R.L., and Reimold, W.U., 2001, The Vredefort impact structure, South Africa (the scientific evidence and a two-day excursion guide), *Counc. Geosci., Pretoria, Mem*, 92 (111 pp.).

Gibson, R.L., Reimold W. U., Ashley A. J., Koeberl C., 2002, Metamorphism on the Moon: A terrestrial analogue in the Vredefort dome, South Africa?: *Geology*, 30, 475-478.

Gill, P. E., Murray, W., Ponceleon, D. B., and Saunders, M., 1991, Solving reduced KKT systems in barriermethods for linear and quadratic programming. Technical Report SOL 91–7, Stanford University.

Golub, G.H., Heath, M. and Wahba, G., 1979, Generalized cross-validation as a method for choosing a good ridge regression parameter: *Technometrics*, 21, 215-223.

Grant F.S., West G.F, 1965, Interpretation theory in applied geophysics: McGraw-Hill, New York.

Grieve, R. A. F., and A. Therriault, 2000, Vredefort, Sudbury, Chicxulub: Three of a kind? *Annual Review of Earth Planetary Science*, 28: 305-338.

Guillen, A., and Menichetti, V., 1984, Gravity and magnetic inversion with minimization of a specific functional: *Geophysics*, 49, 1354-1360.

Green, W. R., 1975, Inversion of gravity profiles by use of a Backus-Gilbert approach: *Geophysics*, 40, 763-772.

Hansen P.C., 1998, Rank-deficient and discrete ill-posed problems: Numerical aspects of linear inversion: *Society of Industrial and Applied Mathematics*, 247 pp. ISBN 0898714036.

Hansen P.C., 2008, Regularization Tools: A Matlab Package for Analysis and Solution of Discrete Ill-Posed Problems. www.netlib.org/numeralgo.

Hargraves RB, 1961, Shatter cones in the rocks of the Vredefort Ring, *Trans. Geol. Soc. S.Afr.* 64:147–54.

Hart, R. J., Andreoli, M. A. G., Tredoux, M., and De Wit, M. J., 1990, Geochemistry across an exposed section of Archaean crust at Vredefort, with implications for mid-crustal discontinuities: *Chemical Geology*, v. 82, p. 21–50.

Hart, R.J., Hargraves, R.B., Andreoli, M.A.G., Tredoux, M., and Doucoure , C.M., 1995. Magnetic anomaly near the center of the Vredefort structure: implications for impact related magnetic signatures: *Geology* 23, 277– 280.

Henkel, H., and Reimold, W.U., 1996, Integrated gravity and magnetic modeling of the Vredefort impact structure—reinterpretation of the Witwatersrand basin as the erosional remnant of an impact basin: *Econ. Geol. Res. Unit Inf. Circ*., vol. 299. University of the Witwatersrand, Johannesburg. 89 pp.

Henkel, H., and Reimold, W.U., 1998, Integrated geophysical modeling of a giant, complex impact structure: anatomy of the Vredefort Structure, South Africa, *Tectonophysics* 287, 1– 20.

Hutchinson, M.F., 1990, A stochastic estimator of the trace of the influence matrix for Laplacian smoothing splines: *Communications in statistics, Simulation and Computation*, 19, 443-450.

Kamo, S.L., Reimold, W.U., Krogh, T.E., and Colliston, W.P., 1996, A 2.023 Ga age for the Vredefort impact event and a first report of shock metamorphosed zircons in pseudotachylitic breccias and granophyre: *Earth and Planetary Science Letters*, v. 144, p. 369–388.

Kearey P., Brooks M. and Hill I., 2002, An Introduction to Geophysical Exploration. Blackwell Publishing, Oxford.

Last, B. J., and Kubik, K., 1983, Compact gravity inversion: *Geophysics* 48, 713-721.

Lelièvre, P. G., and D.W. Oldenburg, 2006, Magnetic forward modeling and inversion for high susceptibility: *Geophysical Journal International*, 166, 76–90.

Li Y., and Oldenburg D., 1996, 3D inversion of magnetic data: *Geophysics*, 61, 394-408.

Li Y., and Oldenburg D., 1998, 3D inversion of gravity data: *Geophysics*, 63, 109–119.

Li Y., and Oldenburg D., 2003, Fast inversion of large-scale magnetic data using wavelet transform and logarithmic barrier method: *Geophysical Journal International*, 152, 251-265.

Martinez C., Li Y., 2011, Inversion of regional gravity gradient data over the Vredefort Impact Structure, South Africa: 81st Annual Meeting, SEG, Expanded Abstract.

McCarthy, T. S., I. G. Stanistreet, and L. J. Robb, 1990, Geological studies related to the origin of the Witwatersrand Basin and its mineralization: an introduction and a strategy for research and exploration: *South African Journal of Geology*, 93, 1-4.

McGrath P.H., 1991, Dip and depth extent of density boundaries using horizontal derivatives of upward-continued gravity data. *Geophysics,* 56, 1533–1542.

Menke, W., 1984, Geophysical data analysis: Discrete inverse theory: Academic Press.

Nabighian M.N. and Hansen R.O., 2001, Unification of Euler and Werner deconvolution in three dimensions via the generalized Hilbert transform: *Geophysics*, 66, 1805-1810.

Naidu, P.S., and Mathew M.P., 1998, Analysis of geophysical potential fields: Elsevier.

Oldenburg, D. W., and Y. Li, 1994, Subspace linear inverse method, *Inverse Problems,* 10, 915 - 935.

Oldenburg, D. W., and Y. Li, 2005, Inversion for applied geophysics: A tutorial, *in* D. K. Butler, ed., Near-surface geophysics: SEG, 89-150.

Pilkington, M., 1997, 3-D magnetic imaging using conjugate gradients: *Geophysics* 62, 1132-1142.

Pilkington M., 2009, 3D magnetic data-space inversion with sparseness constraints: *Geophysics* 74, L7-L15

Plouff, D., 1976, Gravity and magnetic fields of polygonal prisms and application to magnetic terrain corrections: Geophysics 41, 727-41.

Portniaguine, O., and Zhdanov, M. S., 1999, Focusing geophysical inversion images: *Geophysics* 48, 713-721.

Portniaguine, O., and Zhdanov, M. S., 2002, Magnetic inversion and compression: *Geophysics* 67, 1532-1541.

Reid, A. B., J.M.Allsop, H. Granser, A. J. Millett, and I.W. Somerton, 1990, Magnetic interpretation in three dimensions using Euler deconvolution: *Geophysics*, 55, 80–91.

Reimold, W.U., and Gibson, R.L., 1996, Geology and evolution of the Vredefort impact structure, South Africa: *J. S. Afr. Earth Sci*. 23, 152– 162.

Reynolds J. M., 1997, An introduction to applied and environmental geophysics, John Wiley & Sons Ltd, Chichester, West Sussex.

Sacchi, M. D., and T. J. Ulrych, 1995, High-resolution velocity gathers and offset space reconstruction: *Geophysics*, 60, 1169–1177.

Safon, C., Vasseur, G., and Cuer, M., 1977, Some applications of linear programming to the inverse gravity problem: *Geophysics*, 42, 1215-1229.

Silva J.B.C., Medeiros W. and Barbosa V., 2001, Potential-field inversion: Choosing the appropriate technique to solve a geologic problem, *Geophysics*, 66, 511–520.

Silva J.B.C. and Barbosa V.C.F., 2006, Interactive gravity inversion: *Geophysics* 71, J1–J9.

Stavrev P. and Reid A., 2010, Euler deconvolution of gravity anomalies from thick contact/fault structures with extended negative structural index. *Geophysics*, 75, I51–I58.

Tikhonov A. N., and Arsenin V. Y., 1977, Solutions of Ill-Posed Problems, Winston and Sons, Washington, D.C.

Wilson G., Cuma M., Zhdanov M. S., 2011, Massively parallel 3D inversion of gravity and gravity gradiometry data: *Feature Paper.*

Zhdanov, M. S., 2002, Geophysical inverse theory and regularization problems: Elsevier.